SQ-

The Deep Space Network Progress Report 42-48

September and October 1978

(NASA-CR-157647) THE DEEP SPACE NETWORK Progress Report, Sep. - Oct. 1978 (Jet Propulsion Lab.) 141 p HC A07/MF A01 CSCL 22D

N79-16000
THRU
N79-16020
Unclas
G3/12 13581

December 15, 1978

National Aeronautics and Space Administration

Jet Propulsion Laboratory
California Institute of Technology
Pasadena, California

The Deep Space Network Progress Report 42-48

September and October 1978

December 15, 1978

National Aeronautics and
Space Administration

Jet Propulsion Laboratory
California Institute of Technology
Pasadena, California

The research described in this publication was carried out by the Jet Propulsion Laboratory, California Institute of Technology, under NASA Contract No. NAS7-100.

Preface

Beginning with Volume XX, the Deep Space Network Progress Report changed from the Technical Report 32- series to the Progress Report 42- series. The volume number continues the sequence of the preceding issues. Thus, Progress Report 42-20 is the twentieth volume of the Deep Space Network series, and is an uninterrupted follow-on to Technical Report 32-1526, Volume XIX.

This report presents DSN progress in flight project support, tracking and data acquisition (TDA) research and technology, network engineering, hardware and software implementation, and operations. Each issue presents material in some, but not all, of the following categories in the order indicated.

Description of the DSN

Mission Support
- Ongoing Planetary/Interplanetary Flight Projects
- Advanced Flight Projects

Radio Astronomy

Special Projects

Supporting Research and Technology
- Tracking and Ground-Based Navigation
- Communications–Spacecraft/Ground
- Station Control and Operations Technology
- Network Control and Data Processing

Network and Facility Engineering and Implementation
- Network
- Network Operations Control Center
- Ground Communications
- Deep Space Stations
- Quality Assurance

Operations
- Network Operations
- Network Operations Control Center
- Ground Communications
- Deep Space Stations

Program Planning
- TDA Planning

In each issue, the part entitled "Description of the DSN" describes the functions and facilities of the DSN and may report the current configuration of one of the seven DSN systems (Tracking, Telemetry, Command, Monitor & Control, Test & Training, Radio Science, and Very Long Baseline Interferometry).

The work described in this report series is either performed or managed by the Tracking and Data Acquisition organization of JPL for NASA.

Contents

NETWORK AND FACILITY ENGINEERING AND IMPLEMENTATION

Network

Network Operations Control Center

Ground Communications

Deep Space Stations

Network Functions and Facilities

N. A. Renzetti
Office of Tracking and Data Acquisition

The objectives, functions, and organization of the Deep Space Network are summarized; deep space station, ground communication, and network operations control capabilities are described.

The Deep Space Network was established by the National Aeronautics and Space Administration (NASA) Office of Space Tracking and Data Systems and is under the system management and technical direction of the Jet Propulsion Laboratory (JPL). The network is designed for two-way communications with unmanned spacecraft traveling approximately 16,000 km (10,000 miles) from Earth to the farthest planets and to the edge of our solar system. It has provided tracking and data acquisition support for the following NASA deep space exploration projects: Ranger, Surveyor, Mariner Venus 1962, Mariner Mars 1964, Mariner Venus 1967, Mariner Mars 1969, Mariner Mars 1971, and Mariner Venus-Mercury 1973, for which JPL has been responsible for the project management, the development of the spacecraft, and the conduct of mission operations; Lunar Orbiter, for which the Langley Research Center carried out the project management, spacecraft development, and conduct of mission operations; Pioneer, for which Ames Research Center carried out the project management, spacecraft development, and conduct of mission operations; and Apollo, for which the Lyndon B. Johnson Space Center was the project center and the Deep Space Network supplemented the Manned Space Flight Network, which was managed by the Goddard Space Flight Center. The network is currently providing tracking and data acquisition support for Helios, a joint U.S./West German project; Viking, for which Langley Research Center provided the Lander spacecraft and project management until May, 1978, at which time project management and mission operations were transferred to JPL, and for which JPL provided the Orbiter spacecraft; Voyager, for which JPL provides project management, spacecraft development, and is conducting mission operations; and Pioneers, for which the Ames Research Center provides project management, spacecraft development, and conduct of mission operations. The network is adding new capability to meet the requirements of the Galileo mission to Jupiter, for which JPL is providing the Orbiter spacecraft, and the Ames Research Center the probe. In addition, JPL will carry out the project management and the conduct of mission operations.

The Deep Space Network (DSN) is one of two NASA networks. The other, the Spaceflight Tracking and Data Network (STDN), is under the system management and technical direction of the Goddard Space Flight Center (GSFC). Its function is to support manned and unmanned Earth-orbiting satellites. The Deep Space Network supports lunar, planetary, and interplanetary flight projects.

From its inception, NASA has had the objective of conducting scientific investigations throughout the solar system. It was recognized that in order to meet this objective, significant supporting research and advanced technology development must be conducted in order to provide deep space telecommunications for science data return in a cost effective

manner. Therefore, the Network is continually evolved to keep pace with the state of the art of telecommunications and data handling. It was also recognized early that close coordination would be needed between the requirements of the flight projects for data return and the capabilities needed in the Network. This close collaboration was effected by the appointment of a Tracking and Data Systems Manager as part of the flight project team from the initiation of the project to the end of the mission. By this process, requirements were identified early enough to provide funding and implementation in time for use by the flight project in its flight phase.

As of July 1972, NASA undertook a change in the interface between the Network and the flight projects. Prior to that time, since 1 January 1964, in addition to consisting of the Deep Space Stations and the Ground Communications Facility, the Network had also included the mission control and computing facilities and provided the equipment in the mission support areas for the conduct of mission operations. The latter facilities were housed in a building at JPL known as the Space Flight Operations Facility (SFOF). The interface change was to accommodate a hardware interface between the support of the network operations control functions and those of the mission control and computing functions. This resulted in the flight projects assuming the cognizance of the large general-purpose digital computers which were used for both network processing and mission data processing. They also assumed cognizance of all of the equipment in the flight operations facility for display and communications necessary for the conduct of mission operations. The Network then undertook the development of hardware and computer software necessary to do its network operations control and monitor functions in separate computers. A characteristic of the new interface is that the Network provides direct data flow to and from the stations; namely, metric data, science and engineering telemetry, and such network monitor data as are useful to the flight project. This is done via appropriate ground communication equipment to mission operations centers, wherever they may be.

The principal deliverables to the users of the Network are carried out by data system configurations as follows:

(1) The DSN Tracking System generates radio metric data, i.e., angles, one- and two-way doppler and range, and transmits raw data to Mission Control.

(2) The DSN Telemetry System receives, decodes, records, and retransmits engineering and scientific data generated in the spacecraft to Mission Control.

(3) The DSN Command System accepts spacecraft commands from Mission Control and transmits the commands via the Ground Communication Facility to a Deep Space Station. The commands are then radiated to the spacecraft in order to initiate spacecraft functions in flight.

(4) The DSN Radio Science System generates radio science data, i.e., the frequency and amplitude of spacecraft transmitted signals affected by passage through media such as the solar corona, planetary atmospheres, and plantetary rings, and transmits this data to Mission Control.

(5) The DSN Very Long Baseline Interferometry System generates time and frequency data to synchronize the clocks among the three Deep Space Communications complexes. It will generate universal time and polar motion and relative Deep Space Station locations as by-products of the primary data delivery function.

The data system configurations supporting testing, training, and network operations control functions are as follows:

(1) The DSN Monitor and Control System instruments, transmits, records, and displays those parameters of the DSN necessary to verify configuration and validate the Network. It provides the tools necessary for Network Operations personnel to control and monitor the Network and interface with flight project mission control personnel.

(2) The DSN Test and Training System generates and controls simulated data to support development, test, training and fault isolation within the DSN. It participates in mission simulation with flight projects.

The capabilities needed to carry out the above functions have evolved in the following technical areas:

(1) The Deep Space Stations, which are distributed around Earth and which, prior to 1964, formed part of the Deep Space Instrumentation Facility. The technology involved in equipping these stations is strongly related to the state of the art of telecommunications and flight-ground design considerations, and is almost completely multimission in character.

(2) The Ground Communications Facility provides the capability required for the transmission, reception, and monitoring of Earth-based, point-to-point communications between the stations and the Network Operations Control Center at JPL, Pasadena, and to the JPL Mission Operations Centers. Four communications disciplines are provided: teletype, voice, high-speed, and wideband. The Ground Communications Facility uses the capabilities provided by common carriers throughout the world, engineered into an integrated system by Goddard Space Flight Center, and controlled from the

communications Center located in the Space Flight Operations Facility (Building 230) at JPL.

The Network Operations Control Center is the functional entity for centralized operational control of the Network and interfaces with the users. It has two separable functional elements; namely, Network Operations Control and Network Data Processing. The functions of the Network Operations Control are:

(1) Control and coordination of Network support to meet commitments to Network users.

(2) Utilization of the Network data processing computing capability to generate all standards and limits required for Network operations.

(3) Utilization of Network data processing computing capability to analyze and validate the performance of all Network systems.

The personnel who carry out the above functions are located in the Space Flight Operations Facility, where mission operations functions are carried out by certain flight projects. Network personnel are directed by an Operations Control Chief. The functions of the Network Data Processing are:

(1) Processing of data used by Network Operations Control for control and analysis of the Network.

(2) Display in the Network Operations Control Area of data processed in the Network Data Processing Area.

(3) Interface with communications circuits for input to and output from the Network Data Processing Area.

(4) Data logging and production of the intermediate data records.

The personnel who carry out these functions are located approximately 200 meters from the Space Flight Operations Facility. The equipment consists of minicomputers for real-time data system monitoring, two XDS Sigma 5s, display, magnetic tape recorders, and appropriate interface equipment with the ground data communications.

D2

N79-16002

DSN Monitor and Control System, Mark III-78

W. G. Stinnett
TDA Engineering

A description of the DSN Monitor and Control System, Mark III-78, is discussed. The major implementation required to evolve from the Mark III-75 to the Mark III-78 configuration is also discussed.

I. Introduction

The DSN Monitor and Control System, as well as the other DSN systems, has undergone a significant evolution from late 1976 through the major portion of 1978. This evolution has resulted in the Mark III-78 configuration. Major implementation occurred in each of the three DSN facilities: Deep Space Stations (DSS), Ground Communications Facility (GCF), and the Network Operations Control Center (NOCC). At the DSS, implementation of new computers for the Telemetry, Command, Tracking, and Radio Science Systems significantly changed the DSN Monitor and Control System. In the GCF, implementation has occurred at the stations and at JPL in the central communications terminal. A major software upgrade occurred within the NOCC due to the changes at the stations and the Ground Communications Facility.

The DSN Monitor and Control System, Mark III-78 configuration is multimission and is utilized by the DSN to support the Pioneer 6-11, Helios 1 and 2, Viking, Voyage , and Pioneer Venus-1978 missions. Figure 1 provides a block diagram of the DSN Monitor and Control System, Mark III-78 configuration.

II. Deep Space Station

As part of the DSN Monitor and Control System, the DSS Monitor and Control Subsystem (DMC) provides two primary functions: (1) the DMC provides the central control and monitor capability for the stations, and (2) the DMC receives control data from and furnishes monitor data to the NOCC for Network Central Control and Monitor purposes.

There are three major assemblies of the DMC that accomplish the above two functions. The three major assemblies are:

(1) An XDS 920 computer.

(2) A station monitor and control console.

(3) A special input-output terminal.

A. XDS 920 Computer

The XDS 920 computer has been a part of the DMC for many years. Its designation is the Digital Instrumentation Subsystem (DIS). It has been utilized as a central collection point for station monitor data and interfacing with the NOCC. For collecting station monitor data, the DIS has interfaces with all of the station subsystems. The station monitor data are accumulated by the DIS and displayed to the station operator located at the station monitor and control console. Additionally, a subset of this station monitor data is sent to the NOCC for Network central monitoring purposes. A significant implementation effort was undertaken for the DIS to convert from the Mark III-75 to the Mark III-78 system.

Major interface changes occurred with the implementation of new computers in the DSS Command, Telemetry, Tracking, and Radio Science Subsystems. The interface with these subsystem computers is via the DSN standard computer-to-computer intercommunication device, a star switch controller. Significant implementation was required for the DIS to operate in this computer network. The new generation computers are approximately 10 times as fast for memory cycle time and are 16-bit word machines versus 24-bit word for the DIS (XDS 920). A special hardware interface device was installed between the DIS and the star switch controller to convert from 24-bit to 16-bit words, and vice versa, and to speed up access time for interfacing with the star switch controller. To accommodate interfaces with the new computers and new protocol and timing requirements with the star switch controllers, significant software changes were required in the DIS. Additionally, the structure of the monitor data parameters was either new or significantly modified from that which previously existed.

Another interface change, from the Mark III-75 to Mark III-78 configuration, was implemented for the DIS. The interface with the GCF high-speed data circuit, for receiving and sending data from and to the NOCC, changed. The DIS to GCF interface for the Mark III-78 system is via the star switch controller. The GCF has implemented a computer, the Communication Monitor Formatter (CMF), at each DSS. The DIS generates high-speed data blocks, consisting of station monitor data, and provides the data to the CMF via the star switch controller. The data are multiplexed with other systems data (e.g., telemetry) onto the high-speed data line for transmission to NOCC. The DIS receives control data from the NOCC via this same interface.

B. Station Monitor and Control Console

The station monitor and control (SMC) console has been provided as part of the Mark III-78 system configuration. The SMC console provides a central control and monitor operator's position for some of the subsystems at the DSS (other subsystems are controlled via another input-output device – see Subsection C, below) The SMC consoles are currently in limited use in the Network; however, work is in process to make them a more useful operational tool. Additional station subsystems are being modified to permit central station control from the SMC consoles.

C. Special Input-Output Terminal

With the implementation of new computers in the Command, Telemetry, Tracking, and Radio Science Subsystems (and the CMF at the DSS), a special terminal was installed as a central DSS input-output device. It consists of four elements. two keyboard-CRTs, a hardcopy printer, and "host" software capability. The keyboard-CRTs and printers interface with the host software (which runs in any of the new computers), and the host software then interfaces with all of the new computers via the star switch controller. In this manner, the new computers can be centrally controlled and monitored.

III. Ground Communications Facility

Significant implementation in the GCF has occurred over the last two years. Concurrent with these changes, the GCF Monitor and Control Subsystem (GMC) has undergone major changes. At JPL in the GCF central communications terminal, the Central Communications Monitor (CCM) computer has been implemented to provide central facility monitor capability. The CCM receives GCF monitor data from two sources: (1) from each Deep Space Station CMF, and (2) from equipment located at the central communication terminal at JPL.

At the DSS, each CMF monitors the status of the GCF equipment and provides periodic status messages, via high-speed data circuit, to the central communications terminal CCM. It should be noted that the control of the CMF is from the central input-output terminal at the DSS (see Subsection II-C, above).

Within the central communications terminal, the CCM monitors the status of the GCF equipment. Major implementation has occurred within the central communications terminal over the past two years. Computers, as part of the GCF high-speed subsystem, have been implemented to allow message switching and error detection-correction. These functions are being accomplished in the high-speed switch (HSW) and the error detection-correction (EDC) assemblies. The new computers interface to the CCM via the standard DSN computer interface – the star switch controller.

IV. Network Operations Control Center

The NOCC Monitor and Control Subsystem (NMC) provides the processing capability for central network monitor and control. Although no major hardware changes have occurred in the NMC, significant software changes were required due to major modifications in the DSS and GCF. The high-speed data messages received from the DSS underwent significant modification due to the implementation that occurred there. Still to be implemented in the NMC is the ability to process GCF monitor data from the CCM. When this has been accomplished, the DSN Monitor and Control System, Mark III-78 configuration will be complete.

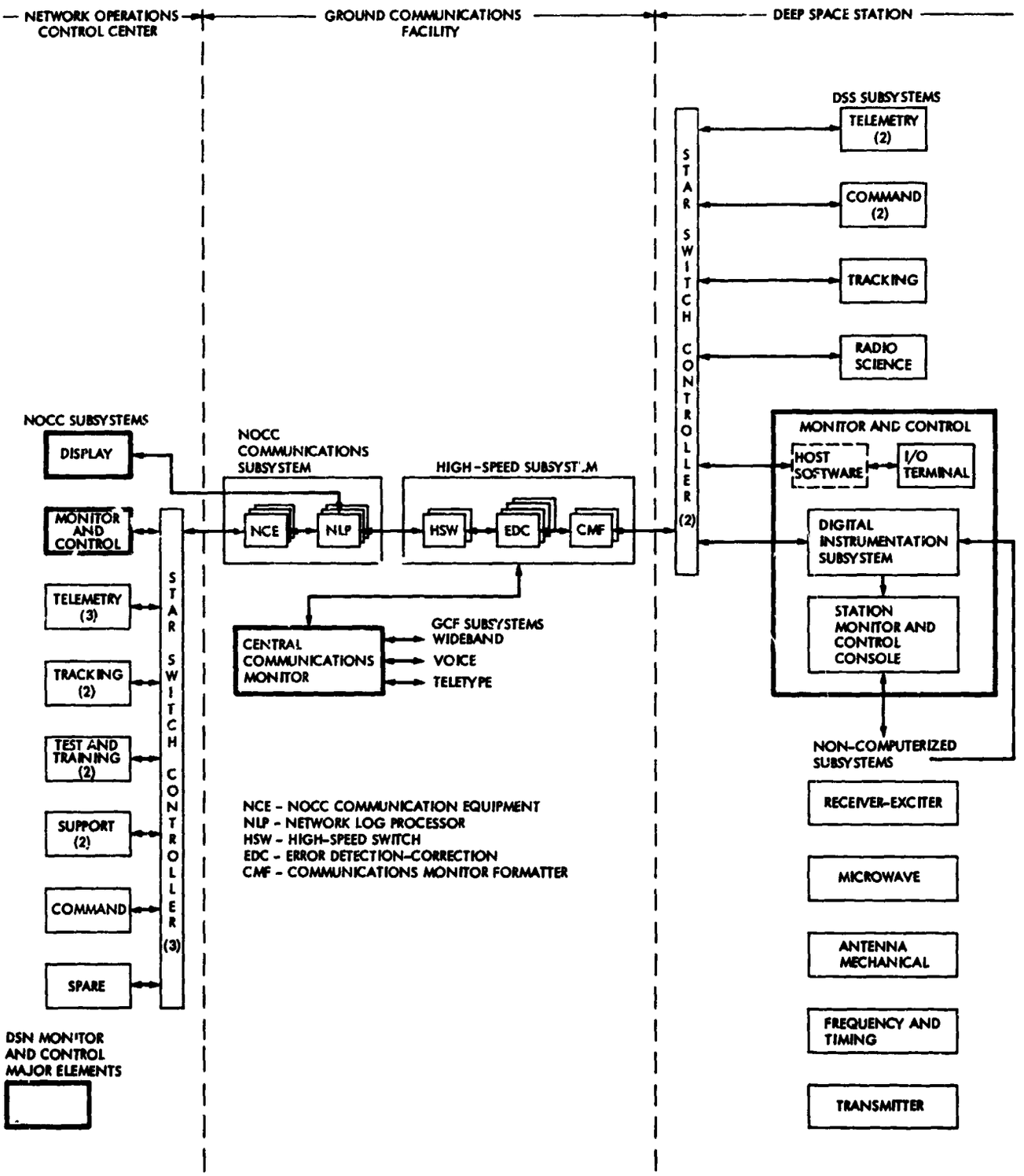

Fig. 1. DSN Monitor and Control System, Mark III-78

Viking Continuation Mission Support

R. L. Gillette
Deep Space Network Operations Section

This article covers the period from 1 July through 31 August 1978. It reports on DSN support of Viking spacecraft activities during the period and continues reporting on the DSN Viking Command and Tracking support.

I. Viking Operations

A. Status

The Viking Orbiter 2 (VO-2) mission ended during this reporting period after a severe gas leak depleted its remaining supply of attitude stabilizing gas. On 20 July, the VO-2 spacecraft was brought out of its roll-drift mode of operation to collect its last sequence of scientific observations of Mars. On 24 July the VO-2 spacecraft developed a severe gas leak in the positive roll valve, and on 25 July drifted off sun acquisition.

The Mars mission officially ended for VO-2 at 11:02 p.m. on 25 July when radio signals from the spacecraft ceased. Launched from Earth on 20 August 1975, VO-2 will now slowly tumble about Mars for at least 50 years before crashing to the surface.

The Viking Orbiter 1 (VO-1) spacecraft continued to operate normally during this reporting period as it collected and returned to Earth weather data and Mars photos as well as relaying to Earth data from the two Viking Landers.

The Viking Landers continue to operate in an automatic mode of operation as they collect and relay to Earth, via VO-1, Mars weather information and photos.

B. Radio Science

Radio Science activities and experimentation continued during July and August. These activities include near-simultaneous Lander/Orbit ranging, VO-1 Earth occultation coverage and the Gravity Field Experiment.

II. Network Support

Table 1 shows the DSN tracking support for January through August 1978. A significant decrease in tracking support is notable in August. This is primarily due to the increase in tracking support required from higher priority projects such as the Voyager and Pioneer Venus Missions. The Viking Project will continue to have major conflicts with other projects for tracking support during the Continuation Mission.

Table 2 gives the total number of commands transmitted by the DSN for Viking Project during January through August 1978. The reduction in the number of commands beginning in June reflects the reduction in Viking operation activity anticipated during the Continuation Mission.

Figure 1 shows the performance of the DSN delivery of the telemetry Intermediate Data Record (IDR) during January 1977 through August 1978. The IDR is a magnetic tape,

produced by the DSN, of digital telemetry data. As a goal, within existing time constraints, the DSN attempts to provide 100 percent of the data recorded at the Deep Space Station on the Digital Original Data Record (DODR) magnetic tape. IDR's are required to be delivered within 24 hours following the end of a station pass.

During July and August 1978, the IDR delivery time significantly improved from the previous months. The delivery time dropped from 23 hours to under 7 hours.

In May of 1978 a new position was created titled DSN Data Records Engineer. The primary function of the Data Records Engineer is to coordinate the data record (IDR) production conflicts among the many DSN projects, including Viking. The improvement in IDR delivery times can be attributed to the coordination efforts of the DSN Data Records Engineer.

The percent of telemetry data delivered to the project also increased during July and August with an average of 99.1 percent of telemetry data delivered.

Table 1. DSN tracking support 1978

DSS	Jan	Feb	Mar	Apr	May	Jun	Jul	Aug
11	8[a] 72[b]	–	19 167	–	18 164	1 1	2 13	–
12	–	4 13	5 22	1 8	–	–	–	–
14	40 319	25 218	37 272	47 365	25 231	34 242	14 89	13 85
42	22 166	23 76	30 201	30 192	2 4	–	2 9	1 3
43	57 294	14 207	15 68	27 163	40 281	46 346	51 449	23 135
44	–	11 51	6 43	–	11 77	3 17	–	3 11
61	10 88	38 243	25 281	15 159	2 26	–	–	1 5
62	61 27	2 25	3 22	3 29	8 75	3 33	1 7	1 9
63	13 101	21 181	30 293	42 440	26 206	41 343	40 291	16 130
Total	156 1067	138 1014	170 1369	165 1356	132 1064	128 982	110 858	58 378

[a]Number of tracks the summation of all Viking spacecraft tracked.
[b]Track time: scheduled station support in hours.

Table 2. Number of commands transmitted in the Viking mission during January through August 1978

DSS	JAN	FEB	MAR	APR	MAY	JUN	JUL	AUG
11	1947	–	119	–	1628	6	0	–
12	–	1	1	374	–	–	–	–
14	4565	1079	1326	3032	2845	1214	870	562
42	1447	1305	261	1079	0	0	0	0
43	1593	1732	124	275	1326	1567	791	7
44	–	255	3	–	373	0	–	30
61	992	3548	1073	1503	0	0	–	0
62	1	1006	461	73	0	960	0	683
63	895	128	2597	4005	669	2451	2984	2073
TOTAL	11440	9054	5965	10341	6841	6198	4645	3355

Fig. 1. Viking telem.: y IDR performance

Pioneer Venus Mission Support

A. C. Bouck
DSN Operations Section

This article reports on activities within the Deep Space Network (DSN) to prepare for the Pioneer Venus Multiprobe Venusian Encounter.

I. Mission Description

The Pioneer Venus Multiprobe Mission is designed to investigate the Venusian atmosphere down to the lowest scale height above the surface (probe survival after impact is not a mission requirement). The mission consists of a Large Probe, three Small Probes and the Bus. The Bus is the mother spacecraft that carried and supported the probes from launch until probe separation.

The four probes are individual spacecraft and transmit their data directly to Earth. The Large Probe carries seven scientific instruments, a radio receiver for two-way doppler tracking only, and transmits data at 256 or 128 bits per second. The Small Probes are identical. Each carries three scientific instruments and transmits data at 64 or 16 bits per second. Their reference frequency for one-way doppler tracking is provided by stable oscillators. Each probe will begin transmission about 22 minutes prior to entering the atmosphere.

II. DSN Entry Support

The DSN will meet one of its greatest challenges on December 9, 1978. In a brief 2 hours, the 64-meter Deep Space Stations (DSS) at Goldstone, California (DSS 14) and Canberra, Australia (DSS 43) must acquire and collect data in real time from four probes that have never been acquired in flight. After the probes reach the surface, DSSs 14 and 43 must support the Bus entry along with any surviving probes. The Bus will be supported by two 26-meter DSSs during the probe descent phase.

III. DSN Implementation at DSSs 14 and 43 for Multiprobe Entry

The following special implementation was required for the Pioneer Venus Multiprobe entry:

(1) Spectral Signal Indicators (SSI):

Three special spectrum indicators (SSI) with microprocessor controls were designed and installed to rapidly identify the probe signals and provide accurate frequencies to acquire lock on the DSN closed loop receivers. The SSI is the key to performing the mission.

(2) Multiprobe Simulator:

The simulator was required for mission test and training. It generates the four Probe's S-band signals, and

simulates the entry doppler profile and telemetry bit rate changes in accordance with the mission timeline.

(3) Open Loop Receivers (OLR)

Two OLRs were added making a total of four 300-kHz bandwidth OLRs. They are the signal input to the SSI and provide predetected signals to the analog recorders for telemetry data recovery.

(4) Venus Wind Experiment Receiver/Recorder:

A special 2-mHz open loop receiver and a 12-megabit-per-second digital recording assembly that simultaneously records the signals from the four Probes and Bus plus two calibration tones were installed to support measurement of the Venus winds using long baseline interferometry techniques.

(5) A fifth closed loop receiver (RCVR 7) and subcarrier demodulator assembly (SDA 7), and three Programmable Oscillator Control Assemblies (POCA) were also installed.

(6) The telemetry processor software was modified to accommodate dual-channel convolutional decoding in a single computer. This added the capability of processing the four Probe data streams simultaneously.

IV. Entry Procedure Development

Entry procedures were developed by the Pioneer Network Operations Project Engineer (NOPE) and three DSS shift supervisors who will support the actual entry event. With a preliminary version of the procedure complete, the authors went to DSS 14 and performed the sequence using the procedure with regular station personnel. After three days of testing and rewriting, the procedures were ready for use in training tests. One major discovery was that station operations during the entry event required a crew complement of 16 to 17 operators as compared to a normal crew complement of 5 to 7 operators It was decided that entry would be supported by combining two crews plus additional personnel from other crews.

V. Unique Entry Support Features

A. Mission Control

The probe entry phase, by its very nature, precludes any project direction. The DSS must therefore support this phase on their own.

B. Dual Uplinks to the Large Probe

To maximize the probability of acquiring postentry two-way lock with the Large Probe in a minimum amount of time, both DSS 14 and 43 will simultaneously transmit to the probe. The real-time doppler data will be utilized to determine which DSS has captured the probe receiver.

VI. Entry Sequence of Events

In Table 1, the uncertainties in probe event times are (1) ±22 seconds for preentry events, and (2) ±60 seconds for entry and postentry events.

Table 1. Time order of the major entry events

	Time (GMT)	DSS	Event
1.	1530		Large Probe receiver on.
2.	1600	14	Antenna on point-Bus in view.
3.	1618	14	Perform Large Probe uplink acquisition.
4.	1730	43	Venus rise.
5.	1748	14/43	Perform minus 60-min checklist.
6.	1825	14/43	Start prime analog (PPR) and digital (DRA) recorders Put doppler data to line.
7.	182613		Large Probe carrier on.
		14	Acquire on SSI, lock receiver 3 (2-way doppler).
		43	Acquire on SSI, lock receiver 3 (3-way doppler).
8.	1830	14/43	Start backup PPR and DRA recorders.
9.	183113		Small Probe 2 carrier on.
		14/43	Acquire on SSI, lock receiver 2.
10.	183113	14/43	Large Probe subcarrier on; lock telemetry.
11.	183401		Small Probe 3 carrier on.
		14/43	Acquire on SSI, lock receiver 7
12.	183613	14/43	Small Probe 2 subcarrier on; lock telemetry.
13.	183708		Small Probe 1 carrier on.
		14/43	Acquire on SSI, lock receiver 1
14.	183901	14/43	Small Probe 3 subcarrier on; lock telemetry
15.	184013	43	Reconfigure for Large Probe bit rate change.
16.	184313	43	Large Probe bit rate change; lock telemetry.
17.	1845	43	Transmitter on-start Large Probe postentry uplink sweep.
18.	1846	14	Start Large Probe postentry uplink sweep.
19.	184813	14/43	Large Probe entry; receiver 3 out of lock.
20.	184825	14/43	Acquire on SSI, lock receiver 3 (1-way doppler).
21.	184830	14/43	Large Probe bit rate change; lock telemetry.
22.	1851	14/43	Receiver 3 out of lock; acquire on SSI, lock receiver 3 (2-way doppler).
23.	185130	TRK	Inform DSS of correct doppler mode; 3-way DSS turns off transmitter.
24.	185313	14/43	Small Probe 2 entry; receiver 2 out of lock.
25.	185326	14/43	Acquire on SSI, lock receiver 2.
26.	185601	14/43	Small Probe 3 entry; receiver 7 out of lock.
27.	185614	14/43	Acquire on SSI, lock receiver 7.
28.	185918	14/43	Small Probe 1 entry; receiver 1 out of lock.
29.	185931	14/43	Acquire on SSI, lock receiver 1.
30.	190413	14/43	Large Probe parachute jettison. Possible receiver 3 out of lock due to doppler shift.
31.	1906	43	Reconfigure for Small Probe 2 bit rate change.
32.	1909	43	Reconfigure for Small Probe 3 bit rate change.
33.	190913	14/43	Small Probe 2 bit rate change; lock telemetry.
34.	1912	43	Reconfigure for Small Probe 1 bit rate change.
35.	191201	14/43	Small Probe 3 bit rate change; lock telemetry.
36.	191518	14/43	Small Probe 1 bit rate change; lock telemetry.
37.	1925	14/43	Prime PPR tape change.
38.	1930	14/43	Backup PPR tape change.
39.	1943	14/43	Large Probe impact.
40.	1945	14/43	Prime DRA tape change.
41.	1948	14	Reconfigure receiver 3 for Bus; lock telemetry.
42.	1949	14/43	Small Probe 2 impact.
43.	1950	14/43	Backup DRA tape change.
44.	1953	14	Bus bit rate change; lock telemetry.
45.	1953	14/43	Small Probe 3 impact.
46.	1954	43	Reconfigure receiver 2 for Bus – lock telemetry.
47.	1955	14/43	Small Probe 1 impact.
48.	2024	14/43	Bus entry.
49.	2025	14/43	Prime PPR tape change.
50.	2028	14/43	Bus burns up; loss of signal.

Helios Mission Support

P. S. Goodwin
TDA Mission Support

W. N. Jensen and G. M. Rockwell
Deep Space Network Operations Section

This article reports on activities of the DSN Network Operations Organization in support of the Helios Project from 15 August 1978 through 15 October 1978.

I. Introduction

This article is the twenty-fourth in a continuing series of reports that discuss Deep Space Network support of Helios Mission Operations. Included in this article is information on the upcoming eighth perihelion of Helios-1 and the sixth perihelion of Helios-2, science experiments, 22-bit error polynomial code (EPC) testing and other mission-related activities.

II. Mission Operations and Status

On 7 September 1978, commands were sent to Helios-1 to turn on Experiment 9. Experiment 9 had been off since 2 July 1978 due to a limitation in available regulator output power. The experiment was fully configured and science data had been received for more than one hour when DSS 44 (Honeysuckle Creek, Australia), which was tracking the spacecraft, reported a loss of downlink at 22:50:25 Universal Time Coordinated (UTC) on 7 September. As a result, a spacecraft emergency was declared at 23:10 UTC and 64-meter coverage requested. On 8 September at 00:39:37 UTC, DSS 43 (Tidbinbilla, Australia) acquired the downlink. After evaluating the first telemetry data, it was discovered the spacecraft's tenth regulator switch had occurred, which caused the turn-off of the non-essential bus, changed numerous status bits and off pointed the High-Gain Antenna. After sending several hundred commands, the spacecraft and its experiments, except for Experiment 9, was reconfigured with the High-Gain Antenna back on Earth point. On 8 September 1978 at 09:00 UTC, the emergency was lifted. Two possible causes for this regulator switch have been identified:

(1) The switch might have been triggered by a solar event that was reported at the Space Environments Services Center, Boulder, Colorado, at approximately the same time period.

(2) Experiment 9 does not have a current limiter for protection and a stuck stepper motor might have caused an overload condition. Experiment 9 will be left off until the circumstances can be clarified with the experimenter.

On 26 October 1978, the Helios-1 spacecraft will enter its eighth perihelion period, which will last until 3 November.

More information concerning this event will be recorded in future articles.

The Helios-2 spacecraft has performed nominally for this period with no significant occurrences or problems. The spacecraft entered its sixth perihelion period on 8 October 1978. Helios-2 entered blackout on 9 October while being tracked by DSS 67/68 (Weilheim, Germany). This earlier than expected blackout was probably due to high solar activity. The spacecraft was at a Sun-Earth-Probe (SEP) angle of 4.1 degrees at blackout. Assuming a symmetrical exit angle, the spacecraft was configured for a 13-day unattended operation period with memory storage covering. Helios-2 was configured in data mode 4, format 3, bit rate of 8 bits per second (bps) and sequence 17. Blackout exit is scheduled to occur on 22 October 1978. As with Helios-1, more information will be available for a future article.

Helios-2 also passed its 1001st day in orbit on 12 October 1978.

Overall coverage for Helios-1 and Helios-2 for this period is listed in Table 1.

III. Special Activities

A. Support of On-Board and Ground Experiments

In conjunction with the perihelion and superior conjunction periods, science data will be collected during times discussed earlier. The prime data types will be faraday rotation data and ellipticity data for Experiment 12. Also solar wind data will be collected during the same period.

B. German Space Operations Center (GSOC) Conversion to the 22-Bit Error Polynomial Code (EPC) and the Mark III Command System

As reported in the last article (Ref. 1), testing has continued on the 22-bit EPC interfaces and Mark III Command System throughout this period. Overall, the testing has gone well. On 3 October, the first demonstration track was performed by DSS 44 while tracking Helios-1 to verify that GSOC was capable of processing telemetry, monitor, and command data while in the 22-bit EPC mode. The monitor software at the Network Operations Control Center (NOCC) was, unfortunately, not available in time for this test, and the Mark III Command System performance was hampered by certain anomalies discovered in the station's Command Processor Assembly's test software. These anomalies affected command transmission to the spacecraft and are being corrected. The interfaces between GSOC, JPL, and DSS 44 worked well in the 22-bit EPC mode, and telemetry and command data flowed without difficulty. Another demonstration was conducted on 5 October with basically the same results. On 8 October, demonstration tracks with DSS 62 (Cabreros, Spain) tracking Helios-1 and DSS 63 (Madrid, Spain) tracking Helios-2 were conducted. The purpose here was to verify that GSOC could process both Helios-1 and Helios-2 telemetry data, while in the 22-bit EPC configuration. This test was successful with no problems encountered. The most recent test was a telemetry and monitor test with DSS 44 tracking Helios-1 and DSS 14 (Goldstone, California) tracking Helios-2. This test followed the same format as the telemetry test above, but with the addition of one monitor data stream from each station. This test proved successful and GSOC processed both telemetry and monitor data from each station. Future tests (demonstration tracks) are scheduled to check out the Mark III Command System following the correction of DSN software. These tests will be reported in a future report.

References

1. Goodwin, P. S., Jensen, W. N., and Rockwell G. M., "Helios Mission Support," in *The Deep Space Network Progress Report 42-47*, pp. 26-28, Jet Propulsion Laboratory, Pasadena, CA, 15 October 1978.

Table 1. Helios tracking coverage

Month	Spacecraft	Station type	Number of tracks	Tracking time (h:min)
August	Helios-1	26 meter	31	147:13
		64 meter	0	00:00
	Helios-2	26 meter	4	20:47
		64 meter	25	84:41
September	Helios-1	26 meter	27	139:40
		64 meter	2	8:25
	Helios-2	26 meter	0	00:00
		64 meter	21	91:02

Convolutional Coding Results for the MVM '73 X-Band Telemetry Experiment

J. W. Layland
Communications Systems Research Section

This article presents results of simulation of several short-constraint-length convolutional codes using a noisy symbol stream obtained via the turnaround ranging channels of the MVM'73 spacecraft. First operational use of this coding technique is on the Voyager mission. The relative performance of these codes in this environment is as previously predicted from computer-based simulations.

This short article presents the results of simulations of several short-constraint-length convolutional codes using 70 min of noisy 5.8-kbps symbol stream recorded by the R&D 930 computer at DSS 14 on Jan 15, 1974. This data was obtained as part of an experiment intended to define the performance to be expected from X-band telemetry on the Voyager and subsequent missions. The simulated telemetry stream was originated on the ground and returned via the turnaround ranging channels of the MVM'73 spacecraft at both X- and S-band (Ref. 1). The same experiment was later performed with Viking (Ref. 2).

The data stream consisted of the repeated sequence 111010, modulated on a subcarrier. This sequence is a codeword of the K=7, rate 1/2 convolutional code now flying on Voyager, and also of two rate 1/3 codes at K=4, and K=5. The signal was processed at the time of reception as an uncoded bit stream and also via a hardware Viterbi decoder for the K=7, rate 1/2 code. It had been initially intended to also operate the JPL-designed K=5, rate 1/3 decoder (Ref. 3) in real-time, but this was not in fact pursued. The data recorded by the on-site SDS-930 computer as 6-bit quantized symbols was subsequently converted to a stream of 4-bit quantized channel-noise samples by extraction of the known data stream. This conversion was done to simplify processing in software through a variety of short-constraint-length convolutional codes. The use of 4-bit quantization compressed this data to two virtually full magnetic tapes, one each for S-band and X-band data.

Decoding from these tapes was performed using a software decoder in the Sigma 5 computer, at constraint lengths K=3 to K=9, rates 1/2 and 1/3 (Ref. 4 describes a 930 version of this decoder). The data was blocked into 5-min segments of approximately 2×10^6 symbols to obtain statistical averages for the coded P_e without masking variations that had been observed in the signal-to-noise ratio during the real-time experiment. Figure 1 shows a time-trace of the decoding results for the S-band data at rates 1/2 and 1/3. Figure 2 shows a similar time trace for the X-band data, decoded at rate 1/2 only. The SNR at S-band was too high to permit statistically significant results for the rate 1/3 codes.

The traces for several of the codes are not complete, work having been stopped pending resolution of the difference between hardware and software decoder performance. This

problem has since been resolved (Ref. 5) and the software results shown to be correct, at least at K=7, rate 1/2, X-band.

Figure 3 summarizes the coded bit error probability seen for these codes as a "function" of the signal-to-noise ratio estimated by way of the (uncoded) symbol error rate. There are no real surprises in this figure. The performance of all codes tested, either rate 1/2 or rate 1/3, is comparable to their performance as seen in earlier simulation with computer-generated noise (Ref. 6).

References

1. Springett, J. C., and Kollar, F. J., "Results of the MVM'73 X-Band Telemetry Experiment," Document 615-149, Jet Propulsion Laboratory, Pasadena, Calif., May 1974 (an internal document).
2. Weber, W. J., et al., *Viking X-Band Telemetry Experiment Final Report*, TM 33-794, Jet Propulsion Laboratory, Pasadena, Calif., Sept. 1976.
3. Lushbaugh, W., *Hardware Version of an Optimum Convolutional Decoder*, TR 32-1526, Vol. II, pp. 49-55. Jet Propulsion Laboratory, Pasadena, Calif., April 1971.
4. Layland, J. W., Capabilities of an All-Software Optimum Convolutional Decoder, SPS 37-62, Vol. II, Jet Propulsion Laboratory, Pasadena, Calif., Mar. 1970.
5. Omura, Jim K., and Butman, S. A., "Foldover Effects on Viterbi Decoding," PR 42-34, pp. 27-32, Jet Propulsion Laboratory, Pasadena, Calif., Aug. 1976.
6. Layland, J. W., Performance of Short Constraint-Length Convolutional Codes and a Heuristic Code-Construction Algorithm, SPS 37-64, Vol. II, pp. 41-44, Jet Propulsion Laboratory, Pasadena, Calif., Aug. 31, 1970.

Acknowledgement

The author is indebted to J. C. Springett and F. J. Kollar for providing the data set, and to J. K. Omura and S. A. Butman for resolving the discrepancy between the hardware and software K=7 results.

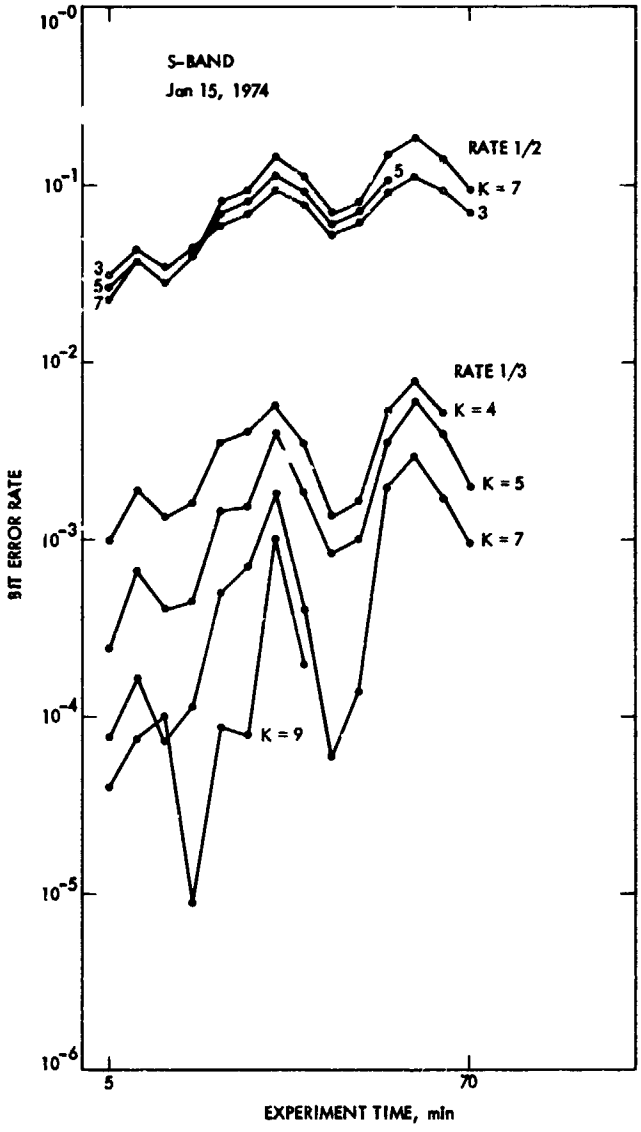

Fig. 1. Decoded bit error rate for S-band data

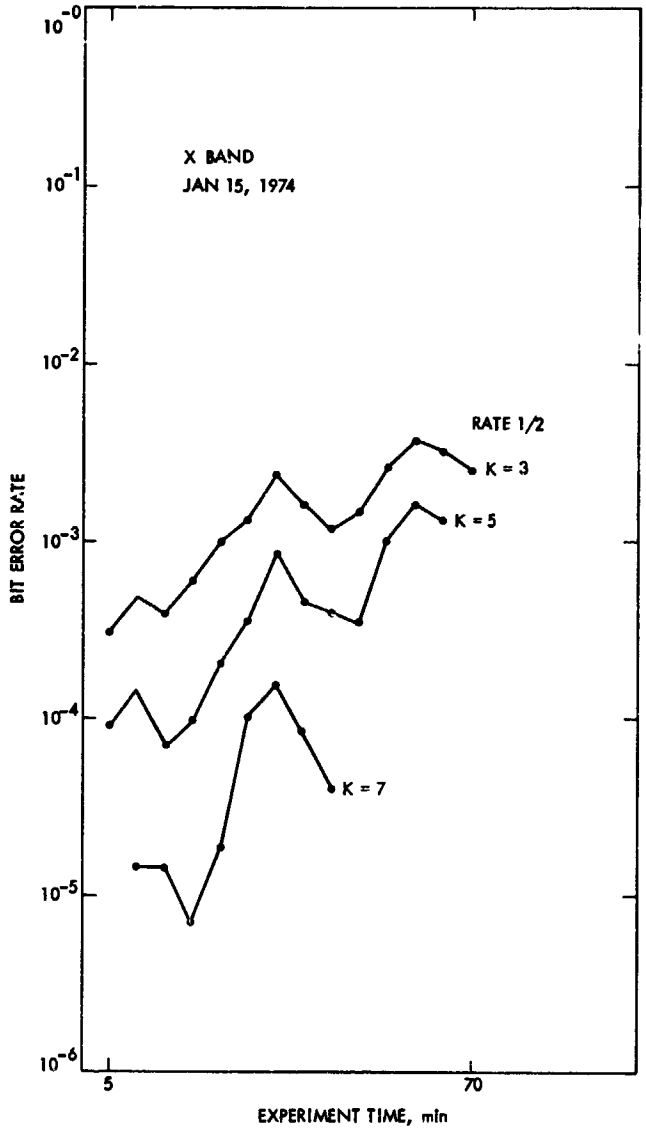

Fig. 2. Decoded bit error rate for X-band data

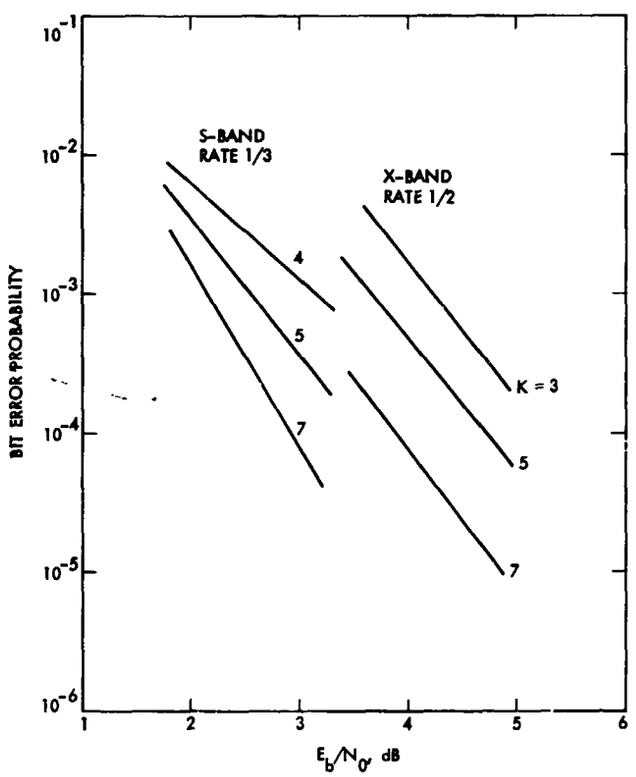

Fig. 3. Coded bit error performance vs SNR

D7

N79-16007

Microwave Radiometer Measurement of Water Vapor Path Delay: Data Reduction Techniques

E. S. Claflin, S. C. Wu, and G. M. Resch
Tracking Systems and Applications Section

Unmodeled electrical path delay from atmospheric water vapor is a limiting error source in geodetic measurements made with very long baseline interferometry and in radio ranging to spacecraft. A dual channel water vapor radiometer, operating near the 22.235-GHz water vapor line, is capable of measuring water vapor-induced delay with good accuracy under most weather conditions. Theory shows that water vapor path delay ΔL_v is proportional to a linear combination of saturation-corrected sky brightness temperatures, measured on and off the water vapor line. The second, off-line, channel removes the effects of emission from liquid water droplets in clouds as well as most of the oxygen emission. Tipping curves remove instrumental error. Sky brightness temperatures are saturation-corrected or "linearized" using estimates of effective sky temperature made from surface temperature. Coefficients in the expression for path delay ΔL_v are functions of surface temperature, pressure, and water vapor density, allowing use of our data reduction algorithm at any altitude and in any climate. Coefficients are found by two methods: (1) from a regression analysis of measured brightness temperatures versus radiosonde measured delay, and (2) from a regression of theoretical brightness temperatures versus radiosonde measured delay. Regression solutions are constrained to remove liquid water contributions and to give the correct slope (i.e., one) for radiometer versus radiosonde path delay.

I. Introduction

Very long baseline interferometry (VLBI) and other extra-terrestrial, microwave, geodetic techniques have potential accuracies at the few centimeter level (Ref. 1). Propagation media effects constitute a limiting error source, however, and must be compensated for to achieve the highest accuracy otherwise inherent in present and planned systems. In particular, one must devise a way to compensate for tropospheric water vapor. Water vapor induced path delay in the zenith direction can vary from less than 1 to more than 30 centimeters depending on climate and weather.

Under favorable conditions, water vapor delay can be solved for as part of the final fitting of residuals in the VLBI data reduction process. If baseline geometry is not favorable, the solve-for procedure will degrade accuracy appreciably.

Moreover, the solve-for solution breaks down if changes in water vapor delay occur rapidly or if the atmosphere has large horizontal inhomogeneities. An independent way to measure delay from tropospheric water vapor is needed.

From among a number of candidate measuring techniques, we have found that the most satisfactory is passive microwave radiometry. A microwave radiometer will operate day or night and under all weather conditions except rain or heavy snow. Spatially, measurements can be made in all directions that are more than a few beamwidths from the horizon and from the sun. Microwave radiometry will, in the future, also be applicable to VLBI geodesy with satellite radio sources and to radio ranging for navigation of interplanetary spacecraft. The purpose of this paper is to present techniques for conversion of radiometer data to water vapor path delay. A discussion of errors will be presented in a later paper.

II. Background

A solution of the radiative transfer equation governing propagation of microwave radiation downward through a nonscattering atmosphere in thermodynamic equilibrium is (Ref. 2)

$$T_B = T_c\, e^{-\tau(\infty)} + \int_0^{\infty} T\alpha\, e^{-\tau(s)}\, ds \qquad (1)$$

where

$$\tau(s) = \int_0^{s} \alpha\, ds$$

is the optical depth, α is the absorption coefficient (distance^{-1}), s is distance upward along the signal path, T is physical temperature of the air, T_B is the sky brightness temperature, and T_c is the cosmic blackbody temperature of about 2.8 K. Typical half-power antenna beamwidths of 5 to 10 degrees are large enough that all celestial sources of radiation are negligible except for the sun.

Important contributions to α are made by atmospheric water vapor, oxygen, and the liquid water droplets in clouds or fog. Water vapor has a spectral line at 22.235 Ghz. Sensitivity to water vapor is achieved by choosing a primary frequency on or near this line. The liquid water contribution from clouds is removed by using a second frequency channel and then linearly combining sky temperatures from both channels. We find that it is sufficiently accurate to assume an f^2 frequency dependence for the liquid water absorption coefficient.[1] The oxygen contribution is from a complex of spectral lines near 60 GHz and has a frequency dependence which is also approximately f^2. About 82 percent of the oxygen contribution is removed by the f^2 dependence assumed for liquid emission. This is fortuitous because oxygen emission also depends on atmospheric temperature, a quantity subject to estimation error. The remaining 18 percent of the oxygen contribution is removed by a small term proportional to air mass in the expression for water vapor path delay. At one air mass this term is approximately −0.4 cm path delay.

A related matter that has already been investigated in some detail is optimal choice of frequency pair for the two radiometer channels. To retrieve water vapor path delay with highest accuracy, it is necessary to use a frequency pair which minimizes error from all sources. No single frequency pair is ideal under all conditions; however, we recognize that a very important consideration is that a frequency pair be chosen which minimizes variation with altitude of the weighting function $W'(s)$ (Ref. 3):

$$W'(s) = \frac{T(T - T_c)}{\rho}\left[\frac{\alpha_{v,1}}{f_1^2} - \frac{\alpha_{v,2}}{f_2^2}\right] \qquad (2)$$

where α_v is the absorption coefficient for water vapor and ρ is water vapor density. The penalty for a nonconstant Eq. (2) along the observing path is appreciable error whenever the water vapor altitude distribution varies markedly from some calibration distribution. Such variations appear to be most common in coastal regions, where layering of marine and continental air is a frequent occurrence. Optimal choice of frequency pairs has been discussed by Wu (Ref. 3). Frequency pairs of 20.3/31.4, 20.0/26.5, and 24.5/31.4 GHz are all near optimal for minimizing variations in weighting function (Eq. 2) with altitude.

[1] Liquid water absorption coefficient frequency dependence was calculated for the case of droplets small compared with wavelength (Rayleigh scattering). The dependence is very nearly f^2, but is slightly affected by temperature (Refs. 4, 5). For a 22.235/31.4-GHz frequency pair, deviations from f^2 behavior will cause an error in path delay of less than 0.7 cm even under the extreme conditions of 1000 μm liquid water, 20-degree elevation angle, and temperature of 0°C. Note also that path delay from liquid water is negligible; 1000 μm of vertical columnar liquid water at 20-degree elevation angle causes path delay of less than 0.5 cm (Ref. 6). For a next generation system, these effects could be estimated to refine the total delay correction.

III. Outline of Technique

The data reduction system developed here can be separated into two parts or activities. The first part comprises techniques for converting raw radiometer data and surface temperature into linearized sky brightness temperatures. An important element of this procedure is the use of tipping curves to provide an instrumental calibration.

The second part is calculation of suitable coefficients for use in finding path delay. Two methods will be discussed for calculating coefficients, both using a regression analysis. In each case the coefficients are adjusted for differing climatic conditions by measurements of surface temperature, pressure, and relative humidity.

IV. Linearized Brightness Temperature and Water Vapor Path Delay

Presence of the exponential terms in Eq. (1) prevents sky brightness temperature from increasing linearly with increasing water vapor path delay. In the limit of small opacities, the relation is linear. In the limit of extremely high opacities, sky brightness temperature becomes equal to surface atmospheric temperature (saturates) and is completely insensitive to changes in water vapor path delay. Between these limits it is possible to "linearize" (saturation-correct) brightness temperature. The purpose of linearization is to transform the calculation of path delay into the familiar problem of solving two linear equations in two unknowns. (The two unknowns are water vapor path delay and integrated liquid water.)

If the linearized brightness temperature T_B' is defined by

$$T_B' = T_c\,[1 - \tau(\infty)] + \int_0^\infty T\alpha\,ds$$

$$= T_c + \int_0^\infty (T - T_c)\,\alpha\,ds \qquad (3)$$

then linearized brightness temperature may be calculated from measured brightness temperature T_B using the following relation derived from Eqs. (1) and (3) (Ref. 3):

$$T_B' = T_c - (T_{eff}' - T_c)\ln\left(1 - \frac{T_B - T_c}{T_{eff} - T_c}\right) \qquad (4)$$

with

$$T_{eff} = \frac{\int_0^\infty T\,\alpha\,e^{-\tau(s)}\,ds}{\int_0^\infty \alpha\,e^{-\tau(s)}\,ds} \qquad (5)$$

$$T_{eff}' = \frac{\int_0^\infty T\,\alpha\,ds}{\int_0^\infty \alpha\,ds} \qquad (6)$$

For small opacities, $T_{eff}' \approx T_{eff}$. For large zenith opacities or small elevation angles, $T_{eff}' < T_{eff}$. Since atmospheric temperature is readily accessible only at the ground, surface values must be used to estimate T_{eff}. A simple expression

$$T_{eff} = T_{eff}' = k_e T \qquad (7)$$

(where T is absolute surface temperature) is sufficient for dry climates. k_e is a function of frequency and can be found by integrating radiosonde profiles with Eq. (6). Typically $0.92 < k_e < 0.95$. More accurate, but more complex, schemes for estimating T_{eff} and T_{eff}' can be devised.

T_B', the linearized brightness temperature, is not very sensitive to T_{eff} and T_{eff}'. Figure 1 shows the linearization correction $T_B' - T_B$ as a function of T_B for three different estimates of $T_{eff} = T_{eff}'$. The correction becomes a significant error source only at very high sky temperatures. Observed zenith sky brightness temperatures at 22.235 GHz have been in the range 13 to 100 K. At 31.4 GHz the range has been 11 to 45 K. The corresponding range of zenith path delays covered by these observations was from 2 to 30 cm.

Wu (Ref. 3) has shown that for a dual channel radiometer, path delay is given by

$$\Delta L_v = (b_0' + b_1 T_{B,1}' + b_2 T_{B,2}')/W'(0) \qquad (8)$$

where

$$b_0' = Gb_0 - T_c(b_1 + b_2) \qquad (9)$$

$$G = m(P/\bar{P})^2\,(\bar{T}/T)^{1.85} \qquad (10)$$

b_0, b_1, b_2 = constants

P = surface pressure: force/area

T = surface temperature

$T'_{B,1}$ and $T'_{B,2}$ are derived from measured brightness temperatures at the two frequencies using Eq. (4). $W'(0)$ is the weighting function of Eq. (2) evaluated at the surface to adjust path delay for varying values of surface temperature, pressure, and water vapor density. The variable G adjusts for changes in air mass m and for changes in the oxygen absorption coefficient with changes in surface temperature and pressure. $\overline{T}$ and $\overline{P}$ are nominal surface values, but are best chosen to be representative of the calibrating or operating conditions. Expressions for the water vapor absorption coefficient α_v can be found in Waters (Ref. 2) and Westwater (Ref. 7). The coefficients b_0, b_1, b_2 can be determined either from theory and a suitable ensemble of radiosonde profiles or from regression of measured sky temperatures against path delays from simultaneous radiosonde data. These methods will be discussed in a later section.

For convenient routine application, Eqs. (8), (9), and (10) can be written as

$$\Delta L_v = a'_0 m - T'_c + a_1 T'_{B,1} + a_2 T'_{B,2} \tag{11}$$

$$a'_0 = \frac{b_0 (P/\overline{P})^2 (\overline{T}/T)^{1.85}}{W'(0)} \tag{12}$$

$$T'_c = \frac{T_c(b_1 + b_2)}{W'(0)} \tag{13}$$

$$a_1 = b_1/W'(0) \tag{14}$$

$$a_2 = b_2/W'(0) \tag{15}$$

and a table of coefficients a'_0, T'_c, a_1, a_2 prepared for suitable choices of P, T, and ρ values. We have found that sufficient resolution is provided by increments of 20 mb (2000 N/m^2) in P, 10°C in T, and relative humidities of 20, 50 and 80 percent.

V. Measurement of Sky Brightness Temperature

Radiometer output is an analog signal which varies linearly with input signal power. Since the constant of proportionality is gain dependent, every radiometer contains two reference loads at carefully measured physical temperatures to establish a brightness temperature calibration. If the sky brightness temperature is T_B, the ambient or base load temperature T_A, and the hot load temperature T_H, then the corresponding number of counts N_B, N_A, N_H (from an analog to digital converter) are related to brightness temperature by

$$T_B = T_A + (T_H - T_A)\gamma \tag{16}$$

$$\gamma = (N_B - N_A)/(N_H - N_A) \tag{17}$$

In practice Eq. (16) is imperfect because of losses and reflections in the horn, waveguide, and switching system. Figure 2 shows typical switches and signal paths for a radiometer. T^*_B, T^*_H, T^*_A are apparent brightness temperatures at the common input. We assume *a priori* that switch isolation is very good (typically the isolation is ~30 dB). Then

$$T^*_B = T_B \beta_B + T_{BL} \tag{18}$$

$$T^*_H = T_H \beta_H + T_{HL} \tag{19}$$

$$T^*_A = T_A \tag{20}$$

are expressions for the input temperatures for a simple linear model in which the input signal suffers attenuation β_i and receives augmentation T_{iL}. The β_i's and T_{iL}'s are temperature dependent. Temperature stabilization of the instrument should remove most of the variation in these parameters. Equation (20) assumes that the switch and waveguide temperatures are nearly the same as the ambient load temperature T_A.

Solving Eqs. (16), (18), (19), and (20) for T_B,

$$T_B = \beta_B^{-1} \left[(T_A - T_{BL}) + (T_H \beta_H + T_{HL} - T_A)\gamma \right] \tag{21}$$

Determination of the four instrumental constants β_B, β_H, T_{BL}, and T_{HL} is not straightforward either theoretically or experimentally. A simplified version of Eq. (21) can be written by assuming $\beta_B \simeq 1$ and $T_{BL} \simeq 0$, which implies negligible losses and reflections between antenna and receiver input. The instrumental constants are then replaced by the "hot load correction," $\Delta T_H = T_H(\beta_H - 1) + T_{HL}$, so that

$$T_B = T_A + (T_H + \Delta T_H - T_A)\gamma \tag{22}$$

The single constant ΔT_H can be found by performing "tipping curves" as outlined in the following section. Some variation in ΔT_H will occur with different brightness and physical temperatures because Eq. (22) is only an approximation to Eq. (21).

VI. Tipping Curves and the Hot Load Correction

Tipping curves are performed by taking measurements of sky brightness temperature at several elevation angles. When a straight line is fitted to linearized brightness temperatures from Eqs. (22) and (4) as a function of air mass, the expected intercept at zero air mass is T_c. Suppose the intercept has a different value $T'_B(0)$. ΔT_H must be adjusted to achieve the desired intercept. Figure 3 shows a straight line fit before (dashed) and after (solid) adjustment of ΔT_H. (The two lines intersect off the graph at $T'_B = T'_A$.)

If the hot load correction is initially taken to be zero, then one can show that

$$\Delta T_H = \frac{[T_c - T'_B(0)]\ [T_H - T_A]}{[T'_B(0) - T_A]} \tag{23}$$

is a good estimate of the required hot load correction. Corresponding sky brightness temperature correction is found from Eq. (22) to be

$$\Delta T_B = \Delta T_H \left(\frac{T_B - T_A}{T_H - T_A} \right) \tag{24}$$

New sky brightness temperatures $T_B + \Delta T_B$ are linearized with Eq. (4) and fitted again to a straight line. The process is repeated[2] as many times as necessary to adjust $T'_B(0)$, the intercept, to within about 0.1 K of T_c. Normally two or three iterations are sufficient. We generally use three points at 1, 1.5, and 2 air masses (90-, 42-, and 30-degree elevation angles) for tipping curves. Repeating the measurement at four points of the compass (different azimuths) provides redundancy in the data and averages over spatial gradients.

Various problems with the measurement system can cause a poor tipping curve. Quality criteria for a tipping curve are the value of the linear correlation coefficient, the size of the hot load correction and its agreement with a "historical" estimate, and the agreement of the estimated zenith path delay with those derived from tipping curves at other azimuths.

Experience with an instrument will show to what degree ΔT_H is constant for each channel. One can then estimate error incurred by using nominal values of ΔT_H to replace tipping curves.

In principle, the most meaningful delay is found by measurements along the line-of-sight to the radio source being observed. For an automated system, a horizon mask for each site and a solar ephemeris are needed to avoid pointing the instrument toward contaminating radiation. Under dry conditions, pointing along the line-of-sight is not likely to give measurable improvement over extrapolated zenith values. In fact, error may be introduced by sidelobe pickup and poorer performance of the data reduction algorithm at low elevation angles. We expect pointing to improve VLBI results under very humid, cloudy conditions.

VII. Coefficient Determination: Regression of Sky Brightness Temperatures Versus Radiosonde Path Delay

Water vapor delay is computed from a radiosonde profile with the expression (Refs. 8 and 9).

$$\Delta L'_v = (1.723 \times 10^{-3}\ \text{K-m}^3/\text{g}) \int_0^\infty \rho/T\, ds \tag{25}$$

where the prime indicates a radiosonde measurement.

---

[2]Equations (23) and (24) must be generalized slightly to take into account each new adjustment of the hot load temperature T_H.

If

$$T_{Hi} = T_H + \Delta T_{Hi}$$

$$\Delta T_{Hi} = \sum_{j=0}^{i} \Delta T_{Hj}^{\text{inc}}$$

and

$$\Delta T_{H0}^{\text{inc}} = 0$$

then

$$\Delta T_{H(i+1)}^{\text{inc}} = \frac{[T_c - T'_B(0)_i]\ [T_{Hi} - T_A]}{[T'_B(0)_i - T_A]} \tag{23a}$$

$$\Delta T_{B(i+1)} = \Delta T_{H(i+1)} \left(\frac{T_B - T_A}{T_H - T_A} \right) \tag{24a}$$

where $i = 0, 1, 2, \ldots$ is the iteration number and "inc" is incremental change.

Suppose a suitably representative group of radiosonde launches has been made, and sky brightness temperatures measured with a radiometer at the time of each launch. The coefficients b_0, b_1, b_2 of Eq. (8) and Eq. (9) may be found by minimizing:

$$S = \sum_i (\Delta L_{vi} - \Delta L'_{vi})^2 \tag{26}$$

with respect to b_0, b_1, and b_2, but subject to several constraints.

The first constraint ensures that background contributions are eliminated:

$$b_1/b_2 = -(f_2/f_1)^2 \tag{27}$$

Two more constraints enforce unity slope and zero intercept on the best-fit straight line of radiometer-measured to radiosonde-measured path delays:[3]

$$\sum_i \Delta L_{vi} = \sum_i \Delta L'_{vi} \tag{28}$$

$$\sum_i (\Delta L_{vi})(\Delta L'_{vi}) = \sum_i (\Delta L'_{vi})^2 \tag{29}$$

If these constraints are not used, slope and intercept may vary appreciably from 1 and 0. This unphysical result is a necessary consequence of random measurement error in sky brightness temperatures and in radiosonde-measured path delays: Scatter in the residuals of Eq. (26) will be minimized by values of b_1 and b_2 which are too small, offset by a value of b_0 which is too large. Figures 4A and 4B illustrate fits obtained with and without constraints on slope and intercept. The coefficients of Fig. 4B will predict too much water vapor path delay under dry conditions and too little under wet conditions.

[3]One may show that only the constraint on slope is actually required. In practice it is easier to constrain both slope and intercept.

Lagrange multipliers may be used to minimize Eq. (26) with respect to b_0, b_1, b_2, but subject to the constraints of Eqs. (27), (28), (29). The problem is thereby simplified to a set of six linear equations in six unknowns. The regression may also be carried out without actual measurement of sky brightness temperatures. Linearized brightness temperatures can be calculated from Eq. (3) using the water vapor absorption coefficient of Waters (Ref. 2) or Westwater (Ref. 7) and the oxygen absorption coefficient of Westwater (Ref. 7).[4] As before, one uses a representative sample of radiosonde profiles.

There is sufficient uncertainty in the water vapor absorption coefficient to cast some doubt on the accuracy of results obtained by the theoretical method. Nevertheless, we have found that the theoretical method gives coefficients in fairly good agreement with those obtained by regression against measured brightness temperatures.

VIII. Summary

A systematic method for reducing dual-frequency water vapor radiometer data to water vapor path delay has been developed. Linearized sky brightness temperatures and path delay coefficients are computed in separate procedures and then combined to calculate path delay. Sky brightness temperatures may be measured by using either tipping curves directly or by using nominal hot load corrections based on tipping curves. Coefficients may be derived from brightness temperature data using a constrained regression analysis against radiosonde-measured path delays, or from a constrained regression analysis of theoretically calculated sky brightness temperatures against radiosonde measured path delays. The coefficients are functions of surface temperature, pressure, and water vapor density, to allow use of the data reduction algorithm at any altitude and in any climate.

[4]Three corrections should be made to Westwater's oxygen absorption coefficient. The pressure should be partial pressure of dry air only, except in the line width where it is total pressure. The coefficient of the line width should be changed to 0.025 from 0.049. The power law temperature dependence of the line width should be changed to 0.85 from 0.75 (Westwater, E. R., private communication).

Acknowledgements

We thank our colleagues, Joe Waters, Joe Stacey, and Bruce Gary, for valuable discussions regarding radiometer data reduction. Bruce Gary has been especially generous with his time and unpublished calculations made for a parallel program of atmospheric remote sensing. He suggested inclusion of temperature and pressure dependence in the inversion coefficients and brought our attention to the inaccuracy of coefficients derived by a simple least squares fit.

References

1. MacDoran, P. F., "Radio Interferometry for International Study of the Earthquake Mechanism," *Acta Astronautica*, Vol. 1, pp. 1427-1444, 1974.

2. Waters, J. W., "Absorption and Emission by Atmospheric Gases," in *Methods of Experimental Physics*, Vol. 12. New York: Academic Press, Chapter 2.3, 1976.

3. Wu, S. C., "Frequency Selection and Calibration of a Water Vapor Radiometer," *DSN Progress Report 42-43*, Jet Propulsion Laboratory, Pasadena, CA, pp. 67-81, Feb. 15, 1978.

4. Gunn, K. L., and East, T. W., "The Microwave Properties of Precipitation Particles," *Quart. J. Roy. Meterol. Soc.*, Vol. 80, pp. 522-545, 1954.

5. Klein, L. A., and Smith, C. T., "An Improved Model for the Dielectric Constant of Sea Water at Microwave Frequencies," *IEEE Trans. Anten. Prop.*, Vol. AP-25, pp. 104-111, Jan. 1977.

6. Crane, R. K., "Microwave Scattering Parameters for New England Rain," Lincoln Laboratory Technical Report 426, Lexington, MA, pp. 55-57, Oct. 1966.

7. Westwater, E. R., "An Analysis of the Correction of Range Errors Due to Atmospheric Refraction by Microwave Radiometric Techniques," U.S. Department of Commerce/ ESSA Tech. Report, IER 30-ITSA 30, Boulder, CO, Mar. 1967.

8. Thayer, G. D., "An Improved Equation for the Radio Refractive Index of Air," *Radio Science*, Vol. 9, pp. 803-807, 1974.

9. Smith, E. K., and Weintraub, S., "The Constants in the Equation for Atmospheric Refractive Index at Radio Frequencies," *Proc. IRE*, Vol. 41, pp. 1035-1037, 1953.

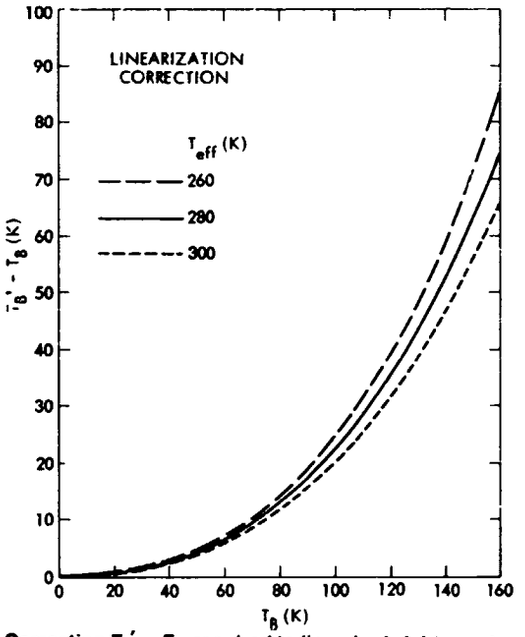

Fig. 1. Correction $T_B' - T_B$ required to linearize brightness temperatures T_B for three effective temperatures T_{eff}

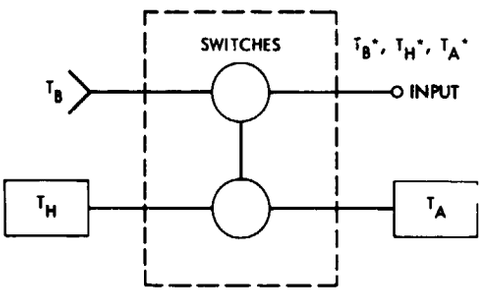

Fig. 2. Signal paths in a typical radiometer

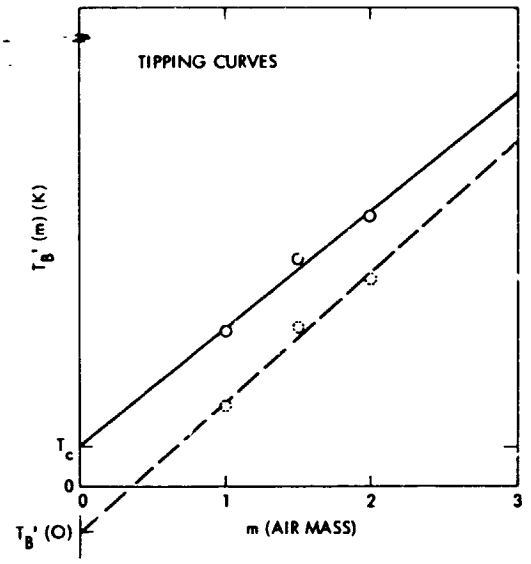

Fig. 3. Tipping curves with no hot load correction (dashed line) and with hot load correction required to give desired zero air mass intercept T_c (solid line); hypothetical data points for each case are also shown

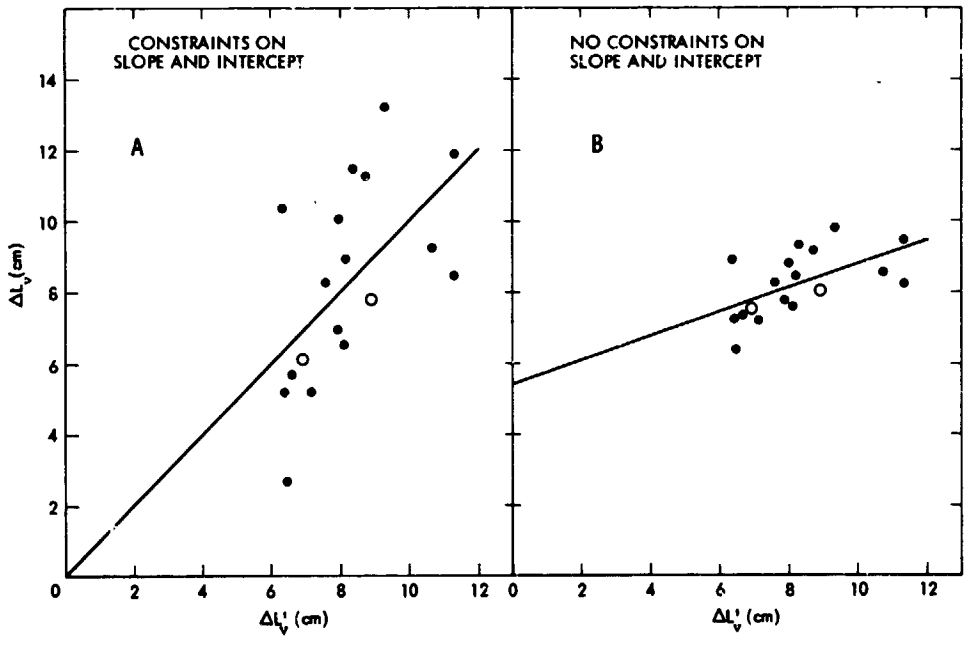

Fig. 4. Path delay ΔL_v from radiometer measurements vs path delay $\Delta L_v'$ from radiosondes using regression: (A) with constraints on slope and intercept, (B) without constraints on slope and intercept. A circle is used to indicate two overlapping points; the straight lines are least squares fits to the points generated by each regression

Low-Noise Receivers: S-Band Parametric Upconverter Development

S. Petty, D. Neff, and D. Norris
Radio Frequency and Microwave Subsystems Section

The combination of a cryogenically-cooled parametric upconverter and a higher frequency maser post amplifier has been proposed as a method of achieving maser-like receiver noise temperatures over much larger instantaneous bandwidths and tuning ranges than are presently obtainable with masers in the range of 1 to 18 GHz. An experimental 2.0- to 2.5-GHz parametric upconverter/maser system has been developed to explore these possibilities. Initial tests of this system have resulted in an effective input noise temperature of 3.1 K at 2295 MHz and 3.2 K at 2388 MHz. The parametric upconverter has logged over 1500 hours at 4.5 K and has undergone 5 thermal cycles (300 K to 4.5 K to 300 K) without degradation.

I. Introduction

Recent advances in many areas of technology have made possible the development of an ultralow-noise receiving system that can exhibit noise temperatures similar to those of microwave maser amplifiers, while providing instantaneous bandwidths and tuning ranges many times greater than those of present maser amplifiers in the 1- to 18-GHz range. This system is comprised of a cryogenically-cooled, upper-sideband parametric upconverter (Ref. 1) followed by a maser amplifier operating at a much higher frequency where wide bandwidth and large tuning ranges have been achieved. Two recent developments in particular have made these performance levels possible: the first is the availability of very high-quality gallium arsenide varactor diodes with low package parasitic reactances, and the second is the recent development of a wideband microwave maser amplifier (Ref. 2), which tunes over the range of 19 to 26 GHz.

To evaluate the feasibility of this type of system for future use in the DSN, an S-band-to-K-band cryogenically cooled parametric upconverter[1] and a K-band maser have been developed, assembled, and tested at JPL. A block diagram of the experimental system is shown in Fig. 1, and a photograph of the completed package is shown in Fig. 2. Following sections of this report will describe each of the system compo-

[1]The parametric upconverter described in this report was developed by AIL, a division of Cutler-Hammer, Melville, L.I., N.Y., under contract to JPL.

nents, provide a theoretical noise temperature analysis, and present performance measurements obtained to date.

II. S-Band Parametric Upconverter

The S-band-to-K-band parametric upconverter (Ref. 3), shown in Fig. 3, has a coaxial signal input circuit and a varactor mount, pump circuit, and (sum) output circuit in K-band waveguide. The input circuit consists of a Type N input connector, a bias tee, which provides diode bias voltage via the input coaxial center conductor, and a matching and tuning section. The varactor diode mount contains a pair of matched diodes mounted across a K-band waveguide in a balanced configuration. This configuration isolates the input circuit from pump, output, and image frequency components, therefore eliminating the need for input circuit filtering with the attendant insertion loss. Separation of pump and output frequency components is accomplished by two bandpass filters. Waveguide spacers and reduced-height sections (not labeled in Fig. 3) provide impedance transformation and tuning at the output, pump, and image frequencies.

The upconverter measures 8 dB of net gain with a 3-dB instantaneous bandwidth of approximately 500 MHz when operating at a physical temperature of 4.5 K. Input return loss measures −7 dB or better from 1950 to 2450 MHz, with the region of best input match (return loss $\geq$ − 10 dB) between 2250 and 2420 MHz. Note that these parameters, which vary considerably with bias current level, were measured at a varactor bias current of 1 to 2 μA. Subsequent noise temperature measurements (described in Section VI of this article) have demonstrated that the best midband noise performance occurs with zero bias current. Therefore, gain, bandwidth, and other RF parameters must be examined after optimum bias settings (for best noise performance) have been determined.

The maser pump rejection filter (Fig. 1) located at the output port of the upconverter is necessary to prevent maser pump power leakage from combining with upconverter pump power in the varactor diodes to produce spurious in-band interfering signals. The present filter is of the "waffle-iron" type and exhibits sufficient attenuation at the maser pump frequency (and its harmonics) to permit noise temperature measurements. An operational upconverter/maser system for the DSN (where received signal levels can be as low as −180 dBm) would require an interstage filter with much higher attenuation at these frequencies.

III. K-Band Reflected Wave Maser (Post Amplifier)

The K-band reflected wave maser is a four-stage, ruby-filled waveguide traveling wave structure operating at 4.5 K (Figs. 4 and 6). A circulator is used to direct input signals into each ruby-filled waveguide section where maser amplification occurs; on reaching the end of the filled waveguide section, the signal is reflected back to the input and is amplified a second time before passing through the input circulator and onto the next stage. Additional circulators (Fig. 5) are used to increase interstage isolation. The three sections shown in Fig. 4 are combined into the single assembly shown in Fig. 6 with the superconducting magnet required for maser operation at the left.

When the maser is tuned to the upconverter output frequency, the maser pump frequency is modulated to cover a 1-GHz range centered near 51 GHz. Pump power (75 to 100 mW) is supplied with a Siemens Corp. model number RW060 backward wave oscillator. Overall maser gain is 30 to 40 dB with 60 to 250 MHz of instantaneous bandwidth depending on the frequency of operation. The limited instantaneous bandwidth available at present is due to magnetic field nonlinearities in the superconducting magnet. This condition does not affect the validity of upconverter/maser system noise temperature measurements, but it does require that the maser be tuned to the specific frequency of interest within the upconverter bandwidth so that maser gain and effective input noise temperature (4.7 ± 0.5 K) are maintained.

This particular maser is a copy of the K-band reflected-wave maser developed by JPL and NRAO[2]; a complete technical description of which is soon to be published (Ref. 2). Continuing K-band maser development work by NRAO has produced a 500-MHz bandwidth. This improvement was accomplished by using a larger superconducting magnet with the same maser structure as described here (Ref. 4). Initial development work on the reflected-wave maser concept began in 1972 under a California Institute of Technology President's grant to the University of California at San Diego and the Jet Propulsion Laboratory (Ref. 5).

IV. Closed-Cycle Refrigerator

A standard 1-W JPL 4.5-K closed-cycle refrigerator (CCR) (Refs. 6, 7) is used to house the upconverter/maser assembly. Figure 2 shows the packaged system with attached pump sources. Figure 7 shows the CCR with vacuum housing, input transmission line, and radiation shields removed.

[2]The development of this maser design was the result of a joint research effort between the National Radio Astronomy Observatory, operated by Associated Universities, Inc., under contract with the National Science Foundation, and the JPL/CIT under contract NAS7-100 sponsored by NASA.

The S-band input transmission line (Fig. 8) utilizes an existing waveguide-to-coax design (Ref. 8) that cools the entire length of coaxial center conductor to 4.5 K. The noise temperature contribution from this transmission line is calculated to be 0.5 K. A length of 3.5-mm (0.141-inch) O.D. semirigid cable, all at a 4.5-K physical temperature, couples the input signal from the CCR input transmission line to the upconverter input connector. Two liquid-helium heat exchangers are required to properly maintain the upconverter diode mount, superconducting magnet, maser circulator assembly, maser structure, and related interconnecting waveguide components at 4.5 K.

Pump inputs in WR 42 and WR 19 waveguide (Figs. 2, 7) are used for exitation of the parametric upconverter (21.76 GHz) and the maser ruby structure (51 GHz), respectively. A WR 42 waveguide is used for the maser output at 24 GHz. Other inputs to the 4.5 K station include the magnet charging system and normal instrumentation wires.

New, larger heat shields were required because of the increased size of the 4.5 K assembly. The increased thermal radiation load from this source, combined with the total input pump power (120 to 150 mW) and the heat conduction associated with the many input connections to the 4.5 K station, have severely loaded the 1-W capacity of the CCR. Operation in a 35°C ambient environment and rapidly repeated retuning of the superconducting magnet have resulted in several CCR warmups. The system, while functional for testing, is very marginal. The development of CCRs with greater 4.5 K cooling capacity is planned.

The large mass (≈9 kg) attached to the 4.5-K station required changes in the support structure and precool system. Mechanically, the upconverter/maser assembly and 4.5-K station are supported by the input waveguides and a solid copper block connected to the 15-K station via the hydrogen thermal switch (Fig. 7). A larger nitrogen precool heat exchanger and copper sheath were attached directly to the superconducting magnet assembly since heat transfer through the Hyperco 27 magnet material is low. Additional copper straps are used to aid heat transfer. These changes have reduced the precool time (ambient to 80 K) from three hours to one hour; a total of eight hours is required to cool down to 4.5 K. The 15-K station appears to have additional cooling capacity to decrease the cooldown time; a larger capacity hydrogen thermal switch should be developed to improve heat transfer from the 4.5-K station to the 15-K station during the cooldown process. A new digital thermometer[3] is being used to monitor CCR temperatures replacing the traditional thermocouple sensors. The direct readout feature from 2 to 300 K enables more convenient and more accurate measurements than has previously been achieved with thermocouple instrumentation.

[3]Model DRC-70C, Digital Thermometer/Controller manufactured by Lakeshore Cryotronics, Inc., Columbus, Ohio.

V. Theoretical Noise Temperature Estimate

Table 1 itemizes the calculated *contribution* to the effective input noise temperature (at the room temperature waveguide input flange) of each component in the upconverter/maser system as diagrammed on the left side of the table. These calculations do not include the effect of input or output circuit mismatch. Therefore, the results are applicable only to midband frequencies where upconverter gain is maximum and input and output reflection losses are small. At 2295 MHz, upconverter gain is within 1 dB of maximum and input return loss between −10 and −13 dB (depending on bias setting), and it is valid to compare noise temperature measurements obtained at this frequency with the theoretical values in Table 1.

As indicated in the table notes, the parameter values used in the calculation are best estimates based on handbook values, previously measured data on similar parts, or data from the various references. Upconverter input and output losses L_3 and L_4 are estimated from (1) measurements reported in Ref. 3, and (2) the difference between theoretical gain (assuming no circuit losses but including calculated diode losses) and actual measured gain.

The physical temperature of the diode junctions has a substantial effect on the overall system effective noise temperature according to Table 1: 2.5 K if the diode junctions experience no pump heating, and 3.5 K if the diode junctions are heated to 20 K. The uncertainties in the estimates of the various contributions listed in Table 1 have not been rigorously analyzed. However, it is believed that the sum of the worst case errors for all other contributions does not exceed the ±0.5 K resulting from the two different diode junction temperature assumptions discussed above. Workers in the field have estimated this pump heating effect to be anywhere between 0.5 K and 30 K above the ambient temperature. Careful system noise temperature measurements as a function of bias level and upconverter pump power level may shed some light on this important question of pump diode heating.

Upconverter diode gain G_D (see Table 1, note f) is approximately proportional to the ratio of output frequency to input frequency. For the S-band to K-band upconverter, this ratio is high, and therefore noise contributions from upconverter

output circuit losses, interstage losses, and maser input noise temperature are small. For this reason, the system input noise temperature is, in fact, lower than the 4.7-K maser input noise temperature. Consider similar varactor diodes used in a 8.5-GHz to 24-GHz upconverter. G_D for this case would be approximately 3 dB and system input noise contributions from L_4, L_5, and T_M would be substantially larger. If maximum performance is to be obtained from upconverter/maser systems at X-band or K_u-band, careful effort will be needed to minimize the loss of each component in the system, and the benefits of using a higher frequency maser postamplifier should be explored.

VI. Noise Temperature Measurements

Noise temperature measurements of the upconverter-maser system were performed at JPL. A feed horn was attached to the input waveguide flange and a large piece of microwave absorber was used as an ambient temperature termination for the horn (see Fig. 9). System noise temperature data are obtained by covering the feed horn with the absorber and then removing the absorber, allowing the horn to view the cold sky. Total operating system noise temperature is obtained by making precision power-level measurements with and without the absorber in place. A detailed description and analysis of noise temperature calibrations using ambient terminations has been published by C. T. Stelzried. (Ref. 10)

Initial measurements to date have resulted in a total system operating noise temperature of 9.4 K at 2295 MHz and 9.5 K at 2388 MHz. Best estimates of noise contributions for the parts of the system are given in Table 2. The noise contribution estimates for the sky and horn are those used in previous S-band maser noise calibrations (Ref. 8). The follow-up receiver contribution is measured by making a system power measurement with the maser pump source on and off. When these three contributions are subtracted from the total system noise temperature, the effective input noise temperature for the upconverter/maser system is found to be 3.1 K at 2295 MHz and 3.2 K at 2388 MHz. These values fall within the theoretical estimate of 2.5 to 3.5 K obtained in Table 1.

The upconverter noise temperature can be estimated by subtracting component noise contribution estimates (Table 1) from the system effective input noise temperatures reported above. This calculation results in an input noise temperature for the upconverter of less than 2 K.

VII. Reliability

The ability of the parametric upconverter to withstand repeated temperature cycling from room temperature to 4.5 K and to operate reliably at this temperature for extended periods of time is of importance. If a cryogenic component is to become an operational reality in the DSN, it must demonstrate high performance in the above areas as well as in areas of RF performance. To date, the upconverter itself has logged over 1500 hours at 4.5 K and has undergone 5 full temperature cycles of 300 K – 4.5 K – 300 K without degradation.

VIII. Conclusions

The combination of an experimental cryogenically-cooled S-band upconverter and a K-band maser postamplifier has demonstrated an effective input noise temperature of 3.1 K at 2295 MHz and 3.2 K at 2388 MHz. These initial results compare favorably with input noise temperatures of 2.0 to 2.1 K achieved with the best S-band maser amplifiers (Ref. 8). These figures represent a remarkable achievement in noise performance for a system which has a potential instantaneous bandwidth of 400 to 500 MHz at S-band frequencies.

Testing of this system will be continued. Feed horn configurations that are suitable for other frequencies within the 2.0 to 2.5-GHz range will be obtained so that system noise temperature can be evaluated across the entire upconverter bandwidth. Other RF parameters will be investigated and reliability in the cryogenic environment will be monitored.

References

1. Sard, E., Peyton, B., Okwit, S., "A Positive Resistance Up-Converter for Ultra-Low-Noise Amplification," *IEEE Transactions on Microwave Theory and Techniques*, Vol. MTT-14, No. 12, December 1966, pp. 608-618.

2. Moore, C. R., and Clauss, R. C., "A Reflected-Wave Ruby Maser With K-Band Tuning Range and Large Instantaneous Bandwidth," to be published by *IEEE Transactions on Microwave Theory and Techniques.*

3. Irvin, G., and Kopcsay, G. V., *Parametric Upconverter*, Final Report on JPL Contract JS651115, AIL, a division of Cutler-Hammer, Melville, L.I., N.Y., January 1977.

4. Moore, C. R., National Radio Astronomy Observatory, P.O. Box 2, Greenbank, West Virginia. Private communication, Sept. 1977.

5. Larry D. Flesner, Sheldon Schultz, Robert Clauss, "Simple Waveguide Reflection Maser With Broad Tunability," *Review of Scientific Instruments*, Vol. 48. No. 8, August 1977, pp. 1104-1105.

6. W. H. Higa and E. Wiebe, "A Simplified Approach to Heat Exchanger Construction to Cryogenic Refrigerators," *Cryogenic Technology*, Vol. 3, pp. 47-48, 50-51, March/April 1967.

7. W. H. Higa and E. Wiebe, "One Million Hours at 4.5 Kelvin," presented at the Cryocooler Applications Conference, sponsored by National Bureau of Standards, Boulder, Colorado, October 1977.

8. Clauss, R. C., and Wiebe, E. R., "Low-Noise Receivers: Microwave Maser Development," in *The Deep Space Network Progress Report*, Technical Report 32-1526, Vol. XIX, pp. 93-99, Jet Propulsion Laboratory, Pasadena, Calif., Feb. 15, 1974.

9. Penfield, Paul, Jr., and Rafuse, Robert P., *Varactor Applications*, M.I.T. Press, Cambridge, Mass., 1962, p. 116.

10. Stelzried, C. T., "Operating Noise Temperature Calibrations of Low-Noise Receiving Systems," *Microwave Journal*, Vol. 14, No. 6, June 1971, pp. 41-48.

Table 1. Theoretical noise temperature estimate, f_s = 2.3 GHz

System schematic diagram	Component description	Component loss L, or gain G, or input noise temperature T	Value of L, G, or T	Component contribution to effective input noise temperature at S-band waveguide input port	
				Contribution[a,b]	Value
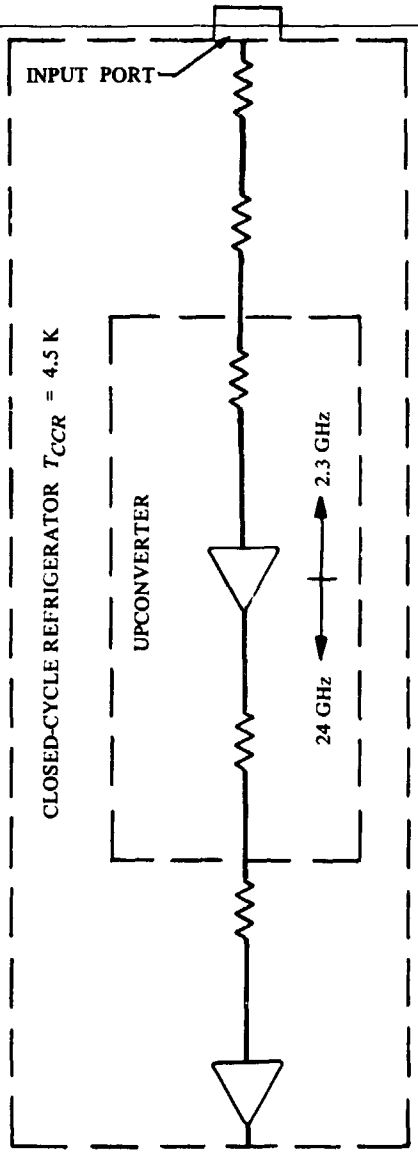	S-band input transmission line	L_1	0.05 dB[c]	–[c]	0.5 K[c]
	0.141 semirigid cable	L_2	0.03 dB[d]	$L_1 (L_2 - 1) T_{CCR}$	0.03 K
	Upconverter input circuit loss	L_3	0.4 dB[e]	$L_1 L_2 (L_3 - 1) T_{CCR}$	0.44 K
	Varactor diodes	G_D T_D	G_D = 9 dB[f] T_D = 0.3 K[g,h] T_D = 1.2 K[h,i]	$L_1 L_2 L_3 T_D$	0.3 K[g] 1.3 K[i]
	Upconverter output circuit loss	L_4	0.6 dB[e]	$\frac{L_1 L_2 L_3 (L_4 - 1)}{G_D} T_{CCR}$	0.09 K
	Interstage loss, including pump rejection filter	L_5	0.9 dB[d]	$\frac{L_1 L_2 L_3 L_4 (L_5 - 1)}{G_D} T_{CCR}$	0.17 K
	Maser	T_M	4.7 K[j]	$\frac{L_1 L_2 L_3 L_4 L_5}{G_D} T_M$	0.93 K
				Total system effective input noise temperature	2.5 K[g] 3.5 K[i]

Table 1. Theoretical noise temperature estimate, f_s = 2.3 GHz (contd)

[a]CCR physical temperature T_{CCR} = 4.5 K.

[b]In the equations, losses L and gains G are dimensionless ratios.

[c]Temperature along this line varies from 300 K to 4.5 K. Q measurements, insertion loss, and temperature gradient calculations were used to determine 0.5 K contribution.

[d]Estimated from published values, previous measurements of similar components, and measured variations of insertion loss vs temperature.

[e]See Section V.

[f]For minimum noise tuning:

$$G_D \approx \frac{f_o}{f_s} \frac{1}{1+\frac{f_o}{M}} \quad \text{(Ref. 10)}$$

where

G_D = conversion gain of varactor diodes

M = varactor diode figure of merit $m_1 f_c$

= 80 GHz (Ref. 3)

f_o = output frequency

= 24 GHz

f_s = input frequency

= 2.3 GHz

Substituting:

G_D = 8.0 = 9 dB

[g]If diode junction temperature is 4.5 K, i.e., no pump heating.

[h]For minimum noise tuning:

$$T_D \cong \frac{2f_s}{M} T_J \quad \text{(Ref. 10)}$$

$\approx$ 0.3 K for T_J = 4.5 K

$\approx$ 1.3 K for T_J = 20 K

where

T_D = effective input noise temperature of varactor diodes due to series resistance.

T_J = physical temperature of diode junction.

[i]If diode junction temperature is 20 K.

[j]Calculation of maser effective input noise temperature gives T_M = 4.7 K ± 0.5 K (Ref. 2)

Table 2. Noise contributions for the upconverter/maser system

Part of system	Noise contribution, K	
	2295 MHz	2388 MHz
Sky (includes atmosphere and cosmic background)	4.9	4.9
Horn (includes mode generator and transition)	1.2	1.2
Upconverter/Maser System	3.1	3.2
Follow-up receiver	0.2	0.2
Total operating system noise temperature T_{op}	9.4	9.5

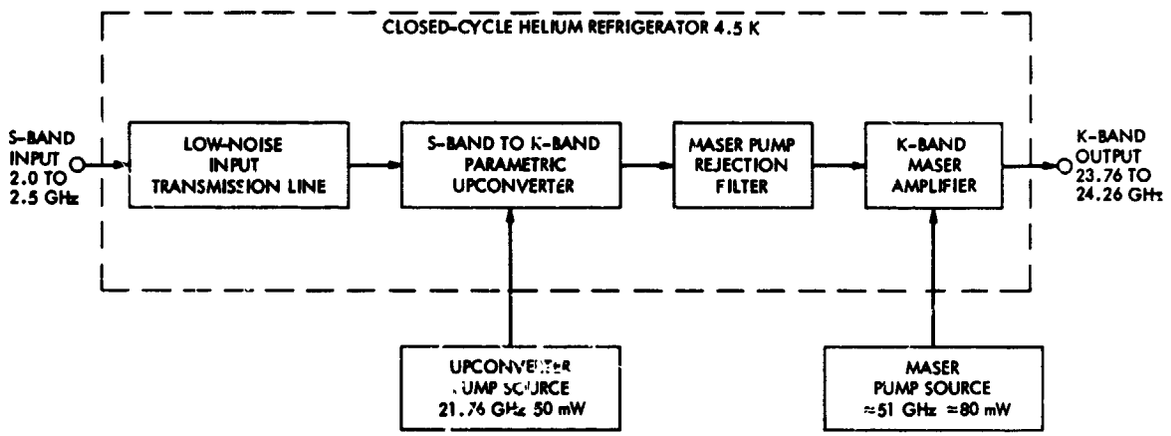

Fig. 1. Block diagram of upconverter/maser/CCR system

Fig. 2. Packaged upconverter/maser/CCR system

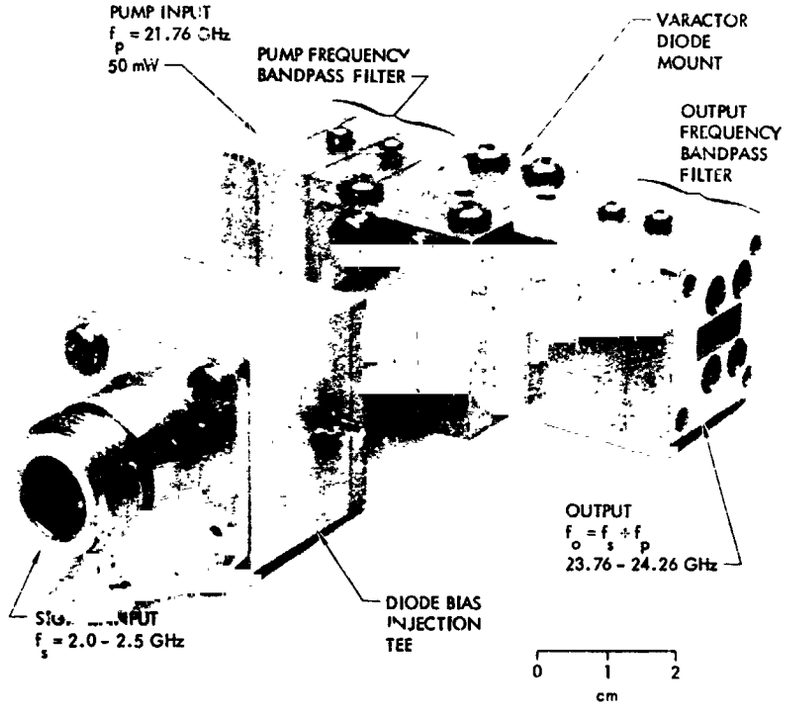

Fig. 3. S-band parametric upconverter

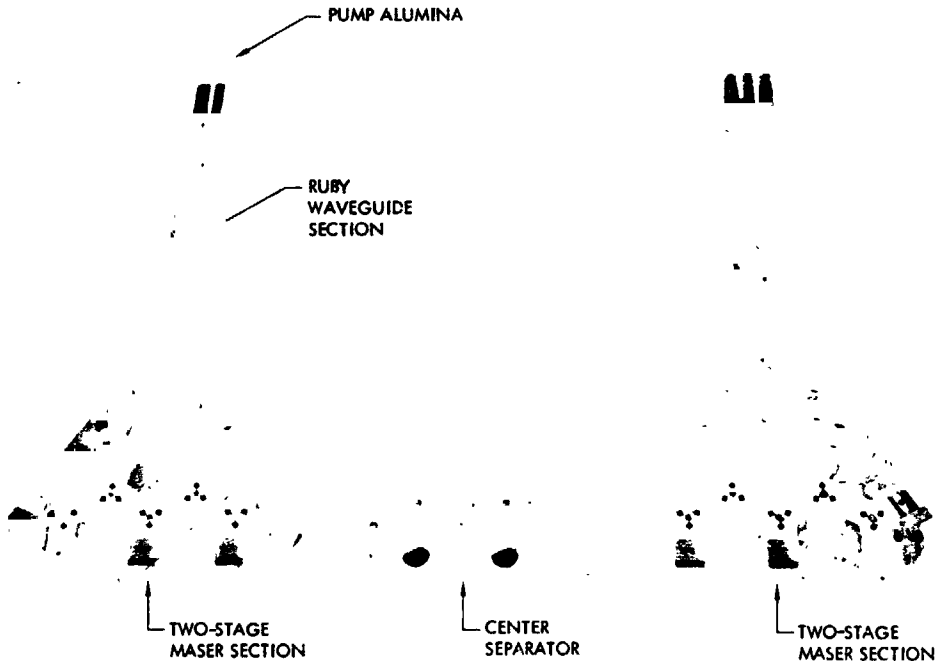

Fig. 4. K-band maser structure

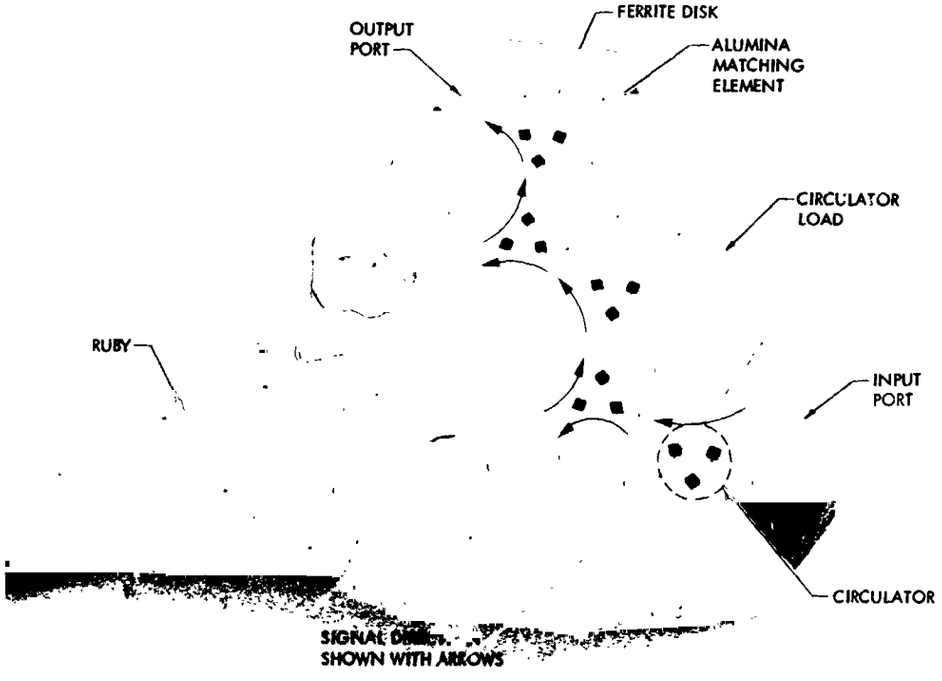

Fig. 5. K-band maser circulator and ruby waveguide detail

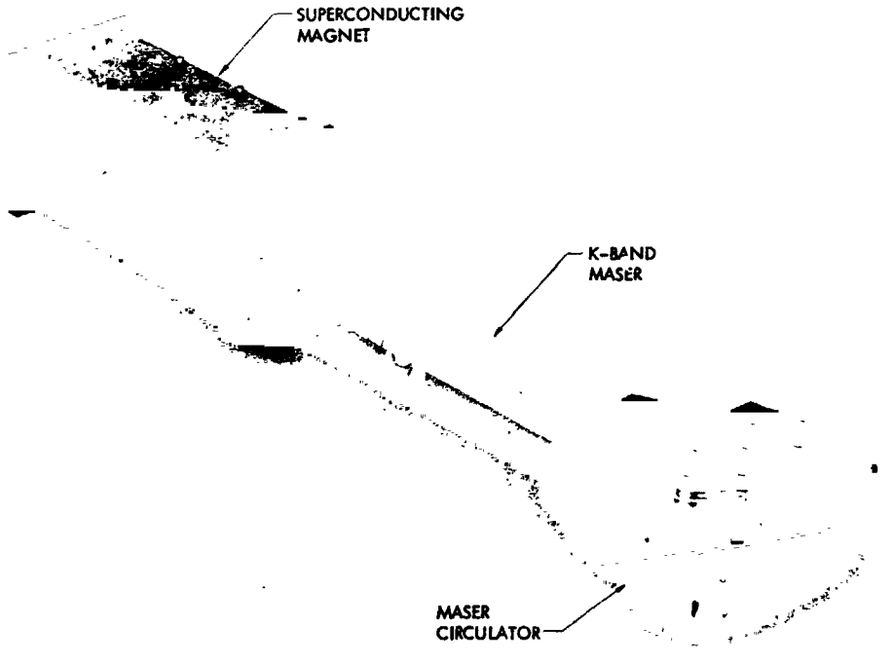

Fig. 6. K-band maser with superconducting magnet

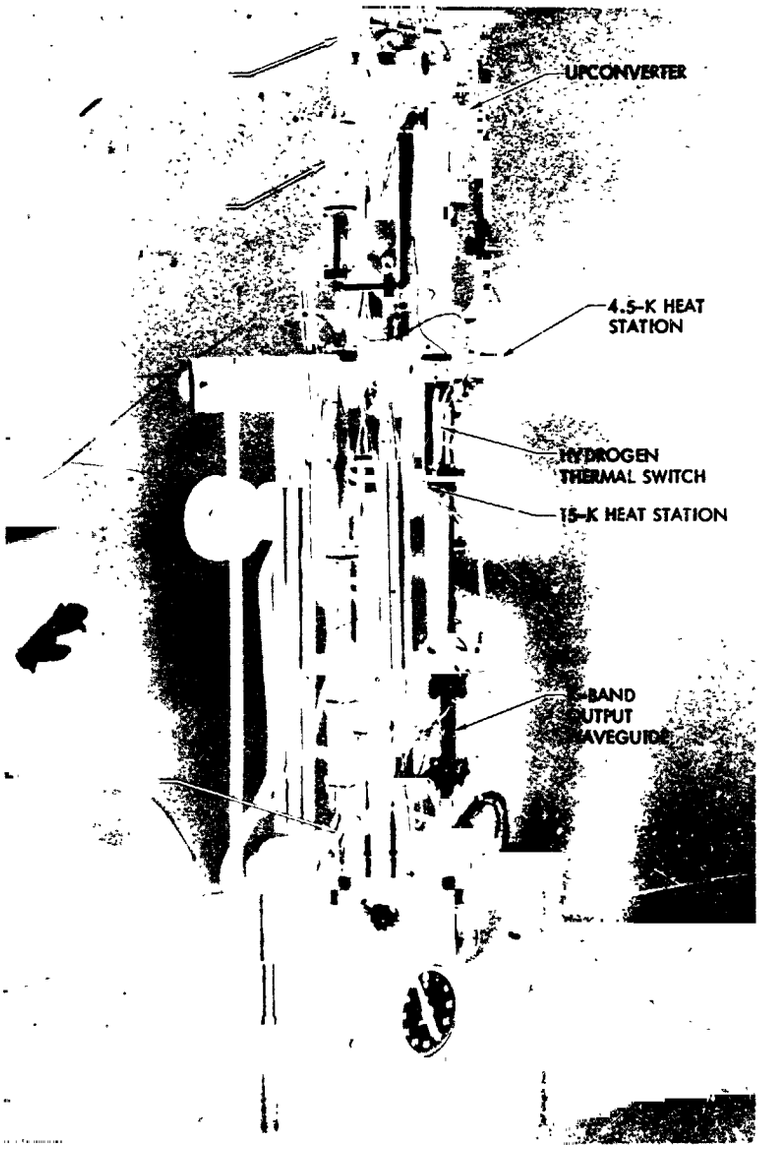

Fig. 7. CCR assembly

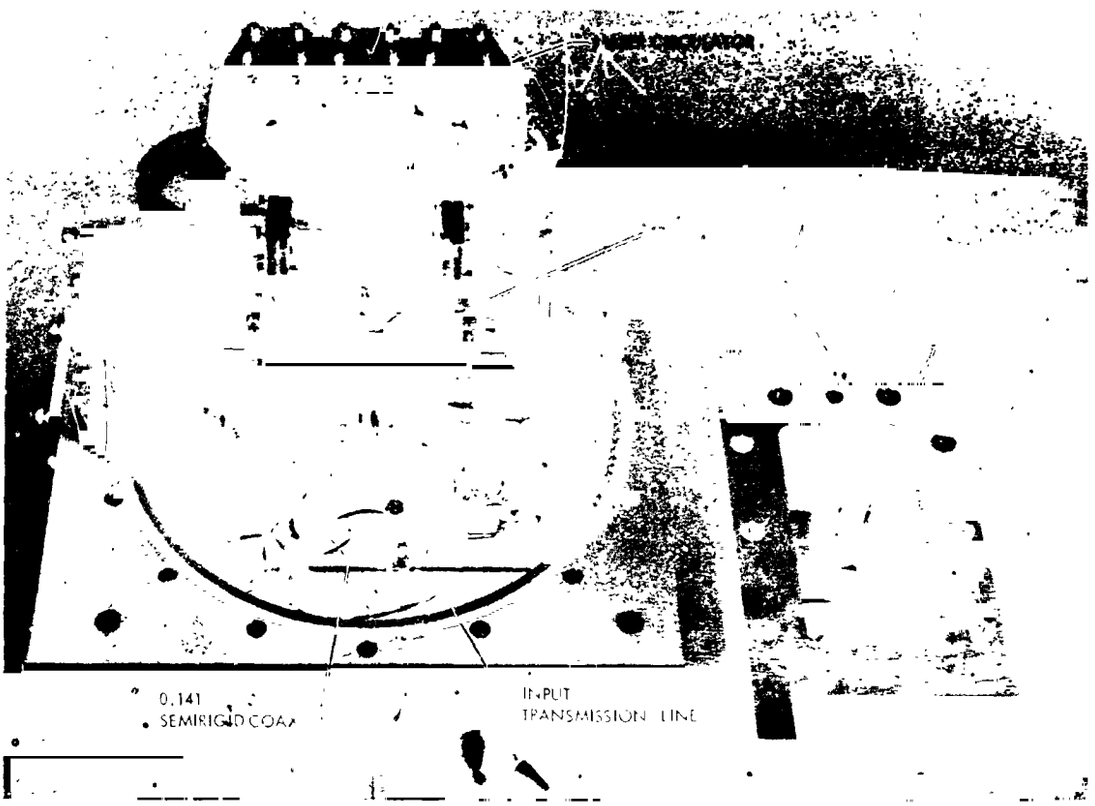

Fig. 8. CCR partially disassembled, showing input transmission line and 4.5-K components

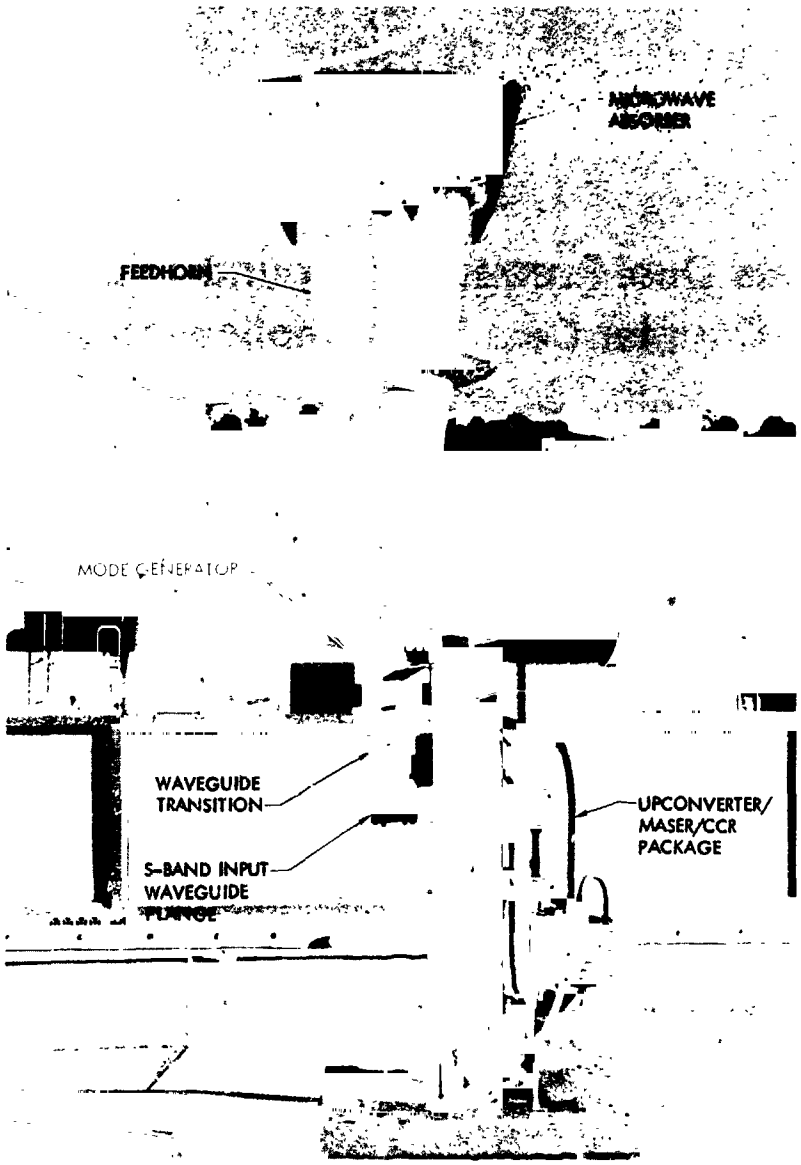

Fig. 9. System for measurement of upconverter/maser noise temperature

Dq

N79-16009

Simultaneous Dual-Frequency, Round-Trip Calibration of Doppler Data With Application to Radio Science Experiments

A. L. Berman
TDA Engineering Office

Simultaneous dual-frequency, round-trip (uplink and downlink) calibration of Doppler data is expected to be a requirement of several radio science experiments being planned for the next decade, and such (calibration) capability is expected to be achieved by the mid-1980s. Simultaneous dual-frequency, round-trip calibration would be straightforward except for the condition of unequal spacecraft turnaround ratios at S- and X-band. This article discusses the impact of unequal turnaround ratios on calibration accuracies in the specific cases of the Gravitational Wave Detection Experiment and the Solar Gravitational Quadrupole Moment Experiment.

I. Introduction

By the early to mid-1980s, the Deep Space Network (DSN) is expected to have augmented the current S-band uplink capability with X-band uplink capability. With additional modification to the spacecraft and ground tracking system, one can readily foresee the provision of the capability for simultaneous round-trip (uplink and downlink) transmission of S- and X-band frequencies. Simultaneous (and independent) transmission of S- and X-band frequency provides the important capability of high-precision calibration of charged particle effects on radio metric (i.e., Doppler and range) data. This new capability will be crucial to certain radio science experiments, and may additionally prove to be beneficial in regard to navigational usage of radio metric data. Such round-trip, dual-frequency calibrations would be (close to) exact and trivial to apply, except for the fact that the spacecraft turnaround ratios[1] at S- and X-band are, according to the current design, expected to be (slightly) unequal.

Simultaneous dual-frequency[2] calibration of radio metric data is expected to be important to the following radio science experiments:

Radio science experiment	Sun-Earth-probe angle, deg	Radio metric data type of interest
Gravitational Wave Detection	~ 180	Doppler
Relativity Tests	~ 0	Range
Solar Quadrupole Measurement	~ 0	Doppler

Callahan (Ref. 1) has treated simultaneous dual-frequency calibration of range data. Although the mechanics of the calibration are similar for both the Doppler and range applica-

[1] Ratio of spacecraft transmitted frequency to spacecraft received frequency for a single-frequency band.

[2] "Simultaneous dual-frequency" will specifically imply "simultaneous, independent, round-trip, dual-frequency."

tions, the final efficacy of the calibration in any given application is highly dependent upon the particular circumstances of the application.

This article will derive and discuss simultaneous dual-frequency calibration of Doppler data. Specifically emphasized will be the application of simultaneous dual-frequency calibration of Doppler data in regard to the Gravitational Wave Detection Experiment (Ref. 2) and the Solar Quadrupole Moment Experiment (Ref. 3).

II. Simultaneous Dual-Frequency, Round-Trip Calibration of Doppler Data

It was noted in Section I that the main difficulty with simultaneous dual-frequency calibration capability is that the spacecraft turnaround ratios at S- and X-band are expected to be (slightly) unequal. Figure 1 presents a simplified block diagram of dual-frequency transmission; the relevant parameters are defined as follows:

F_0 = S-band uplink frequency
$\simeq$ 2.115 GHz

K_0 = ratio of uplink X-band to uplink S-band
$\simeq$ 3.404

C_0 = S-band spacecraft turnaround ratio
$\simeq$ 1.086

C_1 = X-band spacecraft turnaround ratio
$\simeq$ 1.169

One now makes the following additional definitions (where $\Delta\phi$ relates to columnar electron (number) density fluctuation):

Uplink charged particle fluctuation effect (in cycles)

$$= \Delta\phi_{up}\left(\frac{F_0 C_0}{f}\right)$$

Downlink charged particle fluctuation effect (in cycles)

$$= \Delta\phi_{dn}\left(\frac{F_0 C_0}{f}\right)$$

f = frequency

To isolate the frequency-dependent effects (i.e., charged particle fluctuation effects), one scales the downlink X-band by the downlink S-X ratio (C_0/C_1K_0) and differences this with the downlink S-band. The quantity being operated on is integrated (counted) Doppler frequency during a given (averaging time) interval:

$\Delta\phi_m \equiv$ measured charged particle fluctuation effect, in cycles (at S-band downlink frequency)

$$= \left[F_s - \left(\frac{C_0}{C_1 K_0}\right) F_x\right]$$

where:

F_s = (integrated) S-band downlink frequency

F_x = (integrated) X-band downlink frequency

In terms of $\Delta\phi_{up}$ and $\Delta\phi_{dn}$, one expects for the measured charged particle fluctuation effect:

$$\Delta\phi_m = \left[\Delta\phi_{up}\left(\frac{F_0 C_0}{F_0}\right)\cdot C_0 + \Delta\phi_{dn}\left(\frac{F_0 C_0}{F_0 C_0}\right)\right]$$

$$- \left(\frac{C_0}{C_1 K_0}\right)\cdot\left[\Delta\phi_{up}\left(\frac{F_0 C_0}{K_0 F_0}\right)\cdot C_1\right.$$

$$\left. + \Delta\phi_{dn}\left(\frac{F_0 C_0}{C_1 K_0 F_0}\right)\right]$$

$$= \Delta\phi_{up}\, C_0^2\left[1 - \frac{1}{K_0^2}\right] + \Delta\phi_{dn}\left[1 - \frac{C_0^2}{C_1^2 K_0^2}\right]$$

By defining the difference between uplink and downlink charged particle fluctuation effect:

$$\epsilon \equiv \Delta\phi_{up} - \Delta\phi_{dn}$$

one obtains the downlink charged particle fluctuation effect in terms of the measured charged particle fluctuation effect and the uplink-downlink difference:

$$\Delta\phi_{dn} = \frac{\Delta\phi_m - \epsilon C_0^2\left(1 - \frac{1}{K_0^2}\right)}{\left[C_0^2\left(1 - \frac{1}{K_0^2}\right) + 1 - \frac{C_0^2}{C_1^2 K_0^2}\right]}$$

One now writes the expression for the measured charged particle fluctuation effect in terms of the desired (scaled) calibration (first bracketed term) and a term that is dependent on the (unknown) uplink-downlink differences (second bracketed term):

$$\Delta\phi_m = \left\{\left[1-\frac{1}{K_0^2}\right]\cdot\left(C_0^2\,\Delta\phi_{up}+\Delta\phi_{dn}\right)\right\}+\left\{\frac{1}{K_0^2}\left[1-\frac{C_0^2}{C_1^2}\right]\cdot\Delta\phi_{dn}\right\}$$

The appropriate (S-band) calibration is now identified as follows:

$$C_0^2\,\Delta\phi_{up}+\Delta\phi_{dn}=\left(1-\frac{1}{K_0^2}\right)^{-1}\left\{\Delta\phi_m-\frac{1}{K_0^2}\left[1-\frac{C_0^2}{C_1^2}\right]\cdot\Delta\phi_{dn}\right\}$$

$$=\left(1-\frac{1}{K_0^2}\right)^{-1}\left\{\Delta\phi_m-\frac{\frac{1}{K_0^2}\left(1-\frac{C_0^2}{C_1^2}\right)\left[\Delta\phi_m-\epsilon C_0^2\left(1-\frac{1}{K_0^2}\right)\right]}{\left[C_0^2\left(1-\frac{1}{K_0^2}\right)+1-\frac{C_0^2}{C_1^2K_0^2}\right]}\right\}$$

Christensen (Ref. 4) first noted that dual-frequency calibration of either frequency is (essentially) equivalent; the X-band calibration corresponding to the above (S-band) calibration is:

$$C_1^2\,\Delta\phi_{up}+\Delta\phi_{dn}=\left(1-\frac{1}{K_0^2}\right)^{-1}\left\{\Delta\phi_m-\frac{\left(\frac{C_1^2}{C_0^2}-1\right)\left[\Delta\phi_m-\epsilon C_1^2\left(1-\frac{1}{K_0^2}\right)\right]}{\left[C_1^2\left(1-\frac{1}{K_0^2}\right)-\frac{1}{K_0^2}+\frac{C_1^2}{C_0^2}\right]}\right\}$$

These expressions reduce to:

$$C_0^2\,\Delta\phi_{up}+\Delta\phi_{dn}\propto\Delta\phi_m+6.40\times10^{-3}\,\epsilon\ \text{(S-band)}$$

$$C_1^2\,\Delta\phi_{up}+\Delta\phi_{dn}\propto\Delta\phi_m+9.17\times10^{-2}\,\epsilon\ \text{(X-band)}$$

The S-band result is similar to that obtained by Callahan (Ref. 1). To utilize these relationships, one needs to be able to relate ϵ to $\Delta\phi_m$; this can only be done in the context of specific experimental conditions. Applications of these results to specific radio science experiments will be discussed in Sections III and IV to follow.

III. Gravitational Wave Detection Experiment Application

The gravitational wave detection experiment utilizing ultra-precise Doppler data has been described in detail in Ref. 2. The experiment is expected to be performed under the following conditions:

(1) SEP ~ 180 deg (specifically to reduce solar wind fluctuations).

(2) Long round-trip light times (RTLTs).

Under such conditions, most of the electron density (and density fluctuation) is near-Earth, so that the correlation time

of interest between uplink and downlink solar wind fluctuation is essentially the RTLT. The Doppler sample interval of interest will be significantly less than the RTLT (Ref. 2). Under these circumstances, one can expect little correlation between $\Delta\phi_{up}$ and $\Delta\phi_{dn}$. A reasonable and quite conservative assumption to make under such conditions is that the difference between $\Delta\phi_{up}$ and $\Delta\phi_{dn}$ is of the same order as the quantities themselves, or, very approximately:

$$\epsilon = \Delta\phi_{up} - \Delta\phi_{dn} \sim \Delta\phi_m$$

For the X-band calibration, one thus expects an error of approximately 0.1 ($\sim 9.17 \times 10^{-2}\ \epsilon/\Delta\phi_m$) when using simultaneous dual-frequency calibration with the currently expected unequal turnaround ratios. Since the quantity of interest to the gravitational wave detection experiment is fractional frequency fluctuation:

$$\sigma(\Delta F/F)$$

one expects a simple order-of-magnitude improvement over the performance for uncalibrated two-way X-band (uplink and downlink). Figures 2 and 3 update previous graphs (Ref. 5) of (with τ_a = averaging time):

$$\sigma(\Delta F/F) \text{ versus } \tau_a$$

under the assumption that simultaneous dual-frequency calibrations result in an order-of-magnitude improvement for the gravitational wave detection experiment conditions.

IV. Solar Quadrupole Moment Experiment Application

The experiment to measure the solar gravitational quadrapole moment via a spacecraft passing very close to the Sun (for instance, at four solar radii as in the proposed Solar Probe Mission) is described by Anderson, et al., in Ref. 3. In this experiment, Doppler measurements at an approximate 10-minute sample interval are the quantity of interest. Most pertinent to the consideration of simultaneous dual-frequency calibration is that the spacecraft is (essentially) *at* the closest approach distance during the time of minimum SEP (~1 deg for the Solar Probe Mission), hence the spacecraft is located at the point of maximum signal path electron density (and density fluctuation). The importance of this is that for any Doppler averaging times greater than a few seconds the $\Delta\phi_{up}$ and $\Delta\phi_{dn}$ will be extremely well correlated. Allowing the very conservative approximation (for a 10-minute averaging time):

$$\epsilon = \Delta\phi_{up} - \Delta\phi_{dn} \sim 0.1\Delta\phi_m$$

results in an error of approximately 0.01 ($\sim 9.17 \times 10^{-2}\ \epsilon/\Delta\phi_m$), hence one can expect a two orders-of-magnitude improvement via simultaneous dual-frequency calibration of X-band as compared to uncalibrated two-way X-band. From Ref. 3, the uncalibrated two-way X-band error at four solar radii is (solar wind fluctuation error only):

$$1\sigma = 2.5 \text{ mm/s}$$

and therefore, with simultaneous dual-frequency calibration of X-band, one can expect:

$$1\sigma = 2.5 \times 10^{-2} \text{ mm/s}$$

At the current time, the ground tracking system (rubidium frequency standard) has a frequency fluctuation of approximately (with τ_a = 10 minutes):

$$1\sigma \approx 1.0 \times 10^{-1} \text{ mm/s}$$

so that even with unequal spacecraft turnaround ratios, simultaneous dual-frequency calibrations appear to be able to reduce solar wind fluctuation in this experiment to below the current (system) inherent limitations.

V. Discussion and Summary

Simultaneous dual-frequency, round-trip (uplink and downlink) capability provides the crucial ability to be able to calibrate solar wind fluctuation in radio science experiments that require highly precise Doppler measurements. The calibration process is complicated by the usage (as per current design) of unequal spacecraft turnaround ratios at S- and X-band. In the case of the Gravitational Wave Detection Experiment, the unequal turnaround ratios limit the calibration to an order-of-magnitude improvement over the uncalibrated two-way (uplink and downlink) X-band; eventually this may result in solar wind fluctuation being the limiting factor in achieving increased system sensitivity. For the Solar Gravitational Quadrupole Moment Experiment, on the other hand, the unequal turnaround ratios will basically not compromise the calibration accuracy of simultaneous dual-frequency, round-trip capability.

References

1. Callahan, P. S., "Range Accuracy as a Function of Tracking Frequencies and Calibration Strategy", IOM 315-66, 25 August 1978. (JPL internal document.)

2. Berman, A. L., "The Gravitational Wave Detection Experiment: Description and Anticipated Requirements", in *The Deep Space Network Progress Report 42-46*, Jet Propulsion Laboratory, Pasadena, California, August 15, 1978.

3. Anderson, J. D., and Lau, E. L., "Gravitational Experiments on Solar Probe", in *A Close-up of The Sun*, edited by Neugebauer, M., and Davies, R. W., JPL Publication 78-70, Jet Propulsion Laboratory, Pasadena, California, September 1, 1978.

4. Christensen, C. S., "Difference Range Error Equations for Voyager – Revisited", IOM 314-123, 1 June 1977. (JPL internal document.)

5. Berman, A. L., "Solar Wind Density Fluctuation and The Experiment to Detect Gravitational Waves ir Ultraprecise Doppler Data", in *The Deep Space Network Progress Report 42-44*, Jet Propulsion Laboratory, Pasadena, California, April 15, 1978.

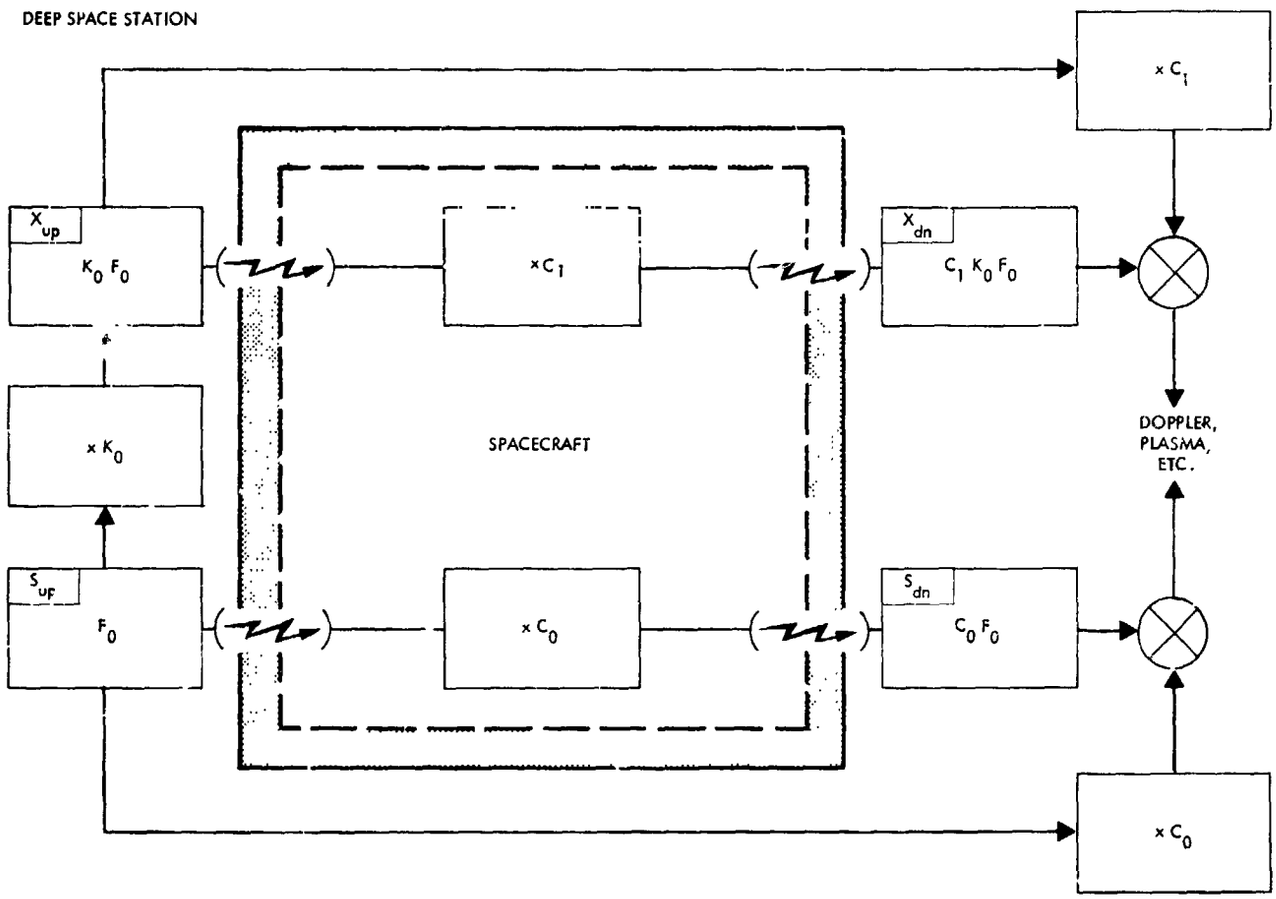

Fig. 1. Simplified functional block diagram of simultaneous dual-frequency uplink and downlink transmission (F_0 = 2.115 GHz, K_0 = 3.404, C_0 = 1.086, C_1 = 1.196)

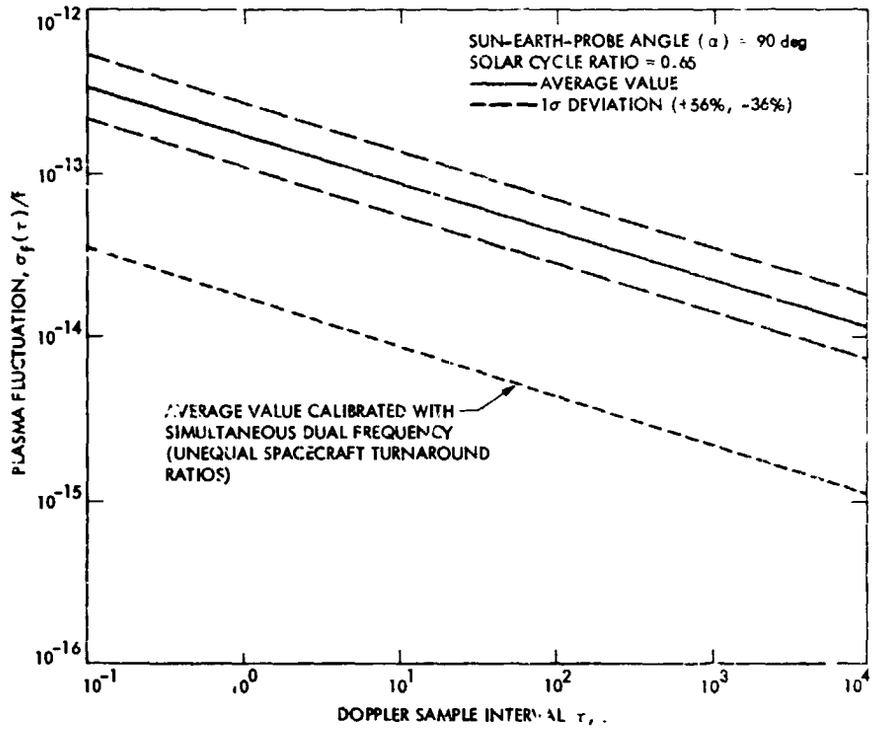

Fig. 2. Two-way X-band plasma fluctuation at solar cycle minimum

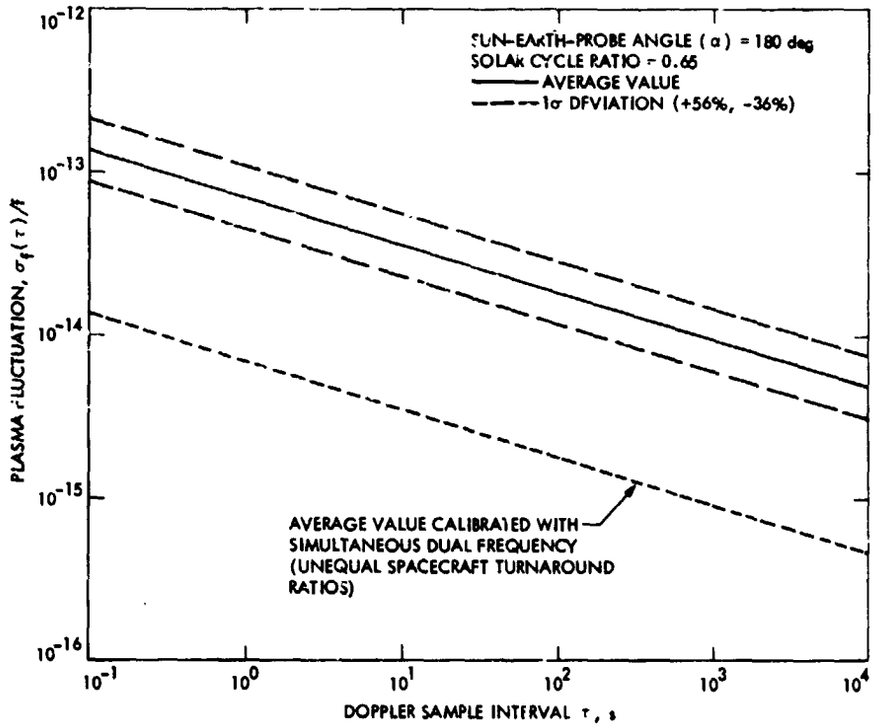

Fig. 3. Two-way X-band plasma fluctuations at solar cycle maximum

A Solar Wind Turbulence Event During the Voyager 1978 Solar Conjunction Profiled via a New DSN Radio Science Data Capability

A. L. Berman and A. D. Conteas
TDA Engineering Office

The Deep Space Network (DSN) has implemented a new radio science data capability within the DSN Tracking System – routine provision of phase fluctuation data concurrently computed over several different time scales. This new capability has been used to observe phase fluctuation spectral characteristics during a rapid increase in solar wind turbulence that occurred during a July 23, 1978, track of the Voyager 1 spacecraft by Deep Space Station (DSS) 11. This article suggests that the new capability will prove quite useful in future studies of variations in Solar Wind phase fluctuation spectral characteristics with, for instance, parameters such as the solar (sunspot) cycle and radial distance.

I. Introduction

During 1977, the Deep Space Network (DSN) implemented a new radio science data capability within the DSN Tracking System. This new capability was described in detail in Berman, Ref. 1. Essentially, the Tracking System routinely (i.e., automatically whenever a spacecraft is being tracked) computes rms phase fluctuation (ϕ) over the fluctuation frequency (ν) range (where ν is related to the Doppler averaging time (τ_a) by the approximate relationship $\nu \approx (36\tau_a)^{-1}$):

$$2.8 \times 10^{-4}\ \text{Hz} < \nu < 2.8 \times 10^{-1}\ \text{Hz}$$

The method of computation is briefly summarized as follows. Doppler samples (accumulated phase in cycles) are provided concurrently at four sample intervals: 0.1 s, 1.0 s, 10.0 s, and 100.0 s. In each case, 18 Doppler *frequency* samples (differenced Doppler accumulated phase divided by averaging time) are differenced with the equivalent *predicted* Doppler frequency. These 18 differenced (actual minus predicted) frequency samples are then fit with a least squares linear curve fit to remove low-frequency trajectory errors (and in the process, low-frequency solar wind induced phase fluctuations). The (scaled) rms phase fluctuation $\tau_a \cdot \sigma_f(\tau_a)$, where σ_f = rms *frequency* fluctuation, is then computed relative to the least squares linear curve fit. Subsequent to the fit, 100 contiguous rms phase fluctuation computations for the 0.1-s Doppler sample interval data, and 10 contiguous rms phase fluctuation computations for the 1.0-s Doppler sample interval data are averaged The final provision of data is summarized in Table 1.

This article presents and briefly describes phase fluctuation data generated during a solar wind turbulence "event" so as to illustrate the potentiality of this new DSN capability.

II. The Data

On July 23, 1978, at about 21:00 Greenwich Mean Time (GMT), the Voyager 1 (ground) observed two-way Doppler data generated by Deep Space Station (DSS) 11 began to indicate that a solar wind flow of (relatively) high turbulence was interdicting the Voyager 1 signal path. At the time, Voyager 1 was at a Sun-Earth-probe angle (SEP) of approximately 6.4 deg. Figure 1 presents the phase fluctuation data for this period. The data presented in Fig. 1 were computed from two-way Doppler data generated by DSS 11. The vertical scale in Fig. 1 is Doppler rms phase fluctuation (ϕ, deg), which is related to rms frequency fluctuation (σ_f) by the approximate relationship (Ref. 1):

$$\phi(\tau_a) \approx \frac{5}{3} \cdot \tau_a \cdot \sigma_f(\tau_a)$$

For the 0.1-, 1.0-, and 10.0-s Doppler sample interval calculations in Fig. 1, ten 3-min phase fluctuation computations (as described in Section I) have been averaged to produce each 30-min (interval) data point. This explains the considerable "smoothness" of the 0.1-, 1.0, and 10.0-s Doppler sample interval data as compared to the 100.0-s Doppler sample interval data. As can readily be seen, the behaviour of the phase fluctuation data in all Doppler sample interval regimes is quite similar. The increase in the 0.1-s Doppler sample interval phase fluctuation data is relatively less than the longer Doppler sample interval data because the 0.1-s Doppler sample interval data contain phase fluctuation components of both the solar wind and the ground tracking system. For the 1.0-, 10.0-, and 100.0-s Doppler sample intervals, the phase fluctuation data are essentially all a result of Solar Wind turbulence.

III. Columnar Solar Wind Phase Fluctuation Spectral Index

The relationship between the columnar (two-dimensional) spectral index is simply (from Berman, Ref. 1, or Douglass, Ref. 2):

$$\phi^2 \propto \nu^{-K_0+1}$$

where

ϕ = RMS phase fluctuation

ν = fluctuation frequency

K_0 = spectral index

Figure 1 additionally provides spectral index data computed from the phase fluctuation data. Inherent to these data is the assumption that the fluctuation spectrum is power-law with frequency. Spectral index data at 30-min intervals were computed for the following frequency ranges:

$$2.8 \times 10^{-3}\ \text{Hz} < \nu < 2.8 \times 10^{-2}\ \text{Hz}$$

$$2.8 \times 10^{-4}\ \text{Hz} < \nu < 2.8 \times 10^{-2}\ \text{Hz}$$

IV. Discussion and Summary

The DSN has implemented a new radio science data capability within the DSN Tracking System -- routine provision of phase fluctuation data concurrently over several different time scales. The columnar solar wind phase fluctuation spectral index can be easily extracted from such data, and hence this new capability should prove quite valuable in studies such as the radial and solar cycle variations of the spectral index.

References

1. Berman, A. L., "Phase Fluctuation Spectra: New Radio Science Information To Become Available in the DSN Tracking System Mark III-77", in *The Deep Space Network Progress Report 42-40*, Jet Propulsion Laboratory, Pasadena, California, August 15, 1977.

2. Douglass, D. H., "Detection of Gravitational Radiation and Oscillations of the Sun via Doppler Tracking of Spacecraft", in *A Close-up of the Sun*, edited by Neugebauer, M., and Davies, R. W., JPL Publication 78-70, Jet Propulsion Laboratory Pasadena, California, September 1, 1978.

Table 1. Provision of phase fluctuation data

Doppler sample interval, s	Number of Doppler samples	Number of estimates averaged	Print-out interval, min
0.1	18	100	3
1.0	18	10	3
10.0	18	1	3
100.0	18	1	30

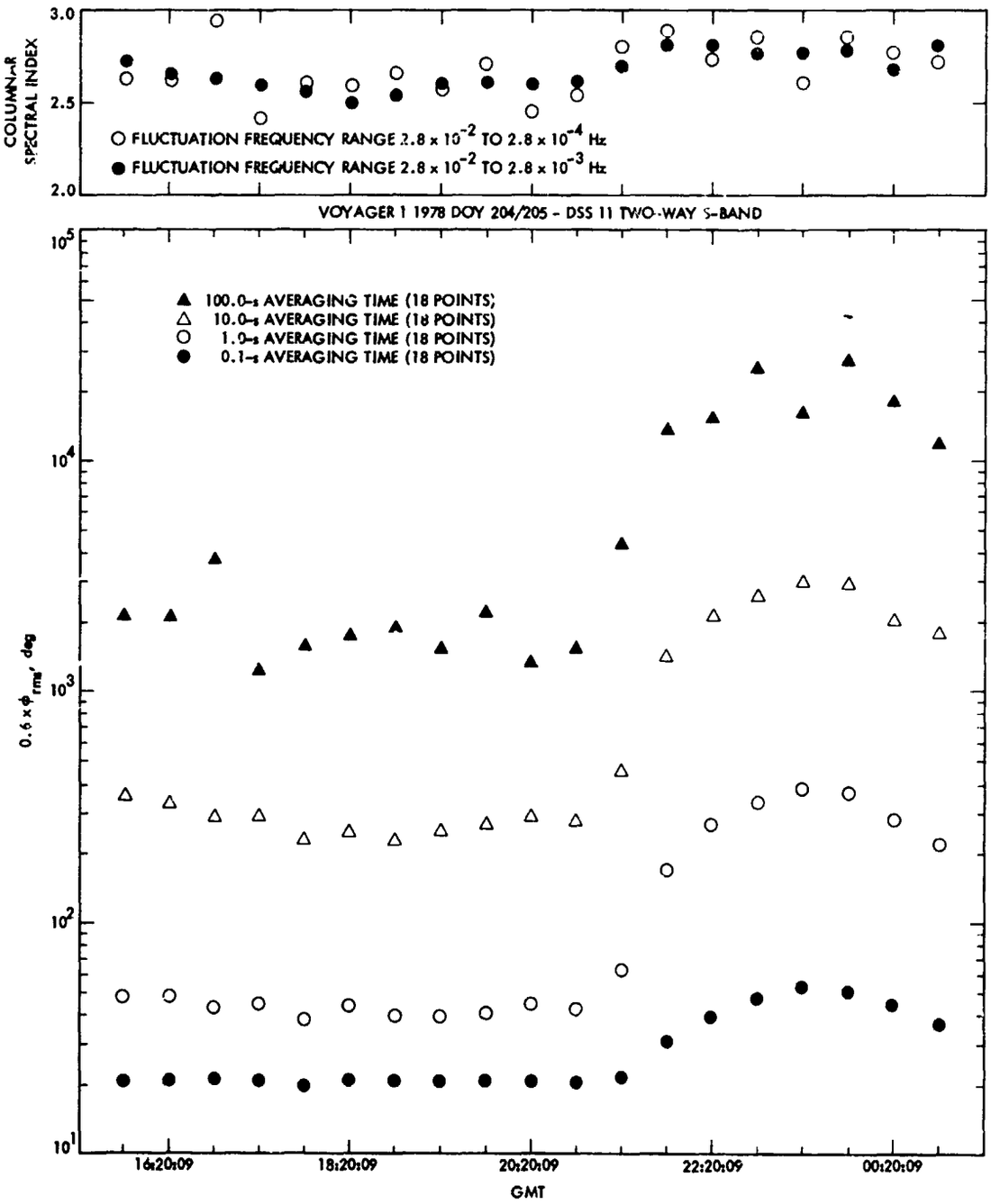

Fig. 1. RMS phase fluctuation and columnar spectral index vs GMT, July 23/24, 1978

Radial and Solar Cycle Variations in the Solar Wind Phase Fluctuation Spectral Index as Determined From Voyager 1978 Solar Conjunction Data

A. L. Berman and A. D. Conteas
TDA Engineering Office

Of current interest is the value of and possible variations in the solar wind phase fluctuation spectral index. This article presents columnar spectral index information that has been extracted from a sizable volume of Voyager 1978 solar conjunction doppler phase fluctuation data. The Voyager 1978 results, when compared to similar information derived from the 1976 Helios and Viking Solar Conjunctions, lead to the following inferences: (1) there has been a significant change in the spectral index from 1976 to 1978; (2) there is continuing evidence that favors a slight (positive) correlation between the spectral index and the solar (sunspot) cycle; (3) there is little or no evidence in support of a radial variation of the spectral index.

I. Introduction

During the last decade, much work has been performed to determine the form of the solar wind fluctuation spectrum. During this period, and through analysis of both spacecraft in-situ and radio scattering measurements, it has become evident that the form of the fluctuation spectrum is best described as power-law with fluctuation frequency (ν); see, for example, Intriligator, et al., Ref. 1; Goldstein, et al., Ref. 2; Unti, et al., Ref. 3; Woo, et al., Ref. 4; and Chang, Ref. 5. It is currently of considerable interest to determine the numerical value of the (power-law) spectral index[1], and, additionally, any possible functional dependencies of the spectral index on:

(1) Fluctuation frequency regime.

(2) Radial distance.

(3) Solar cycle variations.

Recently, Coles, et al., Ref. 6, have determined spectral index variations with both radial distance and fluctuation frequency regime through analysis of intensity scintillation of incoherent radio sources. In contrast to these results, Berman, (Ref. 7), analyzing Viking Doppler phase fluctuation data generated by the Deep Space Network (DSN) during the 1976 solar conjunction, found no indication of a radial dependence of the spectral index. It should be noted, however, that these

[1]The term "spectral index" will specifically imply the *columnar* (two-dimensional) spectral index.

(differing) results were obtained in different regimes of the fluctuation spectrum; whereas the scintillation results from Ref. 6 are for fluctuation frequencies (ν) greater than 0.1 Hz, the Doppler results are for fluctuation frequencies less than 0.03 Hz.

To date, little work has been performed on determining possible variations of the spectral index with solar cycle. Berman recently noted (Ref. 8) that, based on the totality of spectral index measurements to date (1977), the (available) evidence pointed to, at most, only a slight variation of spectral index with solar cycle. Further, Ref. 8 indicated that if indeed correlation did exist between the spectral index and solar cycle, the correlation appeared to be *positive*, i.e., the fluctuation spectrum appeared to be *steeper* during solar cycle (sunspot) maximum.

This article presents the results of extracting spectral index information from a large volume of Doppler phase fluctuation data generated by the DSN during the Voyager 1978 solar conjunction. Analysis of these data indicates:

(1) There was a significant increase in the spectral index between solar cycle minimum (1976) and (near) solar cycle maximum (1978).

(2) There is continued evidence for slight (positive) correlation between the spectral index and the Solar Cycle.

(3) There is little evidence of a significant variation of the spectral index with radial distance (at least in the low frequency portion of the fluctuation spectrum).

II. Helios and Viking Spectral Index Data During 1976

Berman (Refs. 7 and 9) has analyzed a large volume of Doppler phase fluctuation data generated by the DSN during the 1976 solar conjunctions of Helios and Viking. Analysis of the spectral index information derived from the Helios and Viking data yielded the following conclusions (Ref. 7):

(1) The mean value of the spectral index during 1976 was 2.42.

(2) There was little or no indication of a spectral index radial dependence.

Figure 1 (from Ref. 7) presents the spectral index, as computed from Viking Doppler phase fluctuation data, versus Sun-Earth-probe (SEP) angle. The absence of any significant spectral index radial dependence is obvious from inspection of Fig. 1.

III. Voyager Spectral Index Data During 1978

In 1977, the DSN implemented a new capability to allow the convenient extraction of spectral index information from Doppler phase fluctuation data; this capability is described in detail in Refs. 7 and 10. Using this new capability, spectral index information has been computed from Voyager 1 Doppler phase fluctuation data. Very briefly, the spectral index extraction process is predicated on the relationship (Ref. 10):

$$\phi^2 \propto \nu^{-K_0+1}$$

where:

ϕ = rms Doppler phase fluctuation

ν = fluctuation frequency

K_0 = spectral index

The Voyager 1 two-way Doppler phase fluctuation data were analyzed during the periods June 17, 1978. to July 7, 1978, and July 20, 1978, to August 8, 1978. During these periods, the SEP varied between 3.6 deg and 17.9 deg. The fluctuation frequency (ν) range over which the spectral index was computed for the Voyager 1 data was:

$$2.8 \times 10^{-4}\ \text{Hz} < \nu < 2.8 \times 10^{-3}\ \text{Hz}$$

The spectral index information determined from the Voyager 1 Doppler phase fluctuation data is presented in Figs. 2 and 3. Figure 2 presents the spectral index vs day of year (DOY), while Fig. 3 presents the spectral index vs SEP.

The mean value of the spectral index as computed from the Voyager 1 data is $K_0 = 2.67$, as compared to a spectral index mean value of $K_0 = 2.42$ as determined from the Viking and Helios data. This difference is considered statistically significant in light of the large volume of data analyzed in both cases. For the 1976 mean spectral index, 42 pass average (~3 hours of Doppler data) spectral index measurements were available, while in the case of the 1978 mean spectral index, 71 pass average measurements were utilized. Since 1976 constituted solar cycle 20 minimum, and mid-1978 is near (according to Sunspot number) solar cycle 21 maximum, these results can be considered perhaps the strongest evidence to date of (positive) correlation between spectral index and solar (sunspot) cycle.

Figure 3 presents the spectral index vs SEP. Although there appears to be a slight negative slope to the data, it is considered that this is not significant, *particularly* when considered in context of the (smaller) SEP data of Fig. 1, which in no way shows any continuation of such a trend (i.e., a spectral index (negative) correlation with SEP). When considered jointly, it is suggested that Figs. 1 and 3 provide little indication of any significant spectral index radial variation.

IV. Summary and Discussion

A new DSN capability has been utilized to obtain a sizeable volume of spectral index information during the Voyager 1978 solar conjunction. Major conclusions derived from a comparative study of these data with similar data obtained during 1976 solar conjunctions of Helios and Viking are:

(1) There has been a significant change in the spectral index from solar cycle minimum (1976; $K_0 = 2.42$) to (near) solar cycle maximum (1978; $K_0 = 2.67$).

(2) There continues to be evidence for a slight (positive) correlation between spectral index and solar (sunspot) cycle.

(3) There continues to be little or no evidence for a significant variation of spectral index with radial distance.

This new DSN capability is expected to be exercised in future years to derive spectral index information from Voyager solar conjunction Doppler phase fluctuation data, and hence to allow the continued monitoring of spectral index variations during the remainder of solar cycle 21.

References

1. Intriligator, D. S., and Wolfe, J. H., "Preliminary Power Spectra of the Interplanetary Plasma," in *The Astrophysical Journal, Letters*, 162, December 1970.

2. Goldstein, B., and Sisco, G. L., "Spectra and Cross Spectra of Solar Wind Parameters from Mariner 5," in *Solar Wind*, edited by Sonett, C. P., Coleman, P. J., Jr., and Wilcox, J. M. National Aeronautics and Space Administration, Washington, D.C., 1972.

3. Unti, T. W. J., Neugebauer, M., and Goldstein, B. E., "Direct Measurements of Solar Wind Fluctuations Between 0.0048 and 13.3 Hz," in *The Astrophysical Journal*, 180, March 1, 1973.

4. Woo, R., Yang, F., Yip, W. K., and Kendall, W. B., "Measurements of Large Scale Density Fluctuations in the Solar Wind Using Dual Frequency Phase Scintillations," in *The Astrophysical Journal*, Volume 210, Number 2, Part 1, December 1, 1976.

5. Chang, H., *Analysis of Dual-Frequency Observations of Interplanetary Scintillations Taken by the Pioneer 9 Spacecraft*, Doctoral Dissertation, Department of Electrical Engineering, Stanford University, May 1975.

6. Coles, W. A., Rickett, B. J., and Scott, S. L., "Scintillation Observations Near the Sun," in *A Close-up of the Sun*, edited by Neugebauer, M., and Davies, R. W., JPL Publication 78-70, Jet Propulsion Laboratory, Pasadena, California, September 1, 1978.

7. Berman, A. L., "Phase Fluctuation Spectra: New Radio Science Information to Become Available in the DSN Tracking System Mark III-77," in *The Deep Space Network Progress Report 42-40*, Jet Propulsion Laboratory, Pasadena, California, August 15, 1977.

8. Berman, A. L., "Deep Space Telecommunications and the Solar Cycle: A Reappraisal," in *The Deep Space Network Progress Report 42-43*, Jet Propulsion Laboratory, Pasadena, California, February 15, 1978.

9. Berman, A. L., "A Comprehensive Two-Way Doppler Noise Model for Near-Real-Time Validation of Doppler Data," in *The Deep Space Network Progress Report 42-37*, Jet Propulsion Laboratory, Pasadena, California, February 15, 1977.

10. Berman, A. L., and Conteas, A. D., "A Solar Wind Turbulence Event During the Voyager 1978 Solar Conjunction Profiled via a New DSN Radio Science Capability," in *The Deep Space Network Progress Report 42-48*, Jet Propulsion Laboratory, Pasadena, California, December 15, 1978 (this issue).

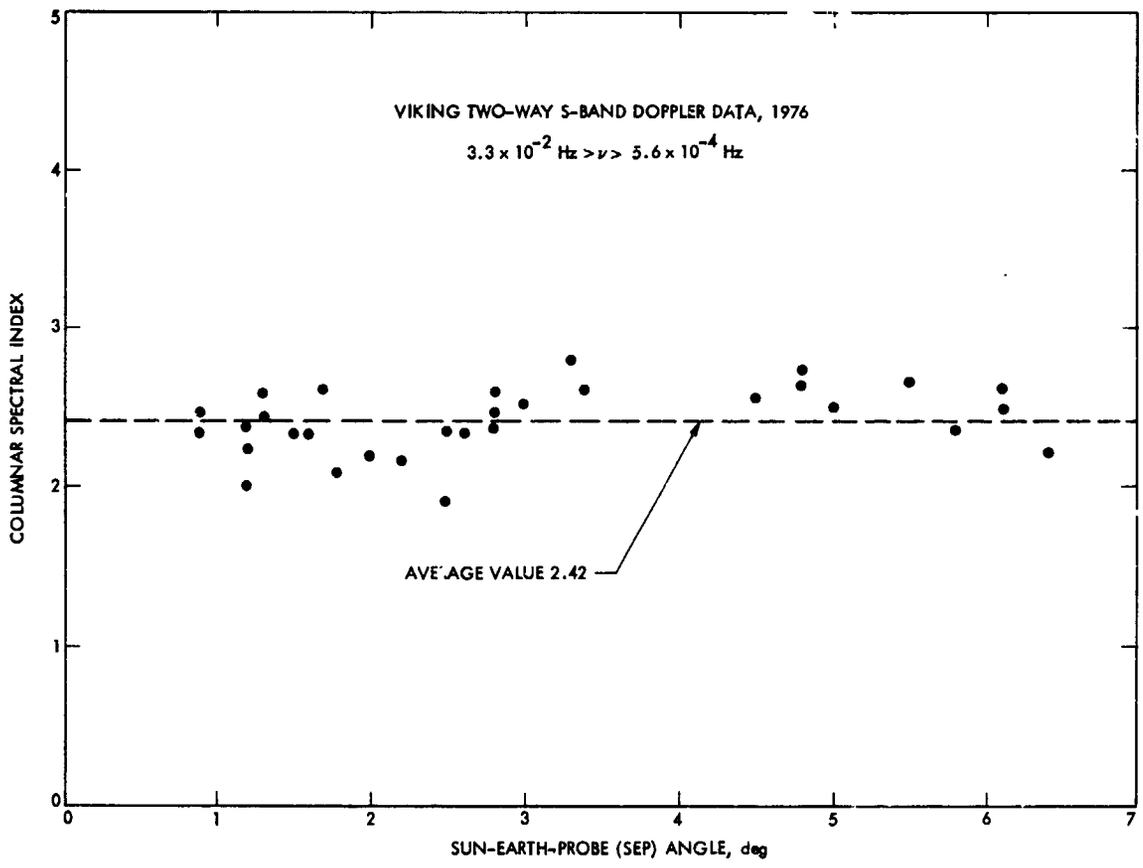

Fig. 1. Columnar solar wind phase fluctuation spectral index vs Sun-Earth-probe angle, 1976

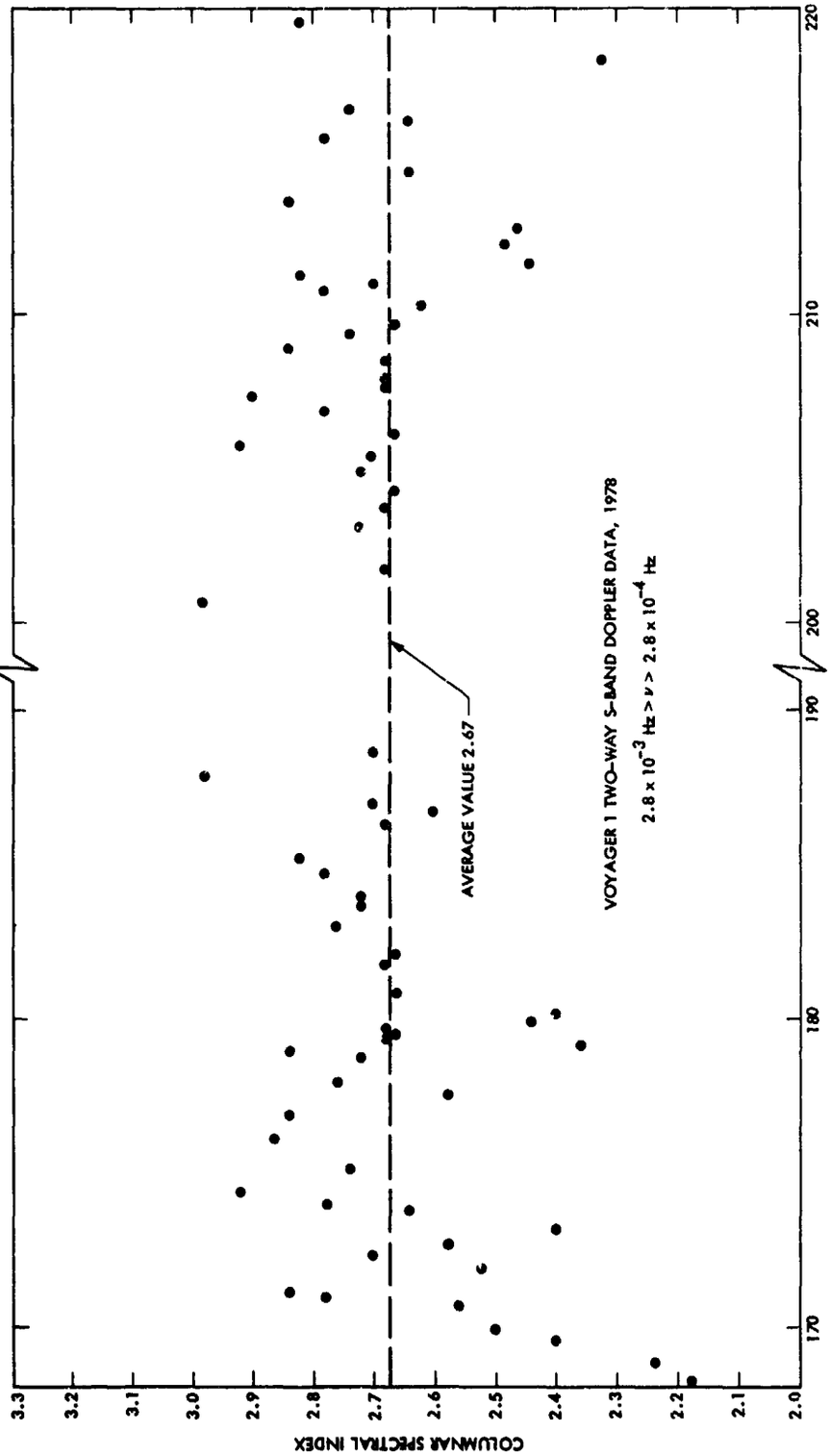

Fig. 2. Columnar solar wind phase fluctuation spectral index vs day of year, 1978

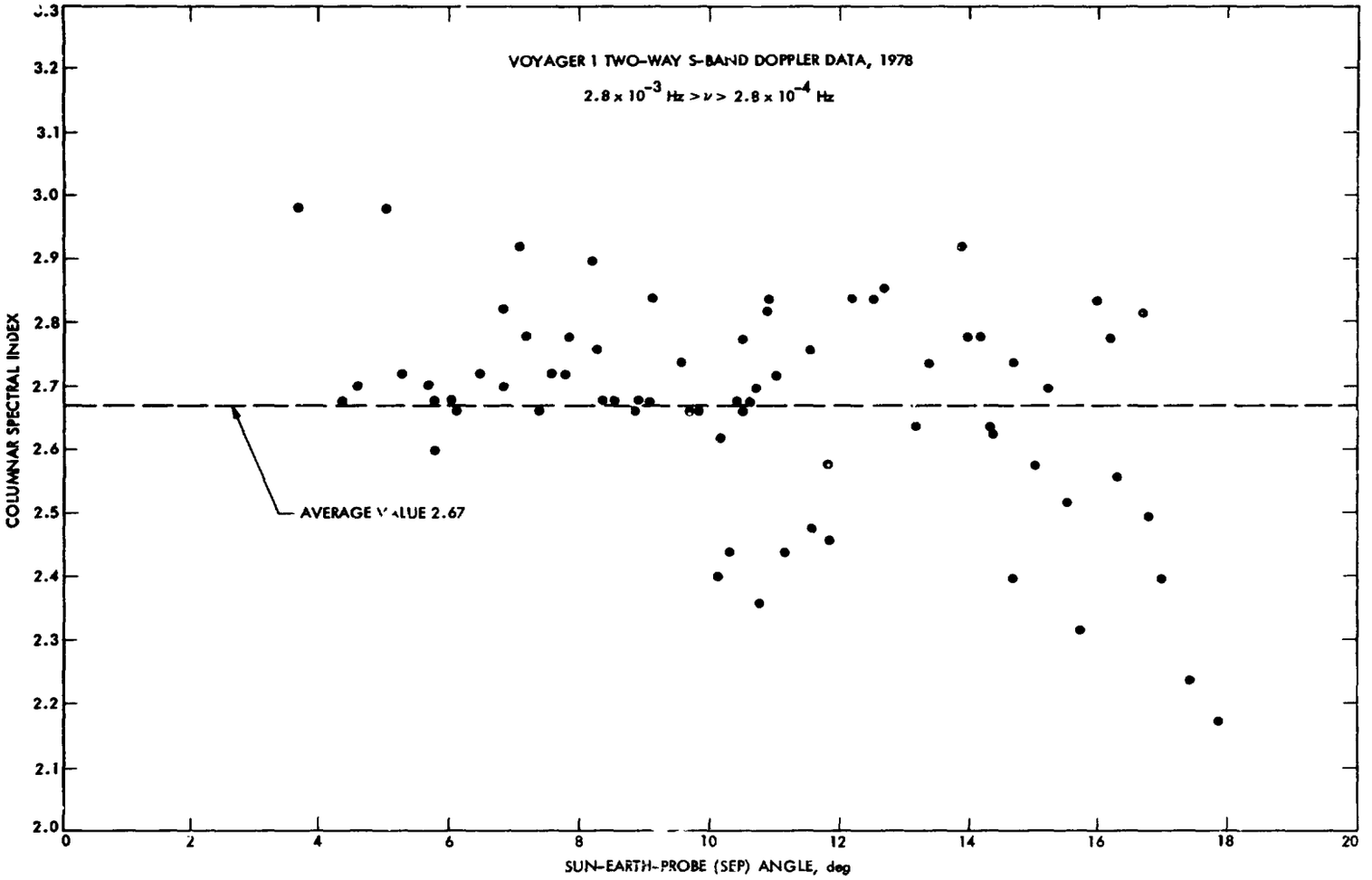

Fig. 3. Columnar solar wind phase fluctuation spectral index vs Sun-Earth-probe angle, 1978

A Simplified Algorithm for Correcting Both Errors and Erasures of R-S Codes

I. S. Reed
University of Southern California

T. K. Truong
TDA Engineering Office

Using the finite field transform and continued fractions, a simplified algorithm for decoding Reed-Solomon codes is developed to correct erasures caused by other codes as well as errors over the finite field $GF(q^m)$, where q is a prime and m is an integer. Such an R-S decoder can be faster and simpler than a decoder that uses more conventional methods.

I. Introduction

Fast real-valued transforms over the group $(Z_2)^m$ were used first by Green (Ref. 1) to decode the (32, 6) Reed-Muller code (Ref. 2) used by the Jet Propulsion Laboratory (JPL) in Mariner and Viking space probes. Gore (Ref. 3) extended Mandelbaum's methods (Ref. 4) for decoding R-S codes (Ref. 5). He proposed to decode R-S codes with a finite field transform over $GF(2^m)$, where m is an integer. Michelson (Ref. 6) implemented Mandelbaum's algorithm and showed that the decoder, using the transform over $GF(2^m)$, requires substantially fewer multiplications than the standard decoder (Ref. 7). Recently, it was shown (Ref. 8) that R-S codes can be decoded efficiently with a combination of the fast transform method and continued fractions.

For a space communication link, it was shown in (Ref. 9) that an R-S code that is concatenated with a Viterbi-decoded convolutional code can be used to reduce the signal-to-noise ratio required to meet a specified bit error rate. Such a concatenated R-S code is implemented presently on the Voyager spacecraft.

In such a concatenated code, the inner convolutional decoder is sometimes able to find only two or more equally probable R-S symbols. Then it is possible to declare an erasure of the R-S symbol, i.e., mark the location of a possible error. The outer R-S code can take advantage of the knowledge of these erasure locations if erasures are reported to the R-S decoder by the Viterbi decoder. Erasures are not reported by the MCD as presently implemented in the DSN.

In this article, a simplified decoding algorithm is developed to correct erasures and errors of R-S codes using both a finite transform and continued fractions. This decoding algorithm is based on the algorithm originally invented by Forney (Refs. 10 and 11). An important advantage of the present decoding technique over previous methods is that a Chien-type search (Refs. 7 and 11) for the roots of the error locator polynomial is completely avoided.

II. On the Decoding of Erasures and Errors

Let n be the block length of an R-S code in $GF(q^m)$. Also let d be the minimum distance of the code where $d = P - 1$. Then $n = P + I$, where P is the number of parity symbols and I is the number of information symbols.

Define the following five different vectors:

$(c_0, c_1, \cdots, c_{n-1})$ = c, code vector

$(r_0, r_1, \cdots, r_{n-1})$ = r, received vector

$(u_0, u_1, \cdots, u_{n-1})$ = u, erasure vector

$(e_0, e_1, \cdots, e_{n-1})$ = e, error vector

$(\tilde{u}_0, \tilde{u}_1, \cdots, \tilde{u}_{n-1})$ = $\tilde{\mathbf{u}}$, new erasure vector

These vectors are related by $\tilde{\mathbf{u}} = \mathbf{e} + \mathbf{u}$ and $\mathbf{r} = \mathbf{c} + \mathbf{u} + \mathbf{e}$.

Suppose that t errors and s erasures occur in the received vector r and that $s + 2t \leq d - 1$. The syndromes are given by

$$S_k = r(\alpha^k) = \sum_{i=0}^{n-1} r_i \alpha^{ki}$$

$$= \sum_{i=0}^{n-1} c_i \alpha^{ki} + \sum_{i=0}^{n-1} u_i \alpha^{ki} + \sum_{i=0}^{n-1} e_i \alpha^{ki} \qquad \text{for } 1 \leq k \leq d-1$$

but

$$\sum_{i=0}^{n-1} c_i \alpha^{ki} = 0 \qquad \text{for } 1 \leq k \leq d-1$$

Thus

$$S_k = \sum_{i=0}^{n-1} u_i \alpha^{ki} + \sum_{i=0}^{n-1} e_i \alpha^{ki}$$

$$= \sum_{j=1}^{s} W_j Z_j^k + \sum_{j=1}^{t} Y_j X_j^k \equiv E_k \qquad \text{for } 1 \leq k \leq d-1 \qquad (1a)$$

In general, let

$$E_k = \sum_{j=1}^{t} Y_j X_j^k + \sum_{j=1}^{s} W_j Z_j^k \qquad \text{for all } k \qquad (1b)$$

where Y_j is the j-th error amplitude, X_j is the j-th error location, W_j is the j-th erasure amplitude, Z_j is the j-th known erasure location, and $E_k = S_k$ is known for $1 \leq k \leq d - 1$.

Following Forney, let the erasure locator polynomial be defined by

$$\tau(x) = \prod_{j=1}^{s} (x - Z_j) = \sum_{j=0}^{s} (-1)^j \tau_j x^{s-j} \qquad (2)$$

This implies

$$\sum_{j=0}^{s} (-1)^j \tau_j Z_k^{s-j} = 0 \qquad \text{for } k = 1, 2, \cdots, s \qquad (3)$$

where $\tau_0 = 1$ and τ_j's are known functions of $Z_1, Z_2, \cdots, Z_s$ for $1 \leq j \leq s$. The Forney syndrome (Ref. 10) is defined by

$$T_i = \sum_{j=0}^{s} (-1)^j \tau_j S_{i+s-j} \qquad \text{for } 1 \leq i \leq d-1-s \qquad (4a)$$

From Eqs. (1a) and (3), we know that τ_j for $j = 1, 2, \cdots, s$ and S_k for $k = 1, 2, \cdots, d - 1$ is known. Thus the T_i's for $1 \leq i \leq d - 1 - s$ are known. In general, let

$$T_i = \sum_{j=0}^{s} (-1)^j \tau_j E_{i+s-j} \qquad \text{for all } i \qquad (4b)$$

where $E_{i+s-j} = S_{i+s-j}$ for $1 \leq i + s - j \leq d - 1$. Then the Forney syndrome T_i is known for $1 \leq i \leq d - 1 - s$.

Now if one substitutes Eq. (1b) into Eq. (4b),

$$T_i = \sum_{j=0}^{s} (-1)^j \tau_j E_{i+s-j}$$

$$= \sum_{j=0}^{s} (-1)^j \tau_j \left[\sum_{k=1}^{t} Y_k X_k^{i+s-j} + \sum_{k=1}^{s} W_k Z_k^{i+s-j} \right]$$

$$= \sum_{k=1}^{t} Y_k X_k^i \sum_{j=0}^{s} (-1)^j \tau_j X_k^{s-j}$$

$$+ \sum_{k=1}^{s} W_k Z_k^i \sum_{j=0}^{s} (-1)^j \tau_j Z_k^{s-j}$$

From Eq. (3) one observes

$$\sum_{k=0}^{s} W_k Z_k^i \sum_{j=0}^{s} (-1)^j \tau_j Z_k^{s-j} = 0$$

Thus,

$$T_i = \sum_{k=1}^{t} Y_k X_k^i \sum_{j=0}^{s} (-1)^j \tau_j X_k^{s-j}$$

$$= \sum_{k=1}^{t} D_k X_k^i \qquad \text{for all } i \tag{5}$$

where the quantities

$$D_k = Y_k \sum_{j=0}^{s} (-1)^j \tau_j X_k^{s-j}$$

for $k = 1, 2, \cdots, t$ are not known.

Now let $T(x)$ be a formal power series in the indeterminate x, defined by

$$T(x) = T_1 x^{-1} + T_2 x^{-2} + T_3 x^{-3} + \cdots$$

$$+ T_{d-1-s} x^{-(d-1-s)} + \cdots \tag{6}$$

Then substituting Eq. (5) into Eq. (6), gives

$$T(x) = \sum_{i=1}^{\infty} T_i x^{-i} = \sum_{i=1}^{\infty} \left(\sum_{k=1}^{t} D_k X_k^i \right) x^{-i}$$

$$= \sum_{k=1}^{t} D_k \sum_{i=1}^{\infty} (X_k x^{-1})^i$$

$$= \sum_{k=1}^{t} D_k \frac{X_k x^{-1}}{1 - X_k x^{-1}} = \sum_{k=1}^{t} D_k \frac{X_k}{x - X_k} = \frac{p(x)}{\sigma(x)} \tag{7}$$

where

$$\sigma(x) = \prod_{k=1}^{t} (x - X_k)$$

is the error locator polynomial and $\deg p(x) < \deg \sigma(x)$. Since T_i is known for $i = 1, 2, \cdots, d - 1 - s$, where $t \leq d - 1$, then, by Theorem 2 in Ref. 8, the error locator $\sigma(x)$ can be obtained by using continued fractions. The roots of $\sigma(x)$ are the locations of the t errors.

Since the locations of the t errors and the s erasures are now known, we may assume that we have the problem of only s' erasures where $s' = t + s$. That is, the only unknowns are the "erasure" amplitudes $\widetilde{W}_1, \widetilde{W}_2, \cdots, \widetilde{W}_{s'}$, the amplitudes of both the error and erasure vectors. The corresponding known locators are $\widetilde{Z}_1, \widetilde{Z}_2, \cdots, \widetilde{Z}_{s'}$. Only the case of erasures need be considered.

Suppose there are $s' \leq d - 1$ erasures. Then $\mathbf{r} = \mathbf{c} + \widetilde{\mathbf{u}}$, where $\widetilde{\mathbf{u}} = \mathbf{u} + \mathbf{e}$ is a new erasure vector in which s' erasures occur where the received vector is $\mathbf{r}$ and $\mathbf{c}$ is the code vector. The syndromes are

$$\widetilde{S}_k = r(\alpha^k) = \sum_{i=0}^{n-1} r_i \alpha^{ki} = \sum_{i=0}^{n-1} c_i \alpha^{ki} + \sum_{i=0}^{n-1} \widetilde{u}_i \alpha^{ik}$$

$$\text{for } k = 1, 2, \cdots, d - 1$$

but

$$\sum_{i=0}^{n-1} c_i \alpha^{ki} = 0 \qquad \text{for } k = 1, 2, \cdots, d - 1$$

Thus

$$\widetilde{S}_k = \sum_{i=0}^{n-1} \widetilde{u}_i \alpha^{ki}$$

$$= \sum_{j=1}^{s'} \tilde{W}_j \tilde{Z}_j^k \equiv U_k \qquad \text{for } k = 1, 2, \cdots, d-1 \qquad (8a)$$

where $\tilde{W}_j$ are the j-th amplitudes of the erasure and error vectors and $\tilde{Z}_j$ are the j-th known locations of the original erasure and error vectors. Note that $\tilde{S}_k$ actually equals S_k in Eq. (1a) for $k = 1, 2, \cdots, d-1$. In general, let

$$U_k = \sum_{j=1}^{s'} \tilde{W}_j \tilde{Z}_j^k \qquad \text{for all } k \qquad (8b)$$

where $U_k = \tilde{S}_k$ for $k = 1, 2, \cdots, d-1$. The erasure polynomial of the original erasure and error vector is given by

$$\tilde{\tau}(x) = \sum_{j=1}^{s'} (x - \tilde{Z}_j) = \sigma(x)\tau(x) = \sum_{k=0}^{s'} (-1)^k \tilde{\tau}_k x^{s'-k}$$

where $\tilde{\tau}_0 = 1$, $s' = t + s$, and $\tau(x)$ and $\sigma(x)$ are given in Eqs. (2) and (7), respectively. Hence

$$\tilde{\tau}(\tilde{Z}_i) = \sum_{k=0}^{s'} (-1)^k \tilde{\tau}_k \tilde{Z}_i^{s'-k} = 0 \qquad \text{for } i = 1, 2, \cdots, s' \qquad (9)$$

Multiplying Eq. (9) by $\tilde{W}_i \tilde{Z}_i^j$,

$$\tilde{W}_i \tilde{Z}_i^{s'} \tilde{Z}_i^j + \sum_{k=1}^{s'} (-1)^k \tilde{\tau}_k \tilde{W}_i \tilde{Z}_i^{s'-k} Z_i^j \qquad (10)$$

Summing Eq. (10) on i for $i = 1, 2, \cdots, s'$, yields

$$\sum_{i=1}^{s'} \tilde{W}_i \tilde{Z}_i^{s+j} + \sum_{i=0}^{s'} \sum_{k=1}^{s'} (-1)^k \tilde{\tau}_k \tilde{W}_i \tilde{Z}_i^{s'+j-k} = 0$$

Thus

$$U_{s+j} + \sum_{k=1}^{s'} (-1)^k \tilde{\tau}_k U_{s+j-k} = 0 \qquad \text{for } j \geq 1$$

In general,

$$U_\ell = -\sum_{k=1}^{s'} (-1)^k \tilde{\tau}_k U_{\ell-k} = 0 \qquad \text{for } \ell > d-1 \qquad (11)$$

where $U_1, U_2, \cdots, U_{d-1}$ are known. From Eq. (11) one obtains the rest of the transform of $\tilde{\mathbf{u}}$, i.e., U_ℓ for $0 \leq \ell \leq n-1$. The vector of amplitudes $\tilde{\mathbf{u}}$ is found by taking the inverse transform over $GF(q^m)$ of U_ℓ for $\ell = 0, 1, 2, \cdots, n-1$. Finally, the original n-tuple code vector can be obtained by subtracting $\tilde{\mathbf{u}}$ from the received vector $\mathbf{r}$.

Let us recapitulate the decoding of R-S codes for both errors and erasures using the transform over $GF(q^m)$ and continued fractions. This algorithm is composed of the following five steps:

(a) Compute the transform over $GF(q^m)$ of the received vector n-tuple, $(r_0, r_1, \cdots, r_{n-1})$, i.e.,

$$S_k = \sum_{i=0}^{n-1} r_i \alpha^{ik} = U_k \qquad k = 0, 1, \cdots, d-1$$

where $r_i \in GF(q^m)$, α is an element of order n, and d is the minimum distance of the R-S code.

(b) Compute τ_j for $j = 0, 1, 2, \cdots, s$ from the erasure locator polynomial

$$\tau(x) = \prod_{j=1}^{s} (x - Z_j) = \sum_{j=0}^{s} (-1)^j \tau_j x^{s-j}$$

where s is the number of erasures in the received vector. The Z_j's for $1 \leq j \leq s$ are the known erasure locations. Then compute the Forney syndrome T_n for $1 \leq n \leq d-1-s$ from the equation

$$T_i = \sum_{j=0}^{s} (-1)^j \tau_j E_{i+s-j} \qquad \text{for } 1 \leq i \leq d-1-s$$

where τ_j for $1 \leq j \leq s$ and $E_j = S_j$ for $1 \leq j \leq d-1$ are known.

(c) Use continued fractions to determine the error locator polynomial $\sigma(x)$ from the known T_i's for $1 < i \leq d-1-s$.

(d) Compute the erasure and error locator polynomials from the equation

$$\tilde{\tau}(x) = \sigma(x)\tau(x) = \sum_{k=0}^{s+t} (-1)^j \tilde{\tau}_k x^{s+t-j}$$

where $\sigma(x)$ and $\tau(x)$ are the known polynomial. Then

compute the rest of the transform of the erasure and error vector from the equation

$$U_\ell = \sum_{k=1}^{s+t} (-1)^k \tilde{\tau}_k U_{\ell-k} \qquad \text{for } \ell > d-1$$

where $U_\ell = S_\ell$ for $1 \leq \ell \leq d-1$.

(e) Invert the transform to recover the error and erasure vector, then obtain the corrected code vector.

To illustrate the decoding procedure for correcting errors with erasures, a simple example of an R-S code over $GF(17)$ is now presented.

Example: Let $GF(17)$ be the field of integers, modulo the Fermat prime $F_2 = 2^{2^2} + 1 = 17$. We consider the correction of one error and two erasures in an eighttuple R-S code over $GF(17)$. For this case $n = 8$, $d-1 = P = 4$, $t = 1$, $s = 2$, and $d - 1 = 2t + s$.

Let $\mathbf{c} = (5, 2, 12, 15, 2, 3, 2, 1)$ be transmitted. Assume the erasure vector is $\mathbf{u} = (0, 0, -3, 0, 0, -2, 0, 0)$ and the error vector is $\mathbf{e} = (0, 2, 0, 0, 0, 0, 0, 0)$. Then $\tilde{\mathbf{u}} = \mathbf{u} + \mathbf{e} = (0, 2, -3, 0, 0, -2, 0, 0)$ is a new erasure vector. Hence the received vector is $\mathbf{r} = \mathbf{c} + \mathbf{u} + \mathbf{e} = (5, 4, 9, 15, 2, 1, 2, 1)$.

Now the syndromes S_k for $\mathbf{r}$ are

$$U_k = S_k = r(2^k) = \sum_{i=0}^{7} r_i 2^{ki}$$

$$= 2(2^k)^1 - 3(2^k)^2 - 2(2^k)^5$$

$$\text{for } 1 \leq k \leq d-1 = 4$$

That is, $U_1 = S_1 = -4$, $U_2 = S_2 = 3$, $U_3 = S_3 = 10$, and $U_4 = S_4 = -3$. The erasure locator polynomial is given by

$$\tau(x) = \prod_{i=1}^{2} (x - Z_i) = (x - 2^2)(x - 2^5) = (x - 4)(x - 32)$$

$$= x^2 - 2x + 9$$

Thus we obtain $\tau_0 = 1$, $\tau_1 = 2$, and $\tau_2 = 9$. Then the Forney syndromes are

$$T_n = \sum_{j=0}^{s} (-1)^j \tau_j S_{n+s-j} = \sum_{j=0}^{2} (-1)^j \tau_j S_{n+2-j}$$

$$= S_{n+2} - 2S_{n+1} + 9S_n \qquad \text{for } 1 \leq n \leq d-1-s = 2$$

Hence $T_1 = 2$, and $T_2 = 4$. The power series for $T(x)$ is

$$T(x) = T_1 x^{-1} + T_2 x^{-2} + \cdots + T_{d-1-s} x^{-(d-1-s)} + \cdots$$

$$= 2x^{-1} + 4x^{-2} + 8x^{-3} + \cdots = \frac{D(x)}{\sigma(x)}$$

Since $d - 1 - s = 2t = 2$, by Theorem 2 in Ref. 8, $\sigma(x)$ can be determined by the use of continued fractions. Thus, $T(x) = 2/(x - 2)$. Hence $\sigma(x) = x - 2$.

The erasure and error locator polynomial is

$$\tilde{\tau}(x) = \sigma(x)\tau(x) = (x - 2)(x^2 - 2x + 9) = x^3 - 4x^2 + 13x - 1$$

Thus, $\tilde{\tau}_0 = 1$, $\tilde{\tau}_1 = 4$, $\tilde{\tau}_2 = -4$, and $\tilde{\tau}_3 = 1$. The rest of the transform for $\tilde{\mathbf{u}}$ is given by

$$E_k = \tilde{\tau}_1 U_{k-1} - \tilde{\tau}_2 U_{k-2} + \tilde{\tau}_3 U_{k-3}$$

$$= 4U_{k-1} + 4U_{k-2} + 1U_{k-3} \qquad \text{for } k \geq 5$$

Thus, $U_5 = -3$, $U_6 = 3$, $U_7 = -3$, and $U_8 = U_0 = -3$. The inverse transform over $GF(17)$ of the U_k for $0 \leq k \leq 7$ is given by

$$\tilde{u}_i = 8^{-1} \sum_{k=2}^{7} U_k 2^{-ik} = (-2) \sum_{k=0}^{7} U_k 2^{-ik}$$

$$\text{for } i = 0, 1, 2, \cdots, 7$$

Hence, $\tilde{\mathbf{u}} = (0, 2, -3, 0, 0, -2, 0, 0)$. The corrected code vector is thus

$$\mathbf{c} = \mathbf{r} - \tilde{\mathbf{u}} = (5, 4, 9, 15, 2, 1, 2, 1) - (0, 2, -3, 0, 0, -2, 0, 0)$$

$$= (5, 2, 12, 15, 2, 3, 2, 1)$$

Acknowledgement

The authors wish to thank Dr. N. A. Renzetti, Manager of Tracking and Data Acquisition Engineering of the Jet Propulsion Laboratory for his continued support and encouragement of the research which led to this paper. The first author also appreciates the encouragement and support he got from Mr. Glen W. Prestor of the Institute for Defense Analyses to pursue this topic.

References

1. Green, R. R., "Analysis of a Serial Orthogonal Decoder," *Space Programs Summary 37-53*, Vol. III, 1968, pp. 185-187. Jet Propulsion Laboratory, Pasadena, California.
2. Reed, I. S., "A Class of Multiple Error-Correcting Codes and the Decoding Scheme," *IRE Trans.*, PFIT-4, 1954, pp. 38-49.
3. Gore, W. C., *Transmitting Binary Symbols with Reed-Solomon Code*, Johns Hopkins EE Report No. 73-75, April 1973.
4. Mandelbaum, D., "On Decoding Reed-Solomon Codes," *IEEE Trans. on Inform. Theory*, Vol. IT-17, No. 6, November 1971, pp. 707-712.
5. Reed, I. S., and Solomon, G., "Polynomial Codes Over Certain Finite Fields," *J. Soc. Indus. Appl. Math.*, Vol. 8, June 1960, pp. 300-304.
6. Michelson, A., *A New Decoder for the Reed-Solomon Codes Using a Fast Transform Technique*, Systems Engineering Technical Memorandum No. 52, Electronic Systems Group Eastern Division GTE Sylvania, August 1975.
7. Peterson, W. W., *Error-Correcting Codes*, MIT Press, Cambridge, Mass., 1961, pp. 168-169.
8. Reed, I. S., Scholtz, R. A., Truong, T. K., and Welch, L. R., "The Fast Decoding of Reed-Solomon Codes Using Fermat Theoretic Transforms and Continued Fractions," *IEEE Trans. on Inform. Theory*, Vol. IT-24, No. 1, January 1978, pp. 100-106.
9. Odenwalder, J., et al., *Hybrid Coding Systems Study Final Report*, Linkabit Corp., NASA CR 114, 486, September 1972.
10. Forney, G. D., "On Decoding BCH Codes," *IEEE Trans. on Inform. Theory*, Vol. IT-11, October 1965, pp. 549-557.
11. Berlekamp, E. R., *Algebraic Coding Theory*, McGraw Hill, New York, 1968.

D/3

N79-16013

Evaluation of the DSN Software Methodology

A. Irvine
TDA Engineering Office

M. McKenzie
TDA Planning Office

This article describes the effects of the DSN software methodology, as implemented under the DSN Programming System, on the DSN Mark III Data Subsystems Implementation Project (MDS). The software methodology is found to provide a markedly increased visibility to management, and to produce software of greater reliability at a small decrease in implementation cost. It is also projected that additional savings will result during the maintenance phase. Documentation support is identified as an area that is receiving further attention.

I. Introduction

This article describes the quantitative and qualitative effects of the software methodology (Ref. 1) as implemented under the DSN Programming System, on the DSN Mark III Data Subsystems Implementation Project (MDS). The period in the life cycle of the MDS that was studied extended from September 1974 through November 1976. During this period, approximately 100,000 lines of application code were delivered as well as diagnostic and system software.

The scope of this article covers the implementation of the approximately 100,000 lines of application code that can be directly allocated to the following subsystems:

DCD	Command
DTM	Telemetry
DTK	Tracking
DMC	Monitor
DTT	Test and Training
CMF	Communications Monitor and Formatter
DST	Host

The subsystems are broken down by size in Table 1.

The effects of the methodology on a single subsystem were studied in detail and the results, with corroboration from a second subsystem, were extrapolated for the entire effort. In addition to this quantitative evaluation of the MDS implementation, a qualitative evaluation by cognizant software engineers is included at the end of the report.

II. Software Methodology

At the start of the MDS Project most of the Standard Practices governing software implementation had been formulated but were as yet unpublished. However, the concepts governing the methodology were well known and interim documents were published to guide software implementation. The princi-

pal concepts used in the MDS software effort and implied by the term "methodology" in this report are:

(1) Structured Programming.

(2) Top-down Development.

(3) Visibility Reporting.

(4) Management Reviews.

(5) Documentation.

III. Impact of Methodology on the Command Subsystem

The Deep Space Station Command Subsystem (DCD) was chosen as a representative system for the MDS for the following reasons:

(1) The DCD software was of the "average" size of the MDS subsystem software.

(2) The DCD was the best documented subsystem in terms of statistics gathered during the project lifetime under study.

(3) The DCD development team most closely adhered to the methodology.

Several important milestones should be noted that occurred during the Command subsystem implementation and represented application of the methodology. These milestones were:

The Software Requirements Document (SRD) published for DCD 3/3/75

The Software Definition Document (SDD) published for DCD 9/19/78

DCD High-Level Design Review 11/13/75

MDS System Level Review 3/13/76

Work Breakdown Structure (WBS) Methodology applied 4/1/76

Monthly Management Reporting started 5/1/76

Weekly Reports 9/8/76

The impact of these milestones will be discussed.

A. Visibility

Application of the methodology resulted in a series of milestones that were designed to increase management visibility. Visibility was indeed increased; an example is found in the management of the subsystem delivery date. The SRD reported an estimated delivery date of 1 August 1976. By the time the SDD was published, six months later, the estimated delivery date had slipped one month. Six months later, at the MDS System Level Review, a further slip of two months for the estimated delivery date had occurred. The successive slips of estimated delivery date can be projected (see Fig. 1). This projection is nonlinear and, as the desired delivery date is approached, the number of slips tends to increase. This slip in estimated delivery date was typical for all subsystems, but is illustrated only for the DCD.

It was possible because of the visibility to determine seven months in advance of the need date that the actual delivery date of the software was slipping. Increased visibility plus the application of the WBS methodology allowed the splitting of the effort into two phases. The software necessary to meet first priority requirements was identified and that portion of the software was delivered as a first phase, thereby pulling the delivery date back to the need date. Without corrective action, delivery would have taken place four to five months late.

B. Anomalies

Anomalies were not originally reported for all subsystems and original published anomaly reports do not reflect the DTT or DST subsystems. For the MDS, approximately 200 anomalies were reported at verification time and during acceptance testing at CTA 21. After acceptance testing, approximately 90 more were uncovered.

For the DCD, 77 anomalies were reported during verification testing and acceptance testing, and 43 after acceptance testing. While the anomaly curve for the DCD presents the typical curve exhibited for the MDS (Figs. 2 and 3), it can easily be determined that the rate is approximately twice that for the project as a whole.

Possible causes for this phenomenon could be:

(1) The software was not ready for delivery.

(2) Reporting of preacceptance test anomalies was more comprehensive than for other subsystems.

(3) The software was more difficult.

(4) The software was considered more crucial to flight operations and therefore more rigorously tested.

(5) The methodology does not affect the number of anomalies.

Close investigation shows that reasons (2) and (4) are probably the true reasons for this phenomenon. It has already been mentioned that the DCD was the best documented subsystem and team members adhered most closely to the meth-

odology, and therefore were more meticulous about reporting errors during the verification phase. Extensive performance test programs were written that exercised the software extensively.

Even at the rate of 4.8 errors per 1000 lines of code prior to delivery, the DCD software compares favorably to the industry average of 18 per 1000 lines of code (see Refs. 2, 3, 4).

C. Implementation Cost

One measure of the effectiveness of a programming methodology is the productivity rate in delivered lines of source code per man-month (LOC/mm). An industrial average productivity rate is available for projects produced without the elements of the software methodology. For a comparison, it is desirable to determine the corresponding productivity rate for the Command Subsystem.

It is felt that for a fair comparison, only equivalent activities should be included in the productivity measure. Thus, included in the Command manpower measure is the direct effort associated with technical manpower, derived not from the System for Resource Management (SRM), but as a direct translation of time expended by personnel in the various tasks associated with software implementation such as designing, coding, testing, and documentation. The time spent by engineering personnel on documentation is included but not the costs of support people, reproduction, and other costs involved in the production of the documents themselves. Time expended was derived primarily from the DCD Operational Software Development Schedule and Manpower Allocation Chart.

Figure 4 represents the manpower loading of the DCD during the time span under discussion. Studies of available data from industry (Refs. 5 and 6) indicate that an average of 3.2 persons per month (200 LOC/mm) should have been utilized to produce the necessary code. Instead only an average of 2.7 (237 LOC/mm) persons were employed. Over the 25-month period, a cost savings of 1 person was achieved, or approximately $50,000 for one subsystem.

A second subsystem was studied to corroborate the productivity gains found in the Command Subsystem. The Communications Monitor and Formatter (CMF) was chosen and the CMF man-power loading is shown in Fig. 5. Again, based on an industry productivity average of 200 lines of code per month (Refs. 5 and 6), the savings were 17.3 man months.

The increase in productivity can be considered significant for both subsystems because it exceeds one standard deviation from the mean. The result reinforces the belief that small but significant direct implementation cost savings were obtained with the use of the software methodology.

IV. Software Development Period

The development period of 25 months used to develop cost estimates is an extremely conservative one consisting of starting where the first known manpower could be attributed to the project. There are many valid and cogent reasons why a later date may be taken. The implementation schedule (Fig. 6) published at the High Level Design Review shows a start date for software implementation at approximately January 1975. If this date is taken as the start of the development period then the following productivity figures can be derived:

DCD	256 LOC/month
CMF	274 LOC/month

The savings would then be:

DCD	17.4 man/months
CMF	23.3 man/months

or approximately $167,000 for just the two subsystems.

V. Documentation

As stated previously, the productivity measure includes engineering time spent on design, code, testing, and documentation, but does not include special documentation support required by the software methodology. For the MDS, documentation support was provided by the Software Production Management and Control (SPMC) center, and is discussed below.

Despite the methodology requirements to produce documentation before or at least concurrent with code, the delivery of formal, validated documentation has consistently lagged behind transfer of the code. This lag has, for many subsystems, been as long as a year and is partially due to the volume of documentation produced

Walston and Felix of IBM (Ref. 7) predict on the basis of 46 software projects of varied purposes and methodologies, that about 800 pages of documentation is produced for a subsystem the size of Command. The values for one standard deviation are 400 pages and 1250 pages of documentation. The Command Subsystem produced at least 1600 pages (Table 2). This value is higher than the average found by IBM, and indicates that the methodology results in a higher volume of documentation.

Extrapolation of information supplied by DSN Data Systems indicates that documentation support[1] for the DCD cost $69,000. This is slightly more than the productivity gains shown in Section III, and does not include costs incurred after the time-span of this study. Although the documentation cost is negating productivity gains in the implementation phase, these costs should be offset in the maintenance phase. In the absence of hard data, the cost and volume of documentation required by the methodology is being analyzed.

VI. Maintenance Phase

Unfortunately, the maintenance and operations phase of the MDS system has just begun, so there is no quantitative cost data. Nevertheless, two pieces of information indicate that maintenance of the software will be less costly per LOC than previous projects. First, though given extensive testing, the number of anomalies was low. Secondly, another project produced concurrently with the software methodology showed increased software maintainability. There is no reason to expect a decrease in maintainability, and every reason to expect an increase with the use of the software methodology. Thus, it is predicted that there will be additional savings during the maintenance phase of the MDS.

VII. Conclusions from Quantitative Study

The major quantitatively measurable benefits derived from the methodology discussed in this report appear to be threefold:

(1) The ability to deliver software on time by providing greater visibility and allowing management to intervene before projected slips actually impact delivery schedule.

(2) A lower anomaly rate than the reported industry average, which indicates better software and predicts decreased maintenance costs.

(3) Small but significant cost savings in manpower resulting in lower implementation costs. These savings will increase as the documentation problem is addressed.

[1] Documentation support, as used here, is defined as all the support functions performed by the SPMC for the Command Subsystem. Thus, included in the $69,000 figure are the following: documentation production, editing, and reproduction costs; computer operator costs for disk generation, job runs, source code updating, disc preparation, operating system copies, and module assembly; and code support costs such as the maintenance of the code library.

VIII. Qualitative Evaluation—Benefits

In addition to the quantitative evaluation of the software methodology, a qualitative study was performed using interviews and questionnaires of cognizant software individuals. Qualitative, rather than quantitative, evaluations were sought for several reasons. Record-keeping is a part of the methodology, but quantitative data are often unavailable for older projects. It is also difficult to obtain numeric information from people recalling old projects: often those who directed old projects are no longer at JPL, and data from memory may not be sufficiently accurate for a valid comparison. Thus, the best information to be gained from these individuals is qualitative.

A specific questionnaire and open discussion format were used in the interview process. The programmers and managers were also asked to relate their experiences on projects conducted prior to addition of the software methodology, and specify areas in which the methodology would have been beneficial. The results of the interviews show a number of common impressions and experiences, which are discussed below.

The primary problem observed in older software projects was a failure to transfer to operations on schedule. Often accompanying this overrun in schedule was an overrun in budget. With these two conditions, and pressure to transfer as soon as possible, documentation suffered and maintenance was difficult once transfer was achieved. The people interviewed noted a number of causes that produced this condition.

The first was the general difficulty in accurately predicting task complexity, required resources, and the final amount of code. Cost and schedule overruns occurred and some incompatibilities with hardware resulted. This problem not only affected past DSN projects, but still affects the software industry as a whole. Nevertheless, it is felt that the methodology's requirements for modularization and Work Breakdown Structure, with a strong emphasis on design, strongly support better schedule, cost, and resource planning.

A second cause of overruns noted by the software personnel was frequent changes in requirements. This instability disrupted schedules and necessitated numerous releases and transfer liens. The software methodology addresses this problem by formalizing the requirements process and enforcing approval of requirement changes.

Occasionally noted was the condition in which the project was due for transfer and management then learned it was far from complete. Management had not adequately monitored

the progress of the project. Again, a benefit of the methodology is that it includes the Work Breakdown Structure, design reviews, and formal milestones, which all address the monitoring of project progress.

The software projects discussed in the interviews all had late and/or insufficient documentation, and major transfer liens were frequent against these documents. Numerous problems resulted: the project was delayed, new personnel found it difficult to work on the software, or testing and debugging required excessive resources. It is felt that the concurrent documentation and design review requirements of the methodology certainly ease these problems. Nevertheless, some documentation is still late. This is partly attributed to flowcharts that sometimes require as long as a month for machine production. By that time, they must often be resubmitted to include changes that occurred during that month. A faster method of documentation production was strongly suggested by the software personnel.

The final cause of project overruns brought out in the interviews was excessive errors in the software. Either major pretransfer testing was required, or numerous bugs were found after transfer. Neither case is desirable. The personnel interviewed felt the modularization, emphasis on design, and formal testing incorporated in the methodology result in less testing, fewer anomolies, and easier debugging.

In summary, projects in the past have often encountered difficulties with schedules and resources, specification changes, management visibility, documentation, and testing. The DSN Software Methodology provides a good structure with which to control these problems.

V. Qualitative Evaluation—Suggested Improvements

In addition to benefits resulting from the software methodology, the software people suggested the following methodology improvements that would produce even more cost-effective software:

(1) The methodology requirements are occasionally not applicable to a specific project, and obtaining a waiver requires time. Perhaps, with a growing experience in using the methodology, a list of requirements by project size, cost, and type could be developed.

(2) The projects still find themselves caught between documentation requirements and the scheduled transfer date. Part of the problem is felt to lie in the slow turnaround time for finished documentation. Also, the requirement of low-level flowcharting results in a great deal of production and revision time. It is suggested that either (a) only higher-level flowcharting be required, (b) a program design language tool be used in place of flowcharts, or (c) a quick method of flowchart production be found. In all, the software personnel feel that flowcharting currently requires that the programmer cater to the machine, rather than the reverse.

(3) The inclusion of programmers, operators, Cognizant Development Engineers (CDEs), and customers in the requirements and broad design process should be encouraged even more than is currently done.

(4) Too much emphasis is given to the quantity of response to the methodology rather than the quality of the response. An effort should be made to determine levels of quality based on maintainability and error rate after transfer.

(5) The methodology can help standardize the development of software and control the flow of projects, but it cannot force a bad manager or programmer into good performance. A key also lies in the people who perform the job.

References

1. *Standard Practices for the Implementation of Computer Software*, edited by A. P. Irvine, JPL Publication 78-53. Jet Propulsion Laboratory, Pasadena, Calif. September 1, 1978.

2. Michael E. Fagen, *Design and Code Inspections and Process Control in the Development of Programs*, IBM Technical Report TR 21.572, Dec. 17, 1974.

3. J. C. Kickson, et al., "Quantitative Analysis of Software Reliability," *Proc. 1972 IEEE Annual Reliability and Maintainability Symposium*, N.Y., January 1972, pp. 148-157.

4. M. L. Shooman, "Probabilistic Models for Software Reliability Prediction," *Proc. 1972 International Symposium on Fault-Tolerance Computing*, Newton, Mass., June 1972, pp. 211-215.

5. Steve Caine, of Caine, Farber and Gordon, Inc. Private Communication, Oct. 1976.

6. Stephen R. McCommon, "Applied Software Engineering: A Real-Time Simulator Case History," *IEEE Transactions on Software Engineering*, Vol. SE-1, No. 4, Dec. 1975, p. 383.

7 C. E. Walston and C. P. Felix, "A Method of Programming Measurement and Estimation," *IBM System Journal*, No. 1, 1977, p. 62.

Table 1. Phase I delivered source lines of code

Subsystem		Lines of code
DCD	Command	16,000
DTM	Telemetry	30,100
DTK	Tracking	12,000
DMC	Monitor	16,000
DTT	Test and Training	2,100
CMF	Communications Monitor and Formatter	17,700
DST	Host	5,000
Total lines of code[a]		98,900

[a]The Standard Operating System is not included in the total lines of code. Size of the Standard Operating System is 16,500 lines of code.

Table 2. Amount of documentation for the Command Subsystem

Document	Number of pages
Project Notebook	154
Software Requirements Document	43
Software Definition Document	123
Software Specifications Document[a]	780
Software Operations Manual[a]	140
Software Test and Transfer Document[a]	250
Anomaly Reports	127
Total Documentation	1617 Pages

[a]Amount of documentation was estimated because there was no formal, published document during the time-span under study.

C-2

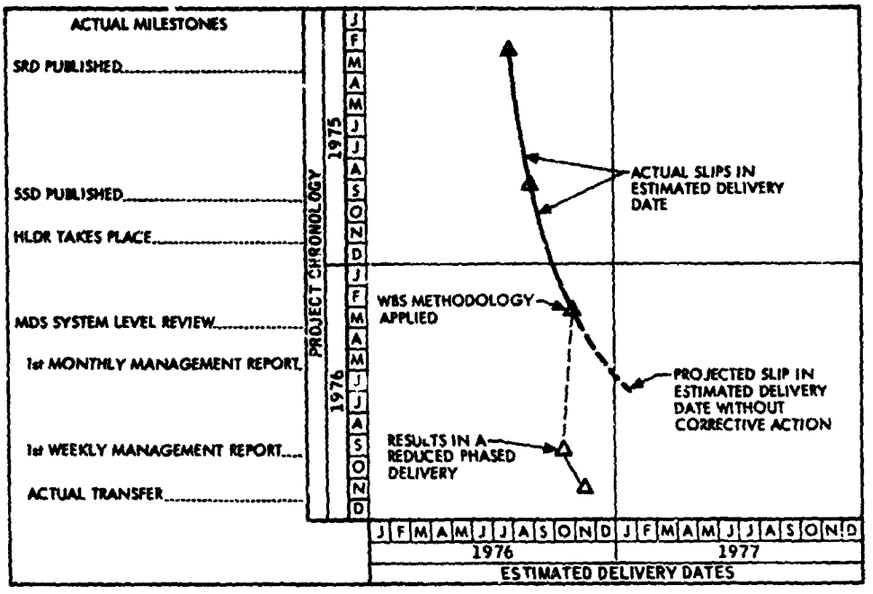

Fig. 1. Successive estimate history of DCD software delivery date

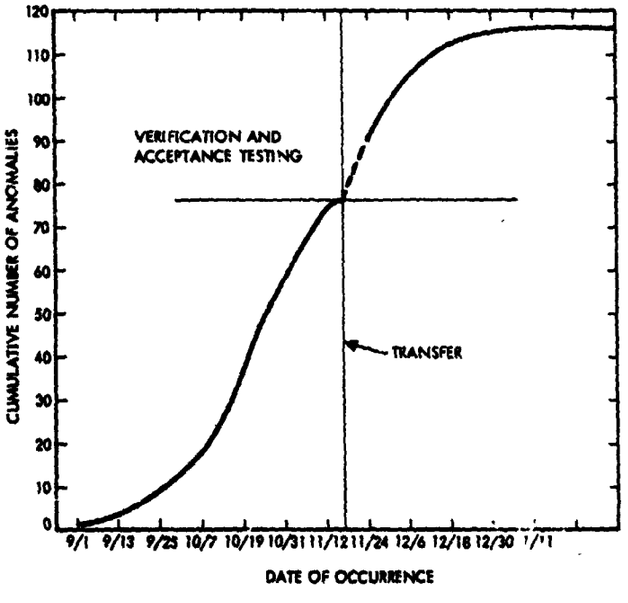

Fig. 2. DCD software anomaly history

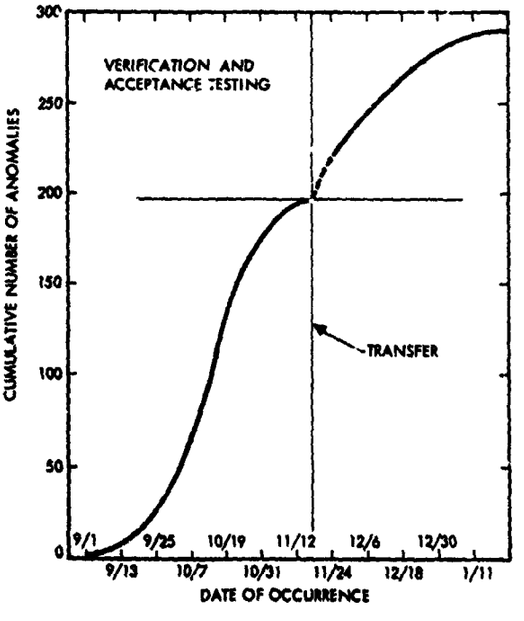

Fig. 3. MDS software anomaly history

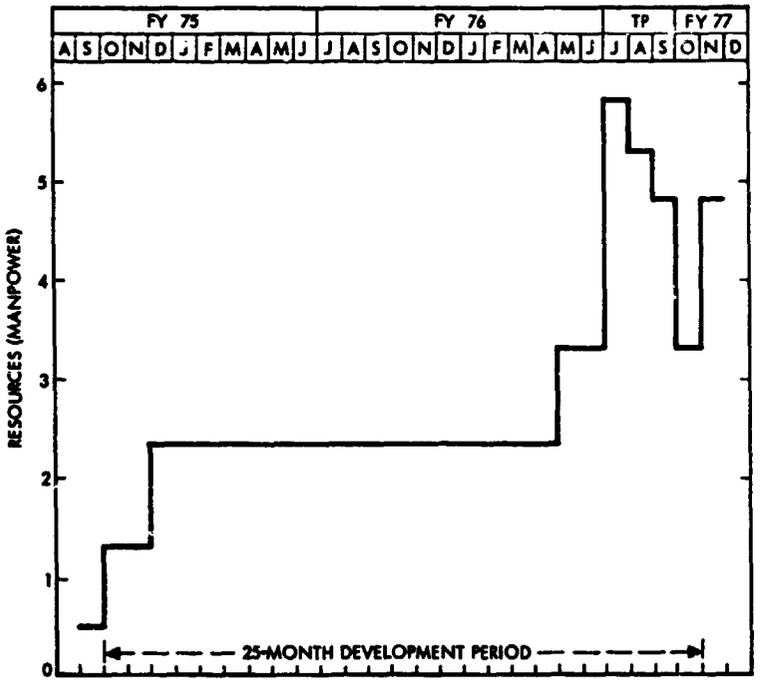

Fig. 4. Command manpower loading profile

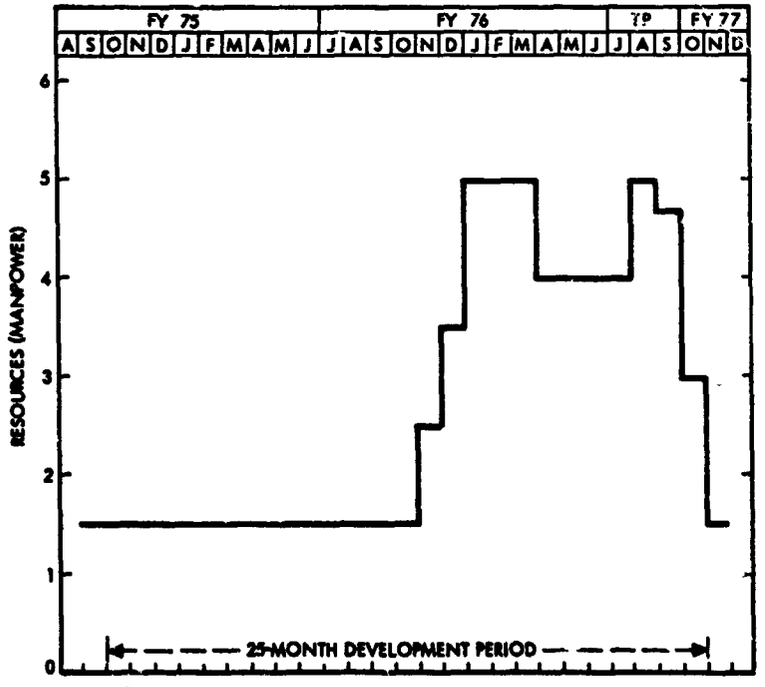

Fig. 5. CMF manpower loading profile

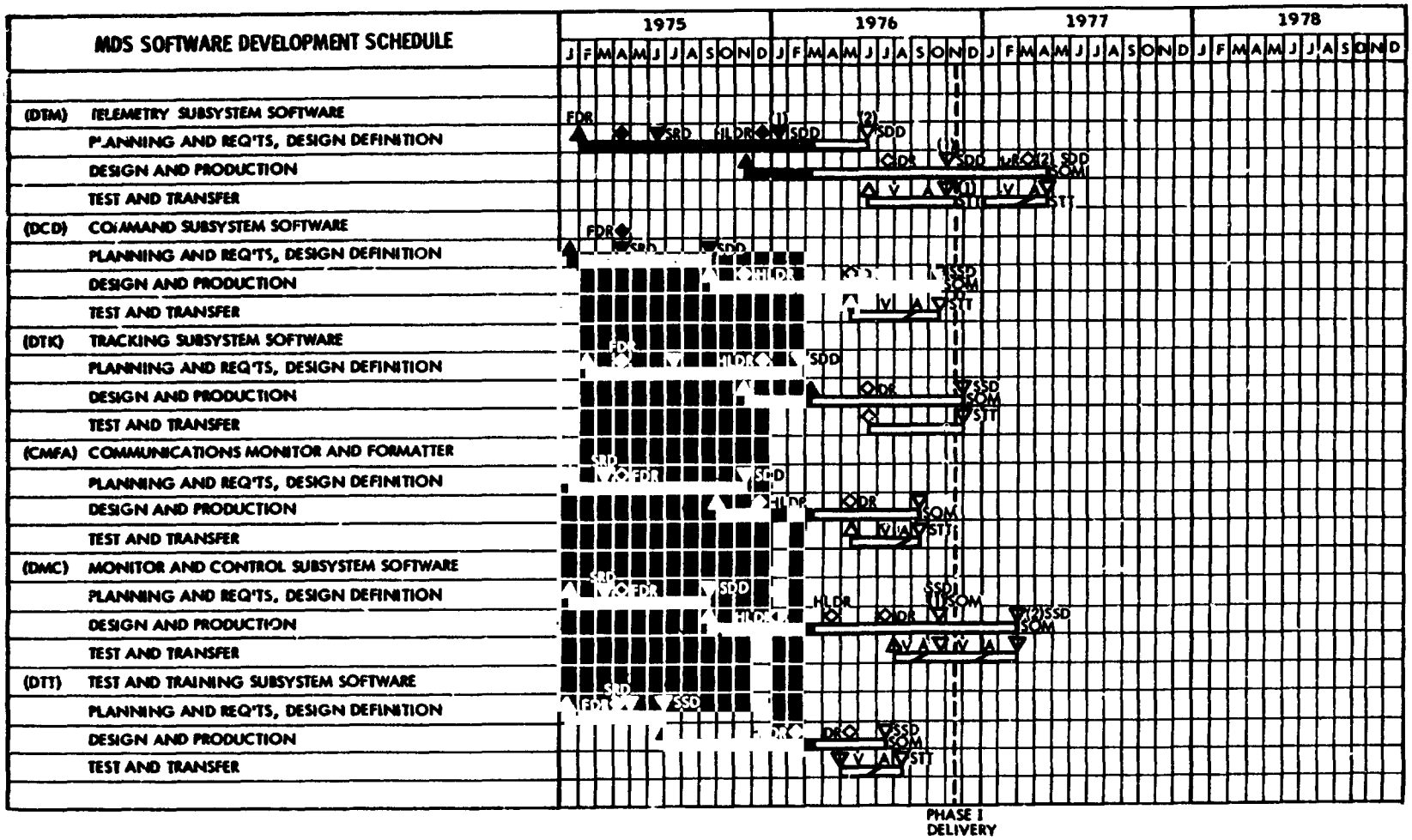

Fig. 6. MDS implementation schedule

D14

N79-16014

MBASIC® Batch Processor Architectural Overview

S. M. Reynolds
DSN Data Systems Section

The MBASIC™ Batch Processor will allow users to run MBASIC™ programs more cheaply. It will be provided as a CONVERT TO BATCH command, usable from the ready mode. It will translate the users program in stages through several levels of intermediate language and optimization. Only the final stage is machine dependent; therefore, only a small effort will be needed to provide a Batch Processor for a new machine.

I. Introduction

Many large, frequently used programs, which are slow and expensive to run, currently exist in the MBASIC™ user community. The MBASIC™ Batch Processor will reduce the time and cost associated with running these programs by providing a compiling facility within the MBASIC™ environment which will allow a user to convert programs to a directly executable form. Direct execution typically reduces program run times by at least an order of magnitude below those of the same programs executed interpretively.

Within the MBASIC™ environment, the user may invoke the Batch Processor through the following commands, prescribed in *Fundamentals of MBASIC™*, Vol. II (JPL, Feb. 19, 1974):

CONVERT ⟨filename⟩ TO BATCH ⟨filename⟩

CONVERT TO BATCH ⟨filename⟩

QUEUE BATCH ⟨filename⟩

RUN ⟨filename⟩

II. MBASIC® Batch Processor Internal View

When called, the MBASIC™ Batch Compiler receives the pseudo-op code (POPCODE) buffer, the Line Reference Table (LRT), and the Name Reference Table (NRT) from the parser. The source code of the program to be compiled is never examined. The output of the compiler is directly executable code for the host machine.

Within the compiler, a completely machine-independent stage is followed by a machine-dependent stage. A major goal of the compiler design is to minimize the proportion of the machine-dependent stage.

The machine-independent stage uses the POPCODE, LRT, and NRT to generate a low-level, machine-independent assembly language called MCODE, which is then translated by the machine-dependent stage into host code (see Fig. 1).

The first step in the translation of POPCODE to MCODE is translation of POPCODE to an equivalent three-address code. This intermediate notation is easier to handle in the ensuing optimization step than the reverse polish notation of POPCODE because reference operands are explicit and are

directly associated with the operation code rather than implicit in pushes onto the stack by previous op codes as in POPCODE.

The second step in translation to MCODE is the optimization of the intermediate code. Because the input and output of this step are intermediate code, expressed in the same internal representation, this step will be delayed in the initial implementation and added later when the surrounding steps have been verified.

The third machine-independent step is translation of the intermediate code to MCODE.

Translation of MCODE to machine-dependent assembly language is performed in two steps: direct translation of MCODE to host code followed by machine-dependent optimization.

For example, the source statement

```
A=B+C
```

becomes

```
PUSH B
PUSH C
ADD
POP A
```

in POPCODE. This is translated into

```
ADD A,B,C
```

in the intermediate code, which is translated into

```
FLOAT TEMP1,B
ADD A,TEMP1,C
```

in MCODE (assuming that B is declared to be an integer), and into

```
LMJ X10,FLOAT
B
TEMP1
L A0,TEMP1
A A0,C
S A0,A
```

Before translation begins, a declaration processing pass through the POPCODE builds a Symbol Definition Table (SDT), which contains type and binding information for each variable explicitly or implicitly declared in the program. The translation process is performed one statement at a time in order to minimize the size of buffers and the use of external mass storage.

III. Pseudo-Op Code

MBASIC™ pseudo-op code is a reverse polish notation for the MBASIC™ virtual stack machine (VSM). One POPCODE string is produced for each MBASIC™ source statement. The MBASIC™ VSM checks for incompatible types at execution time and performs legal type conversions; it can handle arrays and strings as atomic data items; and it handles FOR-NEXT and GOSUB transfers implicitly by using auxiliary stacks. The reflection of these features in POPCODE makes it a relatively high-level language, requiring considerable translation to reach the level of a typical real machine. Even syntactically correct MBASIC™ programs may translate to POPCODE programs which generate runtime errors in the VSM. These errors will be detected and an error message printed during translation rather than at runtime of the compiled program, whenever possible.

IV. Intermediate Language

The Intermediate Language (IL) is a direct mapping of POPCODE to an equivalent non-stack-dependent language. All implicit references to stack data are replaced by explicit references to identifiers, either source defined or temporary identifiers defined by the IL processor.

With one exception, the translation from POPCODE to IL involves a one-to-one mapping of POPCODE statements to corresponding IL statements. The exception is that POPCODE operations whose only result is to push a variable's value onto the data stack do not appear in the IL string, but the identifiers are referenced as IL arguments.

V. POPCODE to IL Translation

The POPCODE to IL translation algorithm is a pseudo-execution of the POPCODE string using an identifier stack instead of a data stack. The popcode string is scanned, and each POPCODE encountered generates the corresponding IL. If values would have been popped from the data stack during execution, identifiers are popped from the identifier stack in the same order. If values would have been pushed onto the stack during execution, temporaries are created and their identifiers pushed onto the identifier stack.

VI. MCODE

MCODE is a low-level, three-address code for a class of virtual machines with variable storage attributes, such as:

(1) Differing number and type of registers.

(2) Differing mappings from main storage to registers (e.g., byte addressable machines which map several cells into one register and word addressable machines which map one cell into one register).

(3) Differing main storage size.

The MCODE generator for a specific implementation of the Batch Processor will be configured by setting its variable attributes to match the host system as closely as possible.

The MCODE virtual machine recognizes the following data types:

(1) Integer – at least 32 bits precision

(2) Real – host system floating point format

(3) Pointer – at least 16 bits precision

(4) Char – at least 7 bits precision

MCODE machines have a separate address space for each data type and for instruction code, and the unit quantity for pointer type and for any absolute address represents one cell of address space of the type pointed to.

Registers may be defined to accept one or more different data types, e.g., a general purpose register in many machines would be represented in the MCODE machine by a register accepting real, integer, and pointer data.

MCODE contains binary, unary, and nonary operations of the following kinds:

(1) Arithmetic

  (a) Add

  (b) Subtract

  (c) Multiply

  (d) Divide

  (e) Unary minus

(2) Boolean

  (a) And

  (b) Or

  (c) Exclusive or

  (d) Complement

  (e) Conditional jump

  (f) Unconditional jump

Each instruction is defined separately for each type, and all operands must be of matching type. Mixed type operations are possible through use of the following conversion operations:

(1) Integer to real

(2) Real to integer

(3) Integer to char

(4) Char to integer

(5) Pointer to integer

(6) Integer to pointer

Each instruction consists of an operation code and zero to three operands. Each operand contains a register/address flag, a register number or address, a type, and a boolean indirect addressing indicator, which may be true only if the operand specifies a pointer register. For arithmetic and boolean operations, the first operand specifies a destination for the result of the operation, and the two other operands specify the source locations. For unary operations, only one source operand is necessary. Jump instructions have one operand, which may only be a pointer register in the case of an indirect address reference or an address in the case of a direct address reference.

MCODE also contains the following operations on data files:

(1) Open

(2) Close

(3) Remove

(4) Rename

(5) Append

These operations have only one operand, which contains a file name.

The following operations have a file name operand followed by a source or destination operand:

(1) Get char

(2) Put char

VII. IL to MCODE Translation

IL to MCODE translation is an in-line expansion performed in a single scan of the IL sequence. Each IL is expanded into one or more MCODE statements. Code for type checking and type conversions for legal mixed type operations is generated during this process. Error messages for illegal types are

generated during type checking. The IL arguments generated are selected on the basis of the best known source for a value at compiled code execution time, i.e., a value known to be in both register and main storage will be represented by the register.

VIII. MCODE to Host Assembly Language Translation

In most cases, the host code will be its standard assembly language. MCODE to host code translation is a machine-dependent process; however, in most cases it can be performed in one scan of the MCODE string with one or more host code statements generated for each MCODE statement. This is possible because MCODE is generated for a virtual machine having storage characteristics similar to those of the real machine.

IX. Machine-Independent Optimization

The machine-independent optimization step is transparent (except in efficiency) to the rest of the MIDB processor because its input and output have the same representation. Optimization will concentrate on expressions and assignment statements. Many statistical studies of actual source code and the possible optimizations have been made, and all show these to be the most effective optimizations in terms of actual reduction of the size and execution time of typical object code. The selected optimizations are:

(1) Subexpressions appearing more than once are calculated once and saved in a temporary variable; instances of the common subexpression are replaced by a reference to the temporary variable.

(2) Subexpressions involving only constants are calculated at compile time.

(3) Multiple assignments to the same variable are recognized and replaced by the last assignment only.

X. Machine-Dependent Optimization

Machine-dependent optimization is also a transparent process (except for efficiency). Some possibilities common to most machines, but still machine-dependent, are the following:

(1) Chains of branches are replaced by a single branch instruction.

(2) Unreachable code is deleted.

(3) Common code groups preceding a collecting node are recognized, and the node is moved to precede the first instance of the common group. The other instance is deleted.

(4) Common code groups heading all branches of a program fork are condensed as in (3), above.

Other completely machine-dependent optimizations might involve such things as invoking auto increment mode in place of explicit pointer arithmetic or recognizing LOAD-STORE groups and replacing them with direct memory to memory moves.

XI. Summary

The MBASIC™ Batch Processor is a language translator designed to operate in the MBASIC™ environment. It will provide a facility with which MBASIC™ programs which have been debugged in the interpretive mode may be translated into a directly executable form and stored or executed from the MBASIC™ environment.

The Processor is to be designed and implemented in both machine-independent and machine-dependent sections. The architecture is planned so that optimization processes are transparent to the rest of the system (except for efficiency) and need not be included in the first design-implementation cycle.

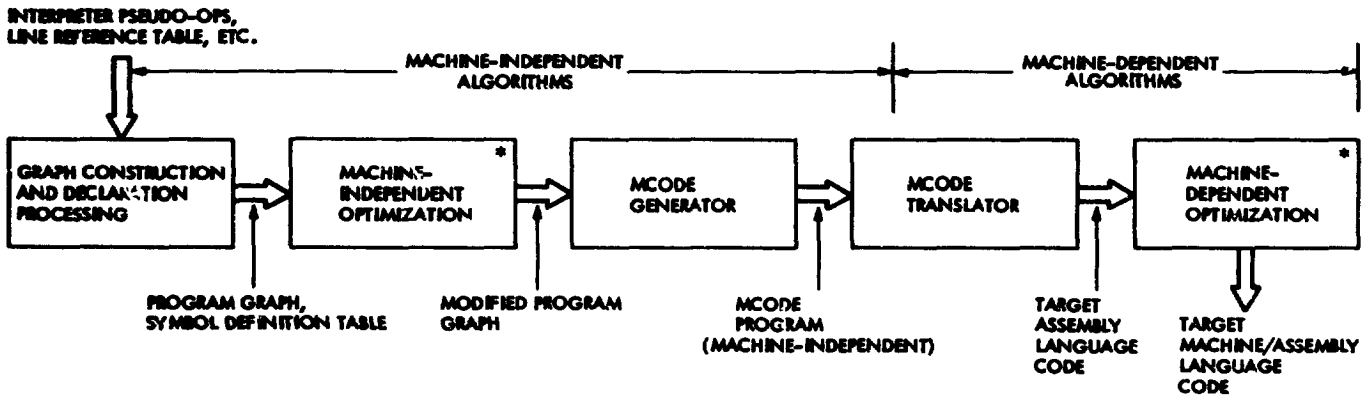

* OPTIMIZATION OPTIONAL

MCODE CHARACTERISTICS:

MACHINE-INDEPENDENT LANGUAGE
LOW-LEVEL LANGUAGE WITH SIMPLE TRANSLATOR
TRANSLATOR IS A REQUIRED PART OF COMPILER
LANGUAGE IS THUS UNDER DSN CHANGE CONTROL
MODULES CODED IN MCODE ARE PORTABLE ONCE MCODE TRANSLATOR IS INSTALLED
REIMPLEMENTATION REQUIRES ONLY TRANSLATOR AND FINAL OPTIMIZER BE REIMPLEMENTED

Fig. 1. MBASIC® Batch Compiler

D15

N79-16015

GCF HSD Error Control

C.-K. Hung
DSN Data Systems Section

A selective repeat Automatic Repeat Request (ARQ) system has been implemented under software control in the GCF Error Detection and Correction (EDC) assembly at JPL and the Comm Monitor and Formatter (CMF) assembly at the DSSs. The CMF and EDC significantly improved real-time data quality and significantly reduced the post-pass time required for replay of blocks originally received in error. Since the Remote Mission Operation Centers (RMOCs) do not provide compatible error correction equipment, error correction will not be used on the RMOC-JPL HSD circuits. The real-time error correction capability will correct error burst or outage of two (2) loop-times or less for each DSS-JPL HSD circuit.

I. Introduction

The Ground Communications Facility (GCF) High Speed Data (HSD) Subsystem consists of the GCF Assemblies (Ref. 5) used to switch, transmit, record, process, distribute, test, and monitor digital data. The detailed functional capabilities of the GCF HSD subsystem for the Mark III period are illustrated in Fig. 1. The HSD circuits for interchange of data between the DSS/RMOC and JPL are impressed with serial bit streams at a continuous line bit rate of 7200 bits/sec in a 1200-bit block size. The blocks are either data blocks or filler blocks. Filler blocks are inserted when the user data load is insufficient to maintain contiguous data blocks on line.

A selective repeat Automatic Repeat Request (ARQ) system (Ref. 6, 9, 10, 11) in which only the particular block received in error is retransmitted has been implemented under software control in the GCF Error Detection and Correction (EDC) minicomputers at the Central Communications Terminal (CCT) at JPL and the Comm Monitor and Formatter (CMF) minicomputers at the DSSs. (These minicomputers, a major portion of GCF High Speed Data subsystem, are shown in Fig. 2.) The CMF and EDC minicomputers, working together, significantly improved real-time data quality and significantly reduced the post-pass time required for replay of blocks originally received in error. The real-time error correction system corrects error burst or outage of two (2) loop-times[1] or less.

Error correction requires that both ends of the HSD line be equipped with error correction capabilities. Error correction will not be used on the RMOC-GCF CCT HSD circuits as the RMOCs do not provide compatible error correction equipment.

[1] A loop-time is a time between a block transmitted and the block acknowledgement received.

II. GCF Error Control Algorithm

In describing the GCF Error Control Algorithm (Ref. 1, 2, 3, 4, 7, 8), only one direction of transmission/reception will be discussed. The reverse direction is identical though independent. A retransmission schematic diagram (Fig. 3) is given to aid in understanding the error control algorithm. The following buffers are needed for the retransmission scheme implemented:

(1) Acknowledgement Queue (A-Queue)

This queue is a first-in/first-out queue which contains data blocks that have been transmitted over the HSD line and are awaiting acknowledgement. As soon as an acknowledgement indicates that a block has been received error-free at the other end, that block is dropped from the A-Queue. Thus, at any time, no more than a loop-time of blocks are stored in the A-Queue (see Table 1, DSS-JPL Loop-Time blocks). The top-entry of the A-Queue is called the A-candidate. It is the next block to be acknowledged or to be retransmitted if the block is not positively acknowledged. For each acknowledgement received, the A-Queue pushes up thus creating the next A-candidate.

(2) Transmit Queue (T-Queue)

This is the data buffer which holds the incoming data blocks until they are called for transmission over the HSD line.

(3) Delivery Queue (D-Queue)

This queue stores all error-free HSD blocks received during retransmission until all prior blocks have been successfully retransmitted. The data blocks are delivered in order. When error correction is inhibited in the far-end, the data blocks are delivered in first-in/first-out sequence.

The error detection encoding and decoding under software control may use either a 22-bit or 33-bit error polynomial. Error correction works only with the 22-bit error code. Each block has two 8-bit fields reserved for GCF error correction use. One field (bits 9-16, word 73) contains the GCF serial number of the block. The other field (bits 1-8, word 74) contains the serial number of the just-received block which is being acknowledged as error-free. These two numbers are termed the GCF serial number and the GCF acknowledgement number respectively. Since the GCF serial number of a HSD block has 8 bits, GCF serial numbers are selected from the set: 0,1,2,·····,255. The term "in GCF sequence" means that a block is serialized in sequence with the previous transmission using the set: 1,2,·····,255,1,2,·····,255,····. The zero value is skipped since it is used for filler blocks. Data blocks transmitted in the error correction mode will carry the non-zero GCF serial numbers. Data blocks transmitted in the error correction inhibited mode will have no GCF serial number (i.e., zero). Whether or not a data block carries a GCF serial number depends on whether or not the transmit end is in error correction mode. Whether a data or filler block carries a GCF acknowledgement number depends on whether a data block with a non-zero GCF serial number was just received. Filler blocks normally will not be serialized but may carry acknowledgement numbers. Each data block that is not acknowledged (i.e., is in error) will be corrected up to N times (normally, N=2). No delay in data flow is introduced when the data string is error-free, but delay is introduced when error correction by retransmission occurs.

The GCF error control algorithm is incorporated into the receive and transmit functions of the CMF and EDC programs. The following is the logic of the error control algorithm.

A. Receive Steps

(1) Accept a high speed data or filler block from HSD line. A normal sequence of interrupts occurs within the time of receipt of a block as predicted by the line rate (6 blocks/sec).

(2) Decode. A block may be received in error in two ways:

(a) Decoding error – Transfer of a complete block, but the 22-bit error polynomial does not correlate with the data in the block.

(b) Missing block – A normal sequence of interrupts does not occur within the time of receipt of a block as predicted by the line rate. The time slot (166.66 msec in 7.2K bits/sec line rate, 6 blocks/sec) corresponding to this missing block is treated the same as a block in error.

(3) Save GCF serial number and acknowledgement number.

(4) If near-end is in error correction mode, go to 5; otherwise skip to 6.

(5) If the acknowledgement number matches the A-candidate (in A-Queue) serial number (indicating that the block was received error-free at the distant end), then the A-candidate is deleted from the A-Queue and retransmission is not required. If the numbers do not match, retransmission is needed.

(6) If the far-end is in error correction mode and the block is received in error, then discard this block and go to 9; otherwise go to 7.[2]

(7) Test block type.

(a) Discard filler block.

(b) Data block with GCF serial number (non-zero) – consider far-end in error correction mode and deliver block to D-Queue for ordered delivery to user.

(c) Data blocks without GCF serial numbers (zero) – consider error correction inhibited at far-end, deliver blocks to D-Queue for first-in/first-out delivery to user.

(8) Delivery to the user (D-Queue Management). The D-Queue is managed by a timer. This queue holds all received data blocks. After processing in the error correction mode (far-end), the blocks are delivered in GCF serial number sequence (the same order in which the blocks were originally transmitted). With error correction inhibited, the data is delivered in a first-in/first-out sequence.

(9) End of receive task.

B. Transmit Steps

(1) If near-end is in error correction mode, go to 2; otherwise skip to 3.

(2) If retransmission is required (from receive task, step 5), the A-candidate is processed in the following way:

(a) If the A-candidate is a data block (GCF serial number is non-zero) and if this A-candidate has been retransmitted N times, then delete the A-candidate and go to 3; otherwise, retransmit the A-candidate and go to 5.

(b) If the A-candidate is a filler block (GCF serial number is zero), delete the A-candidate and go to 3.

(3) If the T-Queue is not empty, select the top-entry from T-Queue for transmission; otherwise select a filler block for transmission.

(4) If the near-end is in the error correction mode, insert a GCF serial number if a data block is being transmitted; otherwise, insert zeros in the serial number slots.

(5) Insert the serial number from the last received block (from receive task, step 3) as the GCF acknowledgement number.

(6) Encode in 22-bit error code.

(7) Transmit this block to HSD line and store this block in the A-Queue if near-end is in error correction mode.

(8) End of transmit task.

In the GCF error control algorithm, the transmit task is driven by the receive task. That is, each received block induces an output block containing its acknowledgement.

The GCF error control algorithm results in four (4) possible operational modes for each DSS-JPL HSD circuit:

(1) No error correction in either direction (DSS/RMOC ↔GCF CCT).

(2) Inbound error correction only (DSS→GCF CCT).

(3) Outbound error correction only (DSS←GCF CCT).

(4) Error correction both directions (DSS↔GCF CCT).

III. GCF Error Control Implementation

The physical configuration and major components of the GCF HSD Subsystem in the Mark III Era is illustrated in Fig 2. The GCF error control algorithm has been implemented in the CMF and EDC software. Key aspects of the implementation are:

(1) The software has been designed and implemented in accordance with DSN software methodology standards (top-down implementation, structured programming principles, etc.).

(2) The implementation effort was organized into a work breakdown structure, which was then used to monitor progress.

(3) Initial inter-computer protocols (data flow) and timing analysis were completed very early in the software development.

(4) Software testing was accomplished in a hardware environment which closely matched that of the final operational configuration.

[2] In case of 7, either (1) far-end is in error correction inhibit mode, or (2) far-end is in error correction mode and the block is received error-free.

After the conclusion of acceptance tests of the DSS CMF in September 1977 and GCF CCT EDC and HSW software in November 1977, the GCF HSD subsystem for the Mark III period became operable and useable to support DSN missions. As of July 1978, all Voyager testing, ATRS recalls, and Manual DODR replay were used by the GCF HSD error correction capabilities. On September 15, 1978, Voyager commenced use of error correction on a routine basis.

The performance of the GCF HSD error control will be described in a subsequent issue of the DSN Progress Report.

References

1. Adeyemi, O. H., "A New Feedback Protocol for the Ground Communications Facility" in the Deep Space Network Progress Report 42-28, pp. 49-56, Jet Propulsion Laboratory, Pasadena, California, December 15, 1976.
2. Adeyemi, O. H., "Error Control in GCF: An Information-Theoretic Model for Error Analysis and Coding", Technical Memorandum 33-699, Jet Propulsion Laboratory, Pasadena, California, October 15, 1974.
3. Adeyemi, O. H. and McEliece, R. J., "Forward Error Correction for the Ground Communications Facility?" in the Deep Space Network Progress Report 42-22, pp. 114-117, Jet Propulsion Laboratory, Pasadena, California. August 15, 1974.
4. Desens, R. E., "GCF Computer Note", unpublished data, Jet Propulsion Laboratory, Pasadena, California, January 28, 1976 (JPL internal document).
5. Evans, R. H., "DSN Ground Communications Facility" in the Deep Space Network Progress Report 42-43, pp. 9-17, Jet Propulsion Laboratory, Pasadena, California, November and December 1977.
6. Gatfield, A. G., "ARQ Error Control on the Satellite Channel" in Conf. Rec., Int. Conf. Comm., 1974, pp. 22B-1 – 22B-5.
7. McClure, J. P., "Basic Algorithm for Retransmission Error Correction", Interoffice Memorandum, October 1972 (JPL internal document).
8. McClure, J. P., "High Speed Data Outage Distribution" in JPL Technical Report 32-1526, Volume XIX.
9. Sastry, A. R. K., "Improving Automatic Repeat - Request (ARQ) Performance on Satellite Channels under High Error Rate Conditions", I.E.E.E. Transactions on Communications, April 1975.
10. Sastry, A. R. K., "Performance of Hybrid Error control Schemes on Satellite Channels", I.E.E.E. Transactions on Communications, Volume Com-23, No. 7, July 1975.
11. Sindhu, Pradeep S., "Retransmission Error Control with Memory", I.E.E.E. Transactions on Communications, Volume Com-25, No. 5, May 1977.

Table 1. DSS-JPL loop time blocks

DSS-JPL	Loop-time blocks
DSS44-JPL	10
DSS62-JPL	13
DSS63-JPL	13
DSS42-JPL	11
DSS43-JPL	11
DSS14-JPL	8

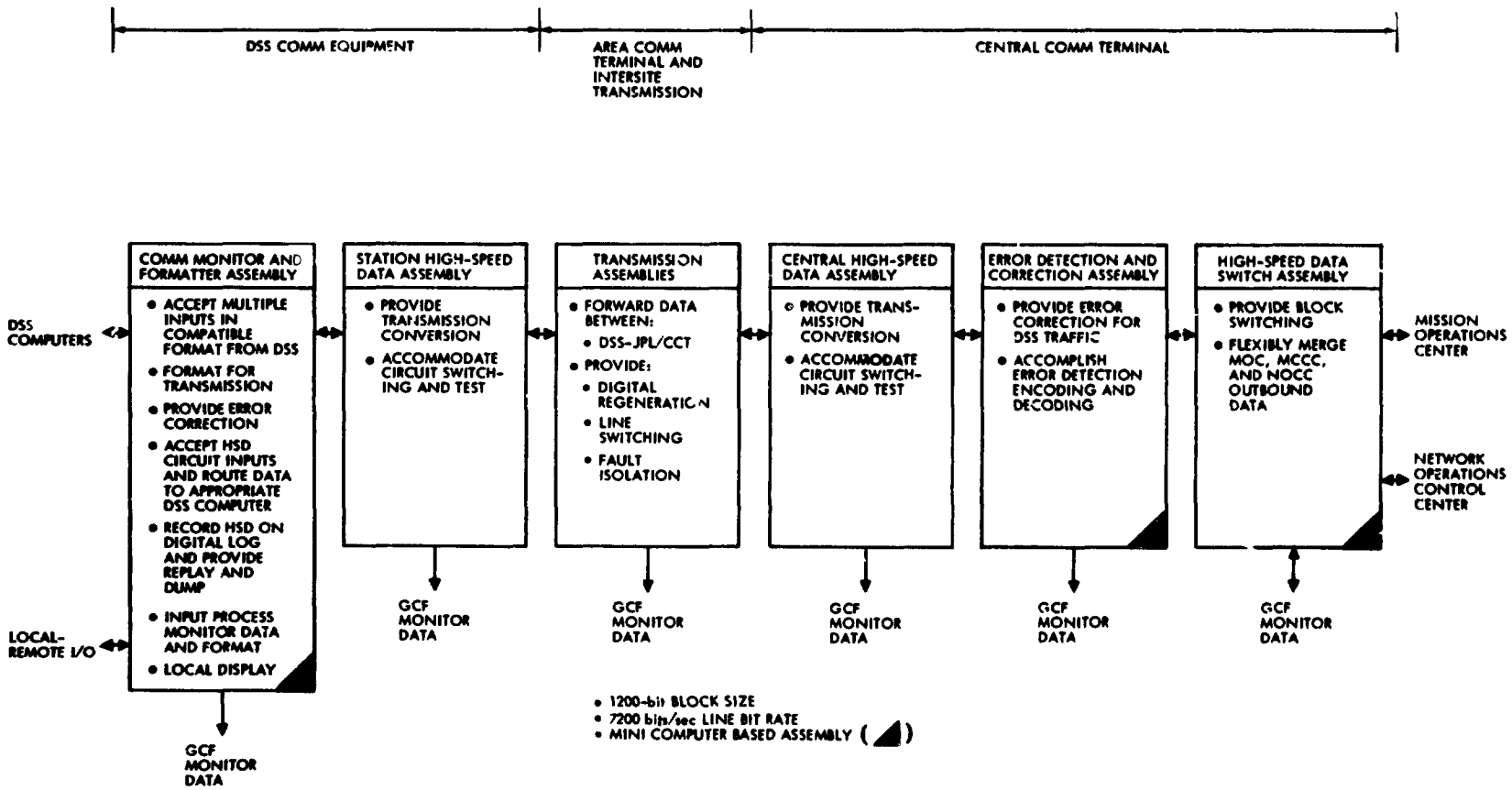

Fig. 1. GCF high-speed data subsystem functional capabilities

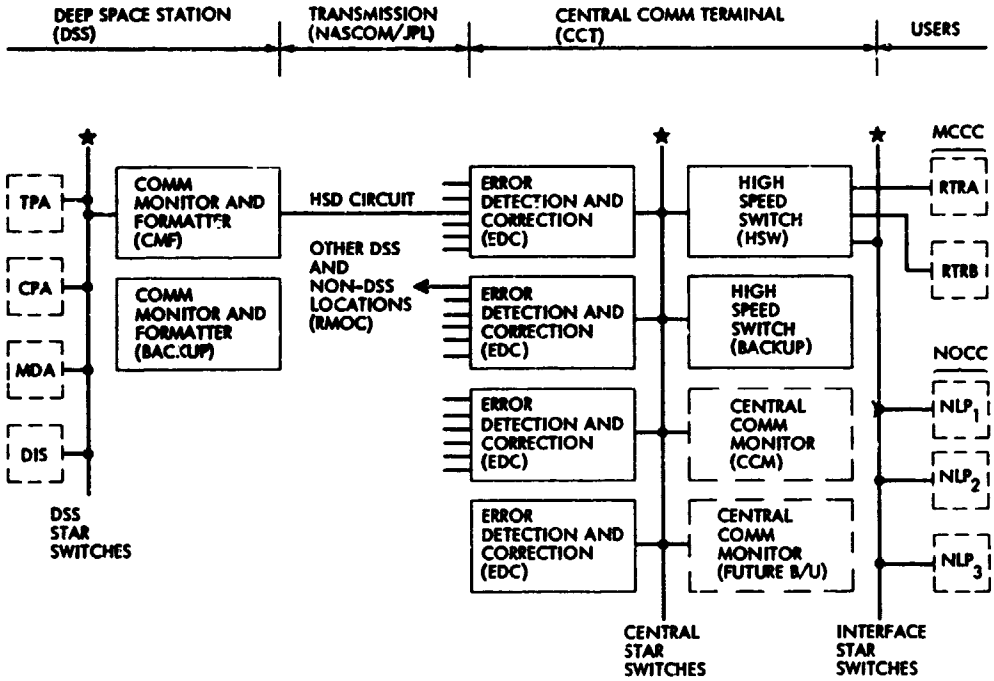

Fig. 2. Mark III-77 high-speed data subsystem configuration

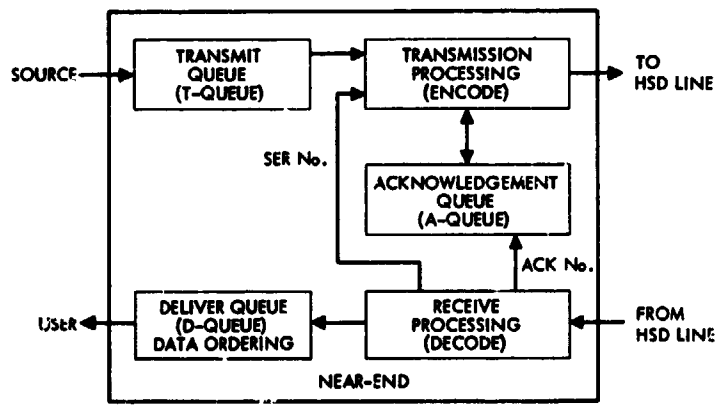

Fig. 3. Retransmission schematic diagram

D16

N79-16016

Tracking Error of 100-m Antenna due to Wind Gust

M. Massoudi
DSN Engineering Section

A procedure is shown to derive root-mean-square tracking error for an antenna system in response to wind-gust loading. Example calculations are illustrated for the design of a proposed 100-m antenna. The effect of wind-gust correlation is also considered.

I. Introduction

Wind loading is an important factor in the design of many above-ground structures. For large antenna structures in particular it is necessary to make some allowance for possible wind loading. Wind motion may be described as consisting of two parts: a mean motion and a superimposed turbulent fluctuation. Some studies have provided detailed measurements of the time history of wind fluctuations, and techniques of random process theory have been employed to gain insight into the physical processes controlling the turbulent fluctuations. This article defines and calculates the tracking error of a proposed 100-m-diameter antenna due to wind-gust torque as a function of equivalent spring constant.

II. Antenna Tracking Error

Wind-gust torques are analyzed as a random process with zero mean. For a system with torque input T_Z and angular displacement output θ_{rms}, (see Fig. 1), we define

T_Z = mean torque input due to wind, Nm

$S_T(f)$ = input spectral density for dynamic wind load

$Y(jf)$ = system admittance to wind torque

$S_0(f)$ = output spectral density

θ_{rms} = tracking error due to wind torque

j = the imaginary unit

The root-mean square (rms) value of the output is obtained from

$$\theta_{rms} = \left\{ \int_0^\infty S_0(f)\,df \right\}^{1/2} \tag{1}$$

where $S_0(f)$ can be computed by

$$S_0(f) = |Y(jf)|^2 S_T(f) \tag{2}$$

in which

$$Y(jf) = \frac{jf}{K_{eq} f_c \left[\left(j\frac{f}{f_n} \right)^2 + j2\zeta\left(\frac{f}{f_n}\right) + 1 \right] \left[j\left(\frac{f}{f_c}\right) + 1 \right]} \tag{3}$$

K_{eq} = series combination of structural stiffness and servo drive stiffness

f_c = servo position loop bandwidth, Hz

f_n = natural frequency of the structure, Hz

ζ = damping ratio, relative to critical damping

f = excitation frequency, Hz

To define the spectral density of the dynamic load, the spectrum of the velocity fluctuations is first required. The velocity spectral density used in this report was obtained by Davenport (Ref. 1), giving the spectrum in the form

$$S_V(f) = \frac{4K U_1^2 X^2}{f(1+X^2)^{4/3}} \tag{4}$$

in which

$S_V(f)$ = velocity spectral density (one-sided)

U_1 = steady speed of wind at reference height of 10 meters, m/s

K = surface drag coefficient for the local terrain

$X = 1200 f/U_1$

To relate the load spectrum to the velocity spectrum, the relation given by Vellozzi and Cohen (Ref. 2) is used, giving the gust-load spectrum in the form:

$$S_T(f) = \frac{4T_z^2}{V_z^2} S_V(f) \tag{5}$$

in which T_Z and V_Z are the steady load and mean wind speed at height Z (meters).

Since the wind gusts are not likely to act simultaneously over the full height of structure, a correlation function (Ref. 2), $C^2(f)$, will be introduced in Eq. (5), which is therefore rewritten as

$$S_T(f) = \frac{4T_Z^2}{V_Z^2} S_V(f) C^2(f) \tag{6}$$

in which

$$C^2(f) = \left\{\frac{1}{\xi} - \frac{1}{2\xi^2}(1-e^{-2\xi})\right\} \times \left\{\frac{1}{\gamma} - \frac{1}{2\gamma^2}(1-e^{-2\gamma})\right\} \times \left\{\frac{1}{\mu} - \frac{1}{2\mu^2}(1-e^{-2\mu})\right\} \tag{7}$$

where

$$\xi = \frac{3.85 f\Delta X}{U}, \gamma = \frac{11.5 f\Delta Y}{U}, \mu = \frac{3.85 f\Delta Z}{U} \tag{8}$$

and

$$U = \frac{U_1}{(1+\alpha)} \left(\frac{h}{10}\right)^{\alpha} \tag{9}$$

in which ΔX, ΔY, and ΔZ = the alongwind, crosswind, and vertical distances over which the correlation is being taken, h is the height of structure, and α is the exponent in the assumed power low-speed profile of the wind vs height of the structure relationship given by

$$U_1 = V_Z \left(\frac{10}{Z}\right)^{\alpha} \tag{10}$$

A. Calculations

To develop Eq. (4) specifically for the case at hand, the following parameters are used:

$\alpha = 0.1405$
$K = 0.005$ } for Goldstone site (Ref. 3)
$Z = 48$ m

then from Eq. (10),

$$U_1 = V_Z \left(\frac{10}{48}\right)^{0.1405} \text{ or } U_1 = 0.80\, V_Z$$

with these relationships, the specific representation of Eq. (4) becomes

$$S_V(f) = \frac{28800 f}{(1+X^2)^{4/3}}$$

For example, with $V_Z = 4.47$ m/s,

$$U_1 = 0.80\,(4.47) = 3.58 \text{ m/s}$$

Thus

$$X = 1200\frac{f}{3.58} = 335.57f$$

and the gust velocity spectrum is given by

$$S_V(f) = \frac{28800f}{(1 + 112608f^2)^{4/3}}$$

Figure 2 shows wind velocity spectral density curves for a family of values of mean speeds, V_Z. Table 1 gives the spectral density equations derived to plot the curves. The tabulated values of f_{max} and $S_V(f_{max})$ indicate the frequency at which the spectra peak and the associated magnitude, respectively.

B. Derivation of the Wind Torque

Loading data derived from existing antenna wind tunnel tests was applied to an analytical model of the 100-m antenna. The antenna orientation shown in Fig. 3 results in the maximum wind torque on the antenna dish, at a speed of 31.29 m/s (70 mph) the result was

$$T_Z = 5.347 \times 10^7 \text{ Nm at } 31.29 \text{ m/s}$$

$$(3.951 \times 10^7 \text{ lb-ft at 70 mph})$$

C. Calculation of Wind Torque for Different Speeds

To calculate wind torque for different speeds of wind, the following formula expresses the relationship that torque is proportional to the square of wind speed, e.g.,

$$T = \left(\frac{V}{V_{ref}}\right)^2 T_{ref} \qquad (11)$$

where T_{ref} and V_{ref} are reference torque and speed, respectively.

Table 2 shows the results of Eq. (11) applied to several mean speeds using the reference speed and torque from the wind tunnel analysis.

D. Calculation of K_{eq}

The equivalent spring constant is computed by means of the well-known relationship for springs in series

$$\frac{1}{K_{eq}} = \frac{1}{K_{structure}} + \frac{1}{K_{servo}} \qquad (12)$$

From structural and servo system analysis, the following spring constants were derived:

$$K_{structure} = 2.82 \times 10^{10} \frac{\text{Nm}}{\text{rad}}$$

$$K_{servo} = 6.78 \times 10^{10} \frac{\text{Nm}}{\text{rad}}$$

substituting these values in Eq. (12) provides

$$K_{eq} = 1.99 \times 10^{10} \frac{\text{Nm}}{\text{rad}}$$

E. Calculation of the Tracking Error

The digital computer was used to integrate Eq. (1) numerically and calculate θ_{rms}. Example results are listed as follows:

Case 1: $f_c = 0.20$ Hz, $f_n = 1.00$ Hz, $\zeta = 0.01$

$C^2(f) = 1$ (100% correlation)

Table 3 shows the constants that can be used to compute the tracking error for Case 1. The tracking error is obtained by dividing the constant by K_{eq}. The results of Case 1 are plotted in Fig. 4.

Case 2: $f_c = 0.20$ Hz, $f_n = 1.00$ Hz, $\zeta = 0.01$

$C^2(f)$: [$h = 104$ meters, $\Delta X = 50$ meters
$\Delta Y = 50$ meters, $\Delta Z = 104$ meters]

Notes h and ΔZ are the overall height of the antenna at stow position.

Table 4 shows the tracking error constants for Case 2. The results of Case 2 are plotted in Fig. 5.

III. Conclusion

The tracking error of the proposed 100-m-diameter antenna due to wind gust has been defined and calculated. In Case 1, in which wind gust has 100 percent correlation over the antenna structure, the tracking error is about 0.012 deg. at 13.14 m/s (30 mph) compared to 0.00043 deg. of Case 2, which is a more realistic result in terms of wind-gust effects on the antenna.

Of course, in considering the above results, one should bear in mind that a reasonable tolerance margin must be taken into account, and these results merely give some understanding to the design team about the antenna performance with respect to wind gust.

References

1. Davenport, A. G., "The Spectrum of Horizontal Gustiness Near the Ground in High Winds," *Quarterly Journal of the Royal Meteorological Society*, London, Vol. 87, Aug. 1961, pp. 194-211.
2. Velozzi, J., and Cohen, E. "Gust Response Factors", *Journal of the Structural Division, Proceedings of the American Society of Civil Engineers*, F ASCE, June 1968.
3. *Wind Power Prediction Models*, Technical Memorandum 33-802, Jet Propulsion Laboratory, California Institute of Technology, Pasadena, California, November 15, 1976.

Table 1. Family of wind velocity spectral densities

V_Z, m/s	$S_V(f)$, $(m/s)^2/Hz$	f_{max}, Hz	$S_V(f_{max})$, $(m/s)^2/Hz$
4.47	$\frac{28800f}{(1+112608f^2)^{4/3}}$	2.31×10^{-3}	35.52
8.94	$\frac{28800f}{(1+28152f^2)^{4/3}}$	4.62×10^{-3}	71.05
13.41	$\frac{28800f}{(1+12512f^2)^{4/3}}$	6.92×10^{-3}	106.57
17.88	$\frac{28800f}{(1+7038f^2)^{4/3}}$	9.23×10^{-3}	142.10
22.35	$\frac{28800f}{(1+4504f^2)^{4/3}}$	1.15×10^{-2}	177.63
26.82	$\frac{28800f}{(1+3128f^2)^{4/3}}$	1.38×10^{-2}	213.14
35.76	$\frac{28800f}{(1+1759f^2)^{4/3}}$	1.85×10^{-2}	284.23
44.70	$\frac{28800f}{(1+1126f^2)^{4/3}}$	2.31×10^{-2}	355.25
53.64	$\frac{28800f}{(1+782f^2)^{4/3}}$	2.77×10^{-2}	426.29

Table 2. Wind torque for different speeds

V_Z, m/s	T_Z, Nm
4.47	1.09×10^6
8.94	4.37×10^6
13.41	9.84×10^6
17.88	1.75×10^7
22.35	2.73×10^7

Table 3. Case 1 tracking error

V_Z, m/s	θ_{rms} (× K_{eq}), deg
4.47	(1.81×10^7)
8.94	(9.14×10^7)
13.41	(2.36×10^8)
17.88	(4.61×10^8)
22.35	(7.75×10^8)

Table 4. Case 2 tracking error

V_Z, m/s	θ_{rms} (× K_{eq}), deg
4.47	(3.24×10^5)
8.94	(2.56×10^6)
13.41	(8.51×10^6)
17.88	(1.99×10^7)
22.35	(3.83×10^7)

Fig. 1. System block diagram

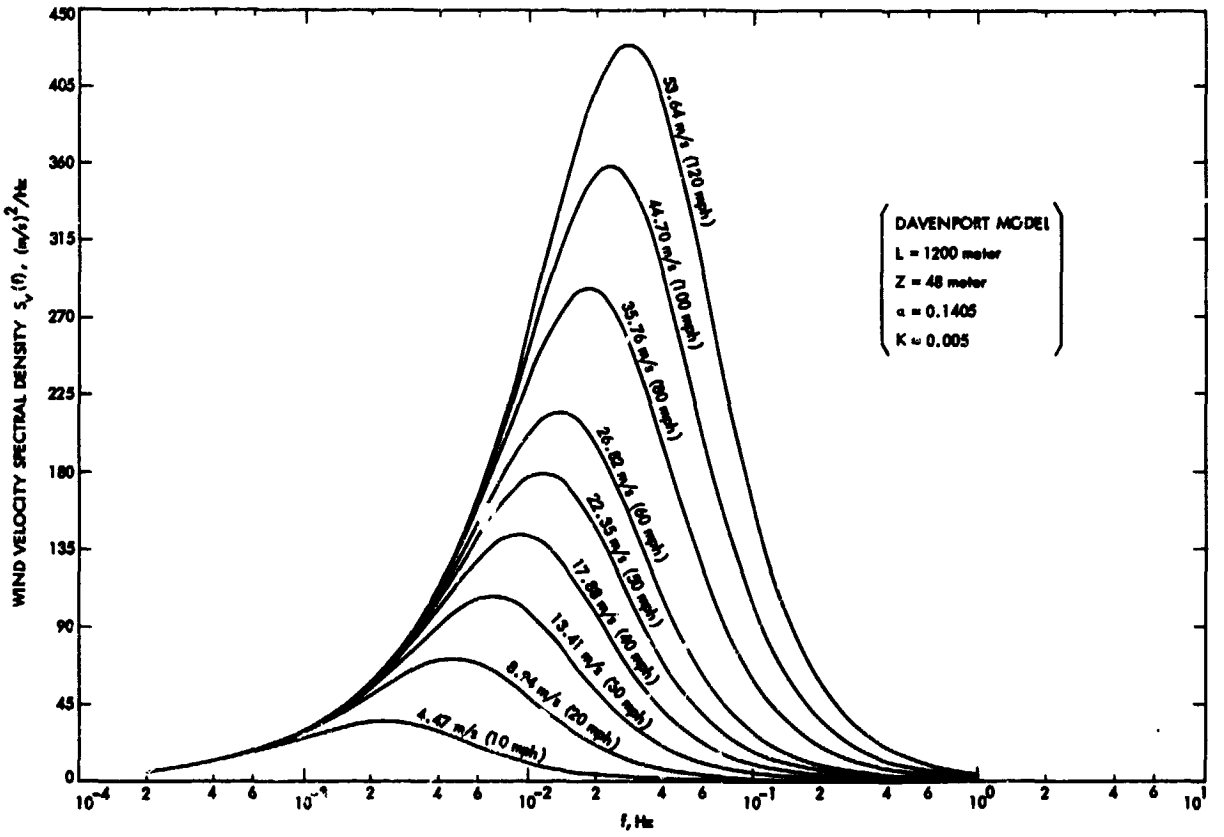

Fig. 2. Wind velocity spectral density

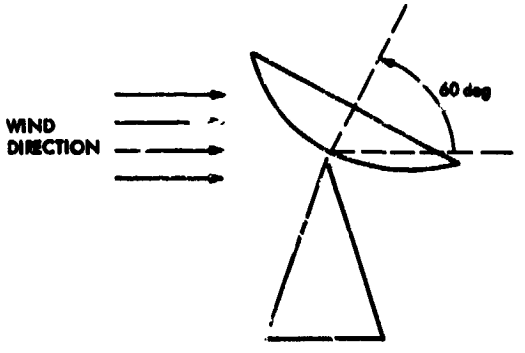

Fig. 3. Antenna orientation diagram

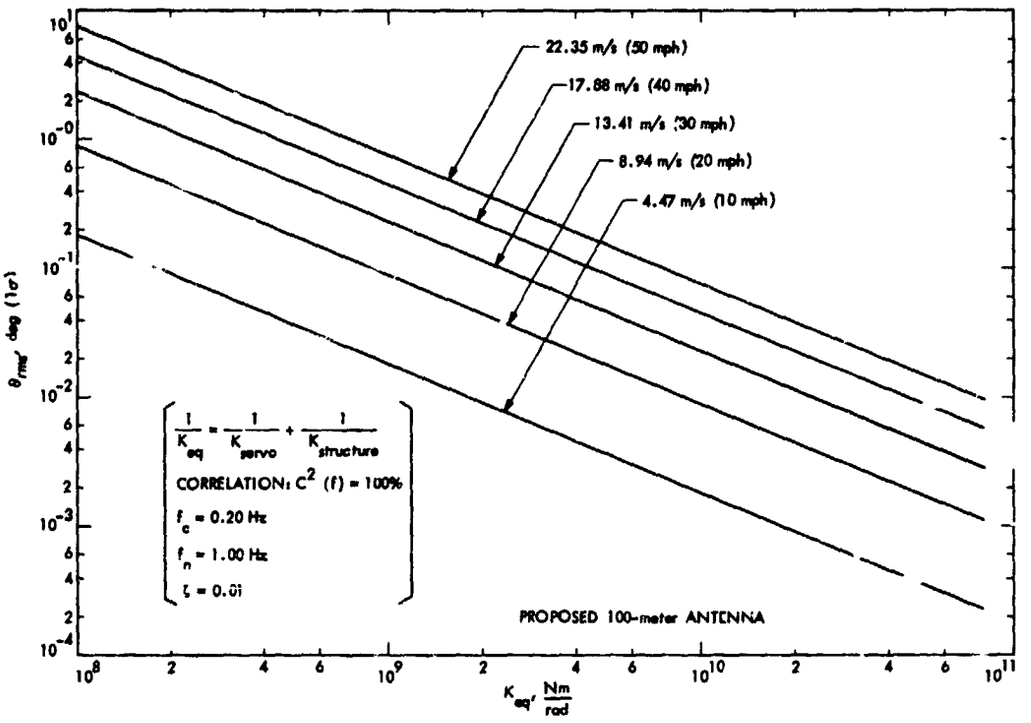

Fig. 4. Tracking error vs equivalent spring constant, Case 1, proposed 100-m antenna

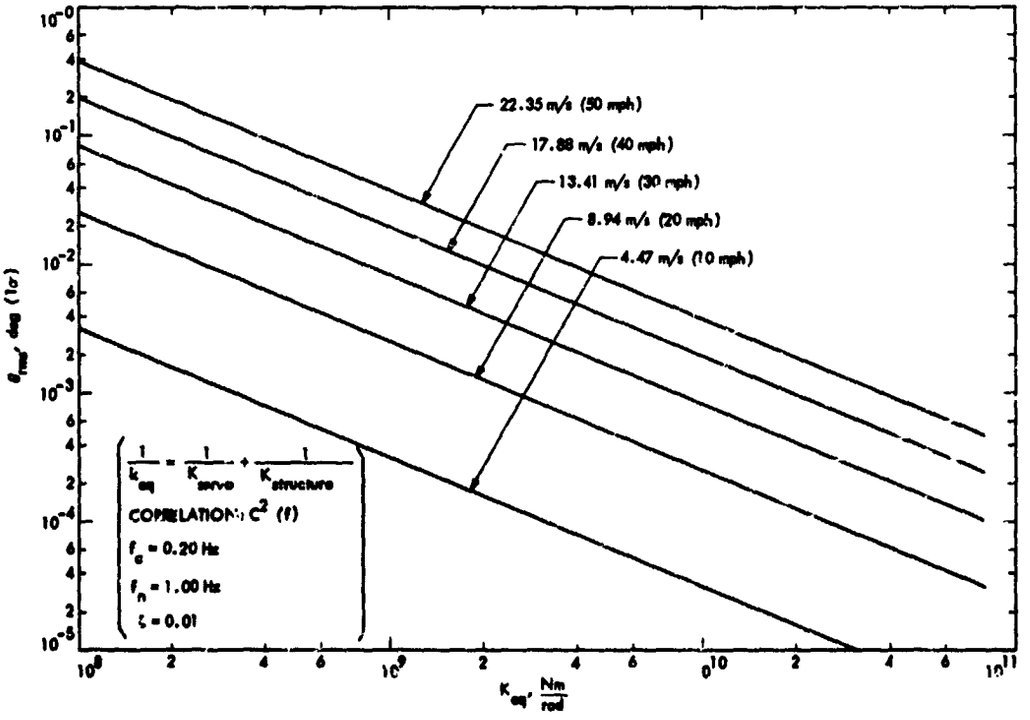

Fig. 5. Tracking error vs equivalent spring constant, Case 2, proposed 100-m antenna

D/7

N79-16017

S-Band Maser Phase Delay Stability Tests

J. M. Ursch, F. Alcazar, J. Galvez, and A. Rius
Madrid Deep Space Station

C. A. Greenhall
TDA Engineering Office

This article summarizes the results of the S-band traveling-wave maser phase delay stability measurements performed at DSS 62. These tests were required for the Pioneer-Venus wind experiment.

I. Introduction

This article summarizes the results of the S-band traveling-wave maser phase delay stability measurements performed at DSS 62. In conjunction with earlier group delay measurements, this article completes the group and phase delay measurements required for the Pioneer-Venus 78 wind experiment.

All tests were performed for the entire S-band maser passband, which includes the 5-MHz passband, from 2290 to 2295 MHz, used in the entry probe wind experiment. This experiment requires that the phase delay variation be less than 1 deg over a 2-MHz passband (2291 to 2293 MHz).

II. Test Configuration

All the tests were performed on the declination (dec) room maser. Figure 1 shows the physical location of test equipment. As can be seen, most of this was installed in the empty part of receiver rack 9.

Figure 2 is the test configuration schematic. To have a phase delay difference of less than 180 deg between test and reference paths, a delay line was fabricated locally. This consisted of about 38 meters of soft line encapsulated in a plastic box and insulated thermally.

III. Phase Delay Stability Versus Maser Parameters

Phase delay variation over a given frequency band is defined as max $\Delta\phi(f)$ - min $\Delta\phi(f)$, where $\phi(f)$ is the phase delay versus frequency curve, $\Delta\phi(f)$ is the change in $\phi(f)$ due to some internal or environmental change, and the max and min are over all f in the band. Notice that if the $\phi(f)$ curve simply moves parallel to itself, the phase delay variation is zero, since $\Delta\phi(f)$ is constant. If the phases of the signals from all Pioneer-Venus probes are shifted by the same amount, no harm is done because the phases are differenced

Variations of five maser parameters were simulated employing the same method used in the group delay stability measurements (see Table 1).

The expected variations were taken from the technical manuals of the corresponding power supplies and checked

against actual variations for periods of about 24 hours. The scale factor is the ratio between the simulated and the expected parameter variations. This must be taken into account when estimating the expected phase delay stability.

A. Results

Figures 3 through 7 are copies of the actual curves obtained while performing the above tests. Table 2 summarizes the test results.

As shown, two sets of measurements were performed (Figs. 3 through 7 correspond to set No. 2) with the dispersion between both being 1.5 deg. This is more than acceptable taking into account the different factors involved.

The variations were measured for a passband of 40 MHz (2265 to 2305 MHz) as well as for the passband of interest in the probe wind experiment (2290 to 2295 MHz). They should be divided by the corresponding scale factor to obtain the expected variations.

B. Coherence with Group Delay Stability Results

By calculating the group delay stability from the data obtained for phase delay stability and comparing it with the data derived from measuring the group delay stability directly, a reasonable coherency may be obtained between both group and phase delay stability measurements. The relationship between group delay stability and phase delay stability is given by

$$\overline{\Delta\tau} = \frac{1}{2\pi B} |\Delta\phi_1 - \Delta\phi_2|$$

where

$\overline{\Delta\tau}$ = group delay stability from phase delay stability data

B = width of passband

$\Delta\phi_1$ and $\Delta\phi_2$ = phase delay differences in both extremes of the passband, considering their signs

The value of $\overline{\Delta\tau}$ may be derived for all parameter variations and compared with $\Delta\tau$, the group delay stability measured earlier. Figure 8 details the result of this comparison for the 40-MHz passband. It can be seen that the difference is less than 0.28 ns except for bandwidth current, where the difference is less than 1.07 ns.

C. Estimation of Phase Delay Stability Versus Room Temperatures

Due to the heavy tracking load, it was not possible to check the phase delay stability versus dec and control room temperatures. However, based on the coherency of results obtained, it is possible to derive from Eq. 1 the phase delay stability $|\Delta\phi_1 - \Delta\phi_2|$ from the group delay stability $\Delta\tau$ measured earlier. See Table 3.

IV. Stability Versus Antenna Orientation

The appropriate range of antenna movement to simulate the possible earth magnetic field variation (due to DSS 43 antenna position changes) during the entry probe wind experiment was estimated using the earth magnetic field model of Lang (Ref. 1):

$B_r = (2m \cos\theta)/R$ radial component

$B_\theta = (m \sin\theta)/R^3$ local meridian component

$B_\phi = 0$ local parallel component

where

$m = 8.1 \times 10^{25}$ gauss $\times$ cm^3

$R = 6.37 \times 10^8$ cm

θ = 50 deg for DSS 62 and 125 deg for DSS 43

From the above we found that the magnitude of the earth's magnetic field for DSS 62 is 0.47 gauss and its elevation angle is 59 deg. For DSS 43 the magnitude is 0.43 gauss. Therefore, by moving the DSS 62 antenna from the az = 0 deg, el = 59 deg position (HA = 0 deg, dec = 72 deg), where the maser magnetic field is perpendicular to the earth's magnetic field, to az = 180 deg, el = 40 deg (HA = 0 deg, dec = 340 deg), where both magnetic fields are parallel, it is possible to simulate a variation larger than that expected in the PV wind experiment. In addition, it should be noted that the earth's magnetic field at DSS 62 is slightly greater than at DSS 43.

Although during the actual test the antenna could only be moved from HA = 0 deg, dec = 70 deg to HA = 0 deg, dec = 360 deg due to safety reasons (personnel and test equipment in dec room), the above reasoning is still valid.

A. Results

Figure 9 illustrates the stability versus antenna orientation results. The antenna movement sequence was: Zenith (Z) → dec 70 deg → Zenith (Z') → dec 360 deg → Zenith (Z'').

It should be noted that it is quite impossible to tie down all the test equipment and cables so that they do not move during the antenna movement. Because of this, after multiple tests

that proved that for very small equipment and cable movements the phase delay may vary about 5 deg, we conclude that the differences between the curves shown in Fig. 9 for all zenith and dec 70-deg positions may be due to slight movements of the set-up components.

From the above it may be asserted that phase delay stability is better than 25 deg for the entire maser passband, 40 MHz, and better than 5 deg for the 5-MHz passband of interest here.

The reason for the different shape of the curves in Figs. 3 through 7 and the curve in Fig. 9 was a maser klystron change in between.

V. Long-Term Stability

The long-term stability of the maser phase delay was checked during periods of 8 hours. The test configuration was the one detailed in Fig. 2 except for the X-Y plotter. This was replaced by a strip chart recorder HP 7100.

During the warmup period of the test equipment, the phase delay drifted considerably. Moreover, for more than 6 hours after this period, the phase delay drifted continuously at a rate of 2 deg per hour.

To check that the phase delay drift observed during the first hour and a half was due to the test equipment warming up, we performed an additional test in which we replaced the maser by a soft line of the proper length. Under these conditions, all the drift should be due only to the test equipment (cables included). Results showed the same considerable drift during the first hour and a half. For about 6 hours after that, no appreciable drift was observed.

The conclusion of these long-term stability tests is that a phase delay drift of about 2 deg per hour can be expected.

VI. Conclusions

A. General

Considering the scale factors, one may infer from Table 2 that the parametric variation yielding the largest phase delay instability (in the 5-MHz passband) is the liquid HE temperature (vapor pressure gauge). The same result was obtained when measuring the group delay stability. Nevertheless, this phase instability is only about 0.16 deg. The root-sum-square (RSS) of the phase instabilities due to all parametric variations is 0.17 deg.

As far as room temperatures are concerned (Table 3), that of the dec room is the one yielding the highest phase delay instability, about 0.27 deg.

The RSS of all phase instabilities from Tables 2 and 3 is 0.32 deg, and the linear sum is 0.58 deg.

From the antenna movement tests (Table 4) it may be seen that the instability in the 5-MHz passband is better than 5 deg. It should be remembered that the simulated antenna movement represents almost a complete range of interaction between the maser and earth magnetic fields (from perpendicular to parallel position). The actual antenna movement during the 90-minute wind experiment will be 22.5 deg in hour angle. Hence, the change in the angle α between the magnetic fields of the earth and the maser is less than 22.5 deg. Assuming that the phase delay variation V is proportional to the change in cos α we have

$$V < 5 \text{ deg} \left(22.5 \frac{\pi}{180}\right) < 2 \text{ deg}$$

This bound corresponds to a 4-m error in the difference of probe position components over 90 minutes (0.74 deg over 1000 seconds) measured by the Goldstone-Canberra baseline. The requirement is for < 1 deg over 1000 seconds, which is met. In addition, the wind experiment is intended to measure probe *velocities*. Since error Δv in the difference of probe velocity components is proportional to dV/dt, the largest that Δv can get is 4 m/5400 s = 0.00074 m/s, a negligible error. The position error is gradually accumulated over the whole 90-minute period. The same reasoning applies to the long-term drift discussed in Section V.

B. Curve Analysis

When comparing Figs. 3 through 5 with Figs. 6 through 7 it was observed that, while the curves in the first figures were rather parallel throughout the passband, the curves in Figs. 6 and 7 appear to "rotate" (or change slopes) near the DSN bandwidth (2285 to 2305 MHz) around which the maser klystron is tuned. This may be explained by using the Leflang model for the phase-versus-frequency maser characteristic, given in degrees by (Ref. 2)

$$\phi(f) = 6.56 \sum_{i=1}^{2} G_i \frac{2(f - f)/\Delta f_L}{1 + \left[2(f - f_i)/\Delta f_L\right]^2}$$

where G_i and f_i are the gain in dB and the central frequency of the i^{th} section, and Δf_L is the maser material resonance line width.

Assuming $\Delta f_L >> f - f_i$ we have

$$\phi(f) \approx 6.56 \sum_{i=1}^{2} G_i \left[\frac{2(f-f_i)}{\Delta f_L} - \frac{8(f-f_i)^3}{(\Delta f_L)^3} \right]$$

To first approximation,

$$\phi(f) \approx 6.56 \sum_{i=1}^{2} G_i \frac{2(f-f_i)}{\Delta f_L}$$

$$= \frac{13.12}{\Delta f_L}(G_1 + G_2)\left(f - \frac{G_1 f_1 + G_2 f_2}{G_1 + G_2}\right)$$

This expression is a straight line with its slope proportional to $G_1 + G_2$ and the intersection with the frequency axis being the gain-weighted mean of the central frequencies of the two sections. Hence, those parametric variations that mainly affect the f_1 and f_2 position (such as beam and reflector voltages and bandwidth control current) will yield rather parallel curves. On the other hand, those affecting $G_1 + G_2$, such as gain control voltage and cryogenic temperature (vapor pressure gauge), will give curves with different slopes and rotating around a zone determined by the klystron tuning.

As for the shape of curves in Fig. 9, the predominant effect for the dec 360-deg curve is the total gain while for the dec 70-deg curve it is the f_1, f_2 positions.

VII. Instability due to Cross-Head Modulation

During one set of measurements, the cross-head modulation effect appeared for a short period of time and has been reflected in Fig. 10. This instability has the same shape as that observed while measuring the group delay stability. The stability may be estimated at less than 5 deg and may be of some importance, if present. The shape of this curve can also be explained due to the rapid and opposite gain variations caused by the cross-head modulation effect.

References

1. Lang, K. R., *Astrophysical Formulae*, Springer-Verlag, Berlin, 1974.
2. Leflang, J. G., *Maser Development*, JPL Technical Report 32-1526, Vol. 15, pp. 92-95. Jet Propulsion Laboratory, Pasadena, Calif., 1973.

Table 1. Test conditions

Parameter	Simulated variation	Expected variation	Scale factor
Beam voltage	± 5 V	< 0.75 V	13.4
Reflected voltage	± 2 V	< 0.1 V	40
Bandwidth control current	± 1 mA	< 50 A	40
Gain control current	± 3 mA	< 50 A	120
Liquid helium temperature	1.3 N/cm^2 = 2 lb/in^2 (VPG)	0.4 N/cm^2 = 0.58 lb/in^2	3.2

Table 2. Results of parametric study

Parameter	Simulated variation	Measured phase delay variation for a 40-MHz passband, deg		Measured phase delay variation for a 5-MHz passband, deg		Scale factor
		Set 1	Set 2	Set 1	Set 2	
Beam voltage	± 5 V	7	6	< 0.5	0.5	13.4
Reflected voltage	± 2 V	9	8.5	2	0.5	40
Bandwidth control current	± 1 mA	2	2	0.5	1	40
Gain control current	± 3 mA	2	2.5	< 0.5	< 0.5	120
Liquid helium temperature	1.3 N/cm^2 = 2 lb/in^2	5	5	< 0.5	0.5	3.2

Table 3. Estimated phase delay stability versus room temperatures

Parameter	Simulated variation	Expected variation	Peak-to-peak variation of group delay, ns	Estimated phase delay stability, deg	
				B=40 MHz	B=5 MHz
Dec room temperature	1.7°C	1.7°C	0.3	2.1	0.27
Control room temperature	1.7°C	0.6°C	0.2	1.4	0.18

Table 4. Phase delay stability versus antenna orientation

Passband, MHz	Measured phase delay stability, deg
40 MHz (2265-2305 MHz)	Better than 25
5 MHz (2290-2295 MHz)	Better than 5

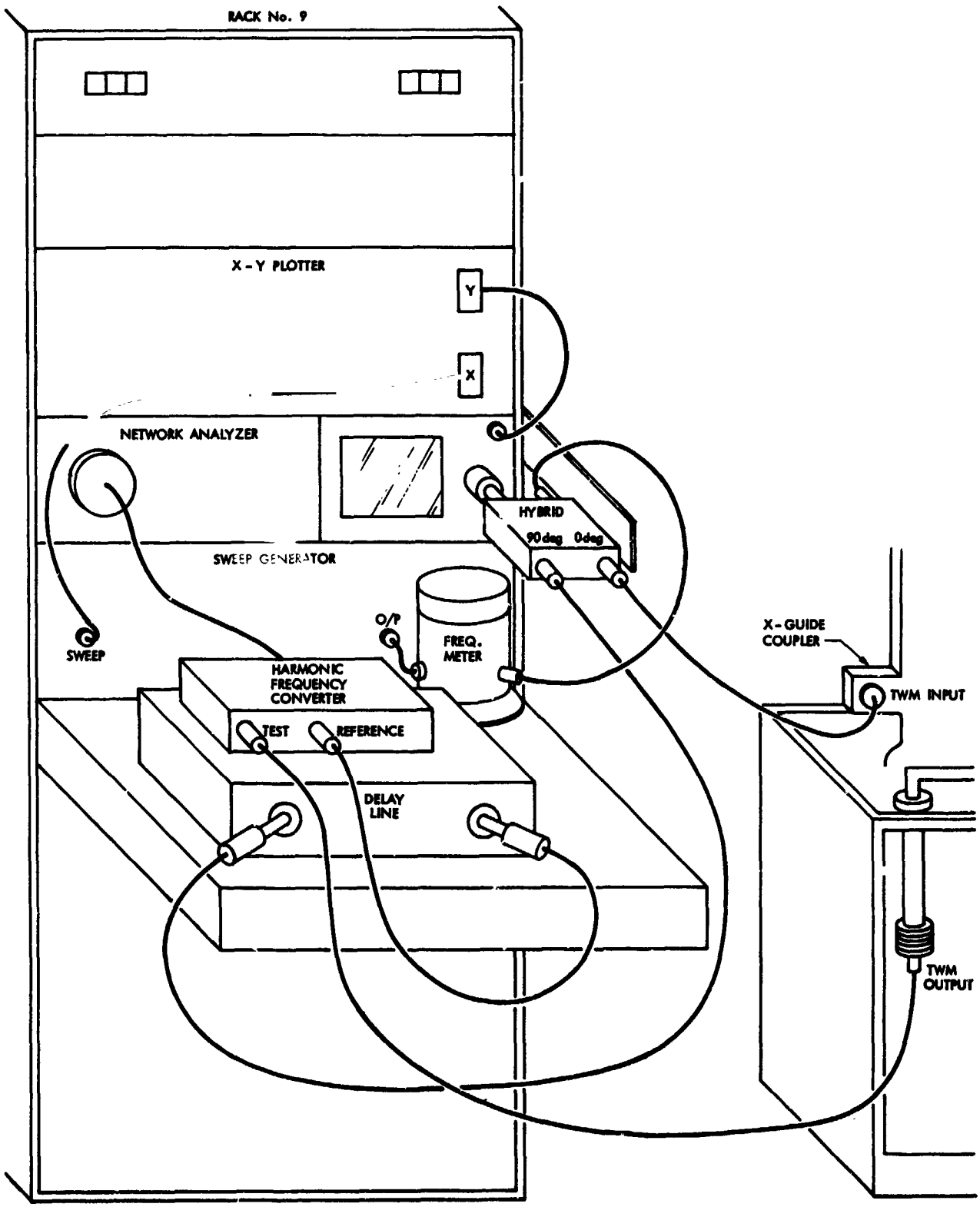

Fig. 1. Test equipment physical location

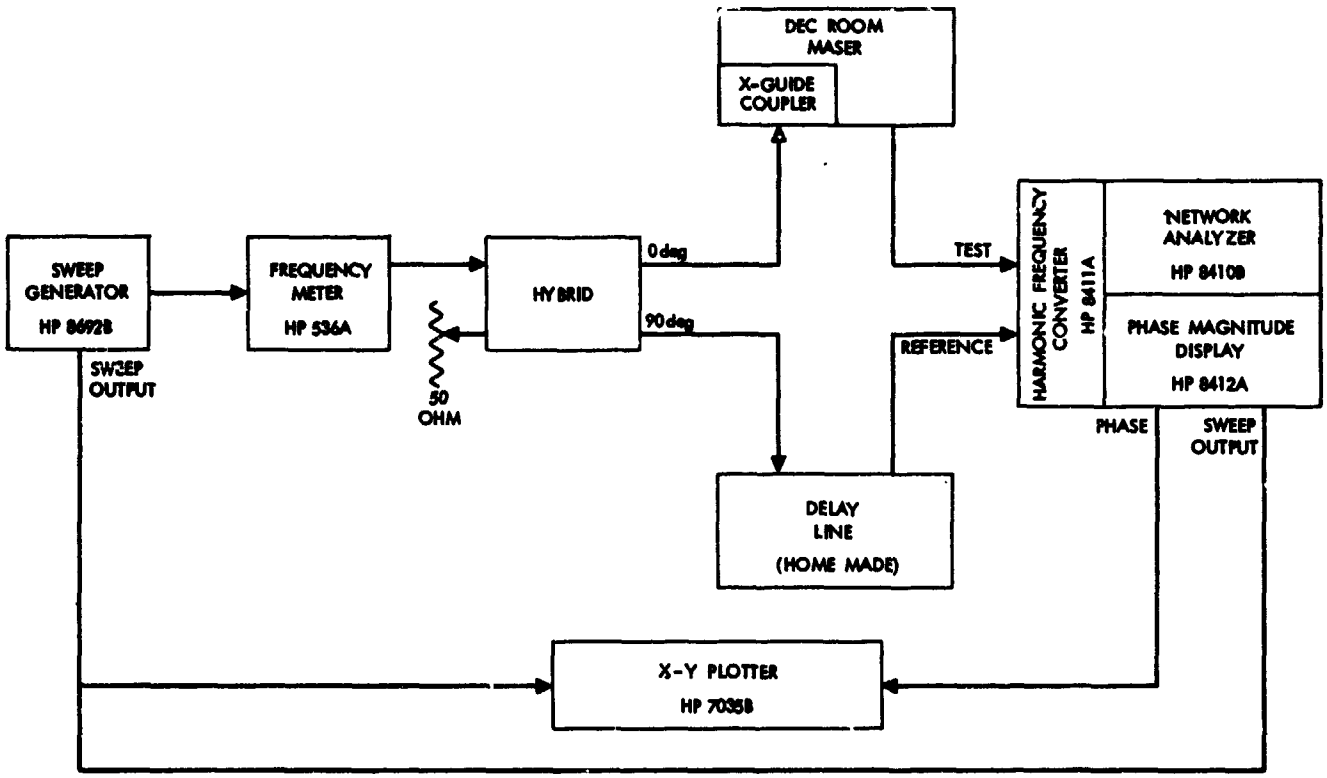

Fig. 2. Test configuration

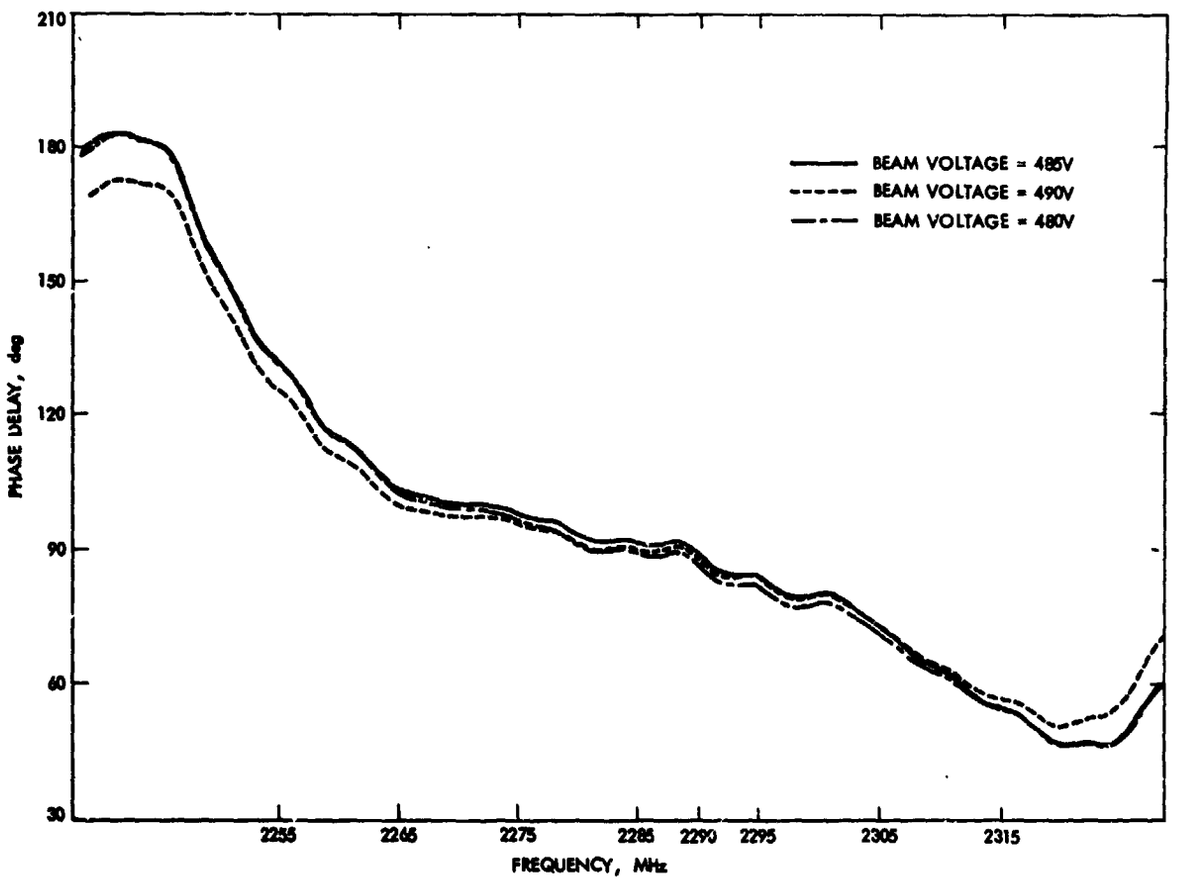

Fig. 3. Phase delay stability vs beam voltage variation

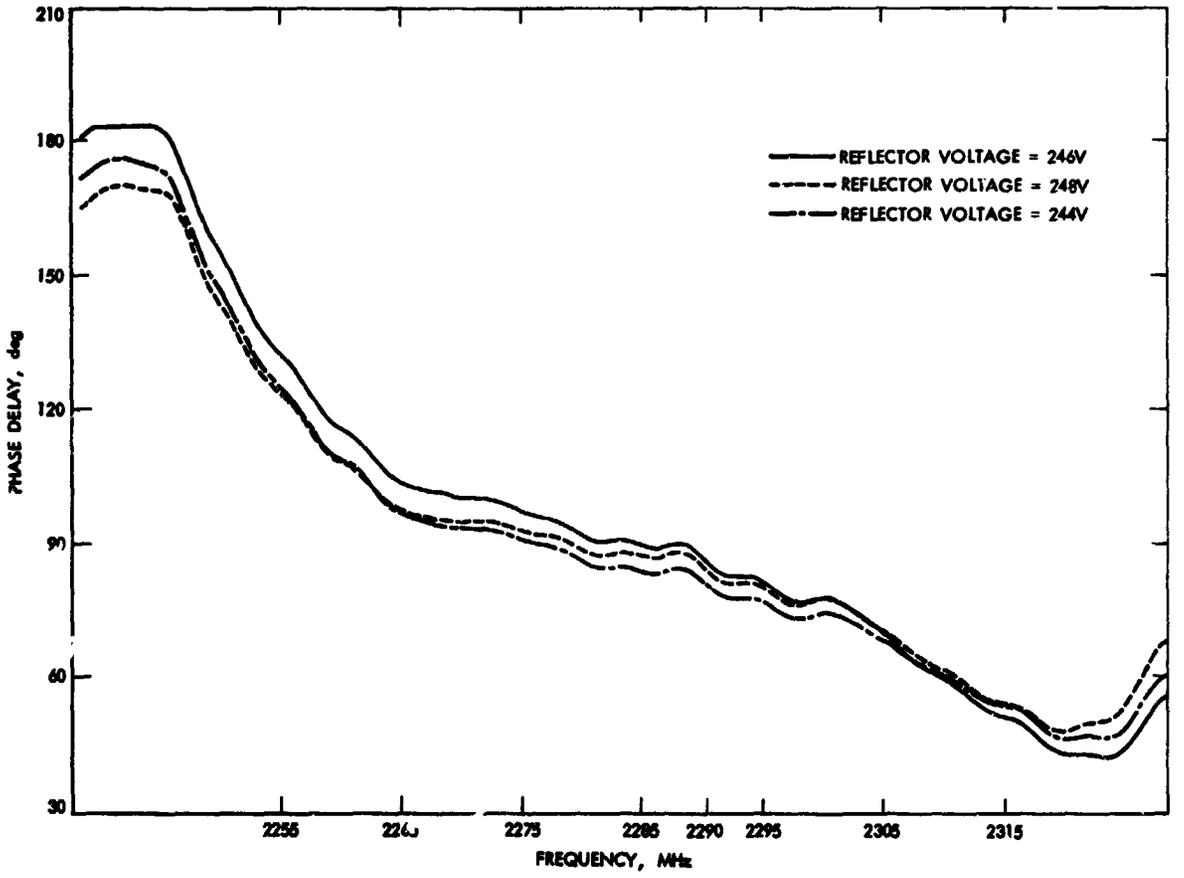

Fig. 4. Phase delay stability vs reflector voltage variation

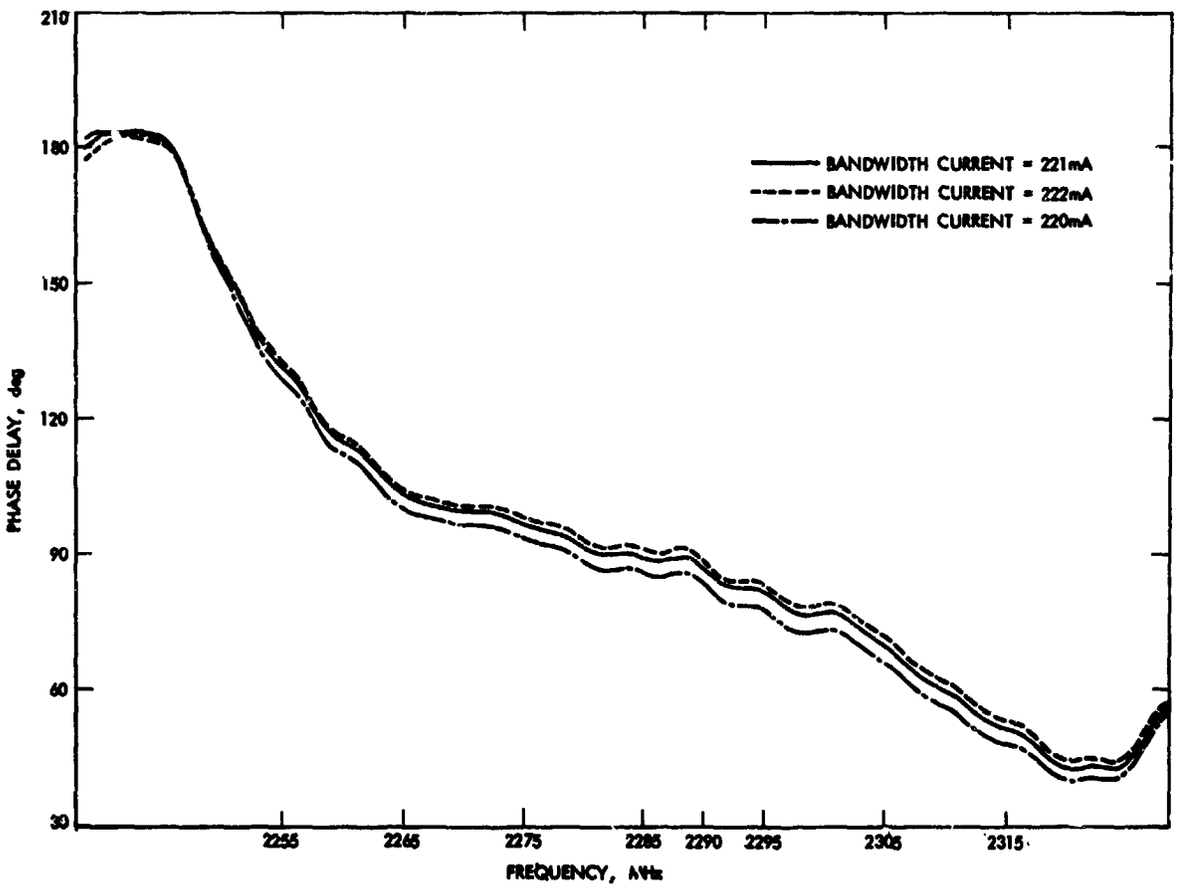

Fig. 5. Phase delay stability vs bandwidth control current variation

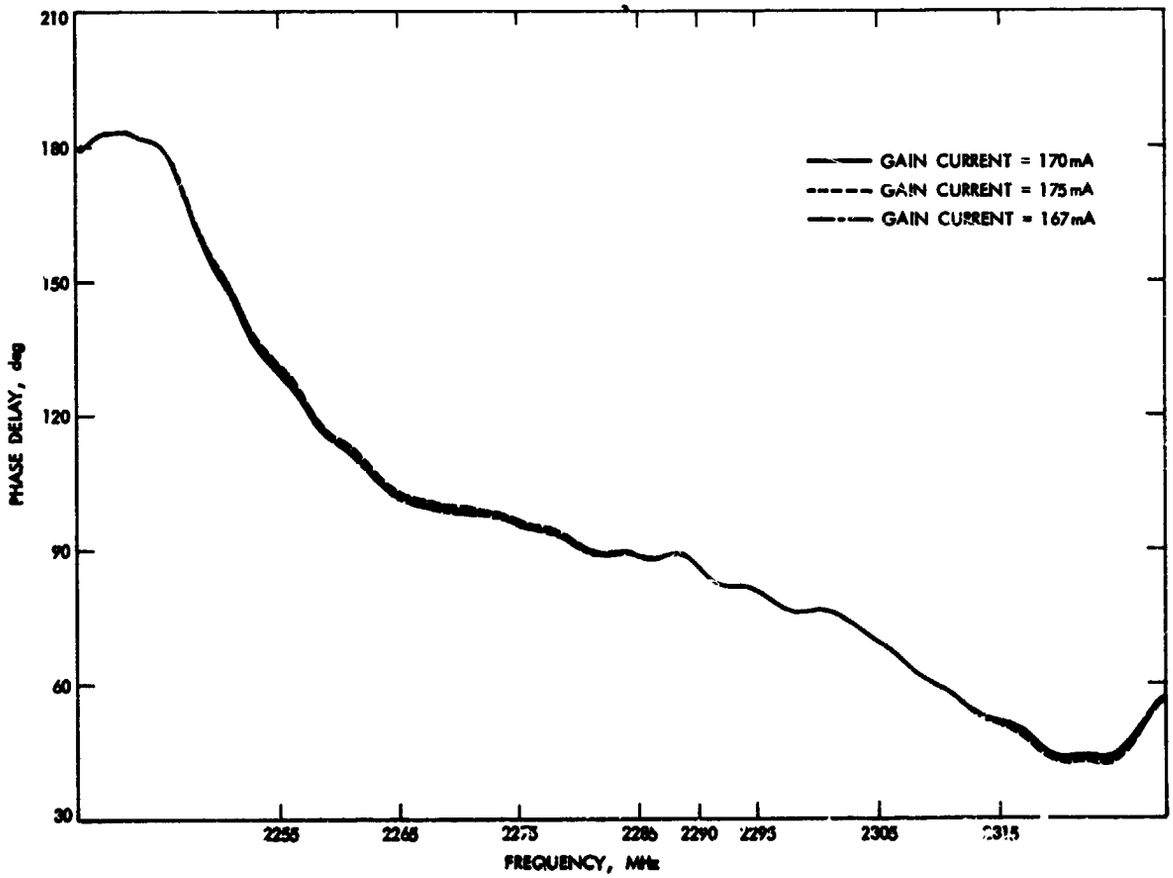

Fig. 6. Phase delay stability vs gain control current variation

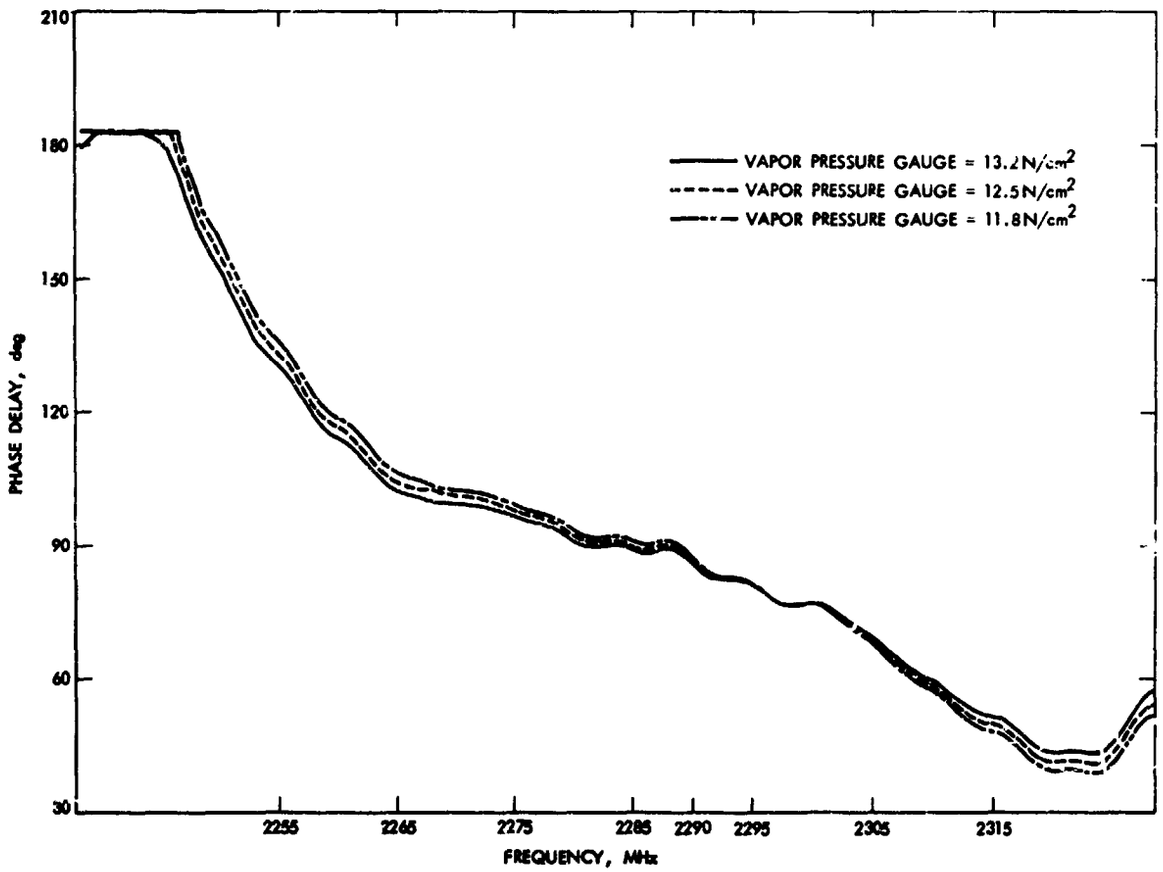

Fig. 7. Phase delay stability vs liquid He temperature

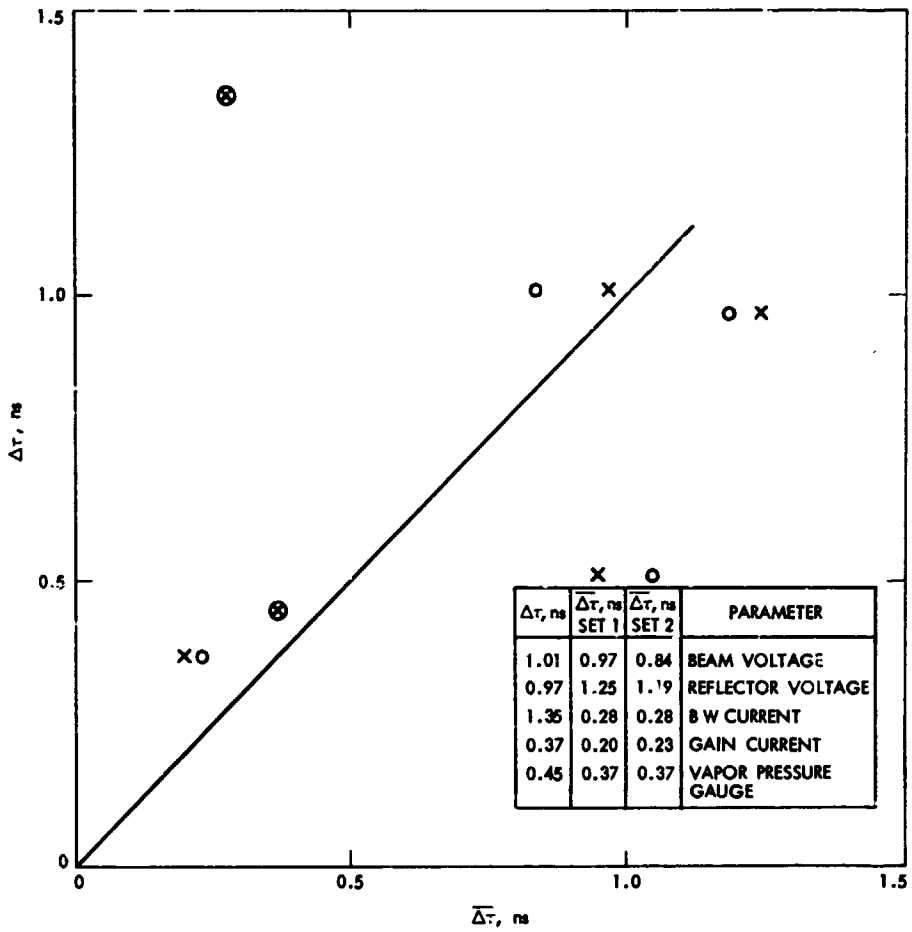

Fig. 8. Coherency of phase and group delay stability

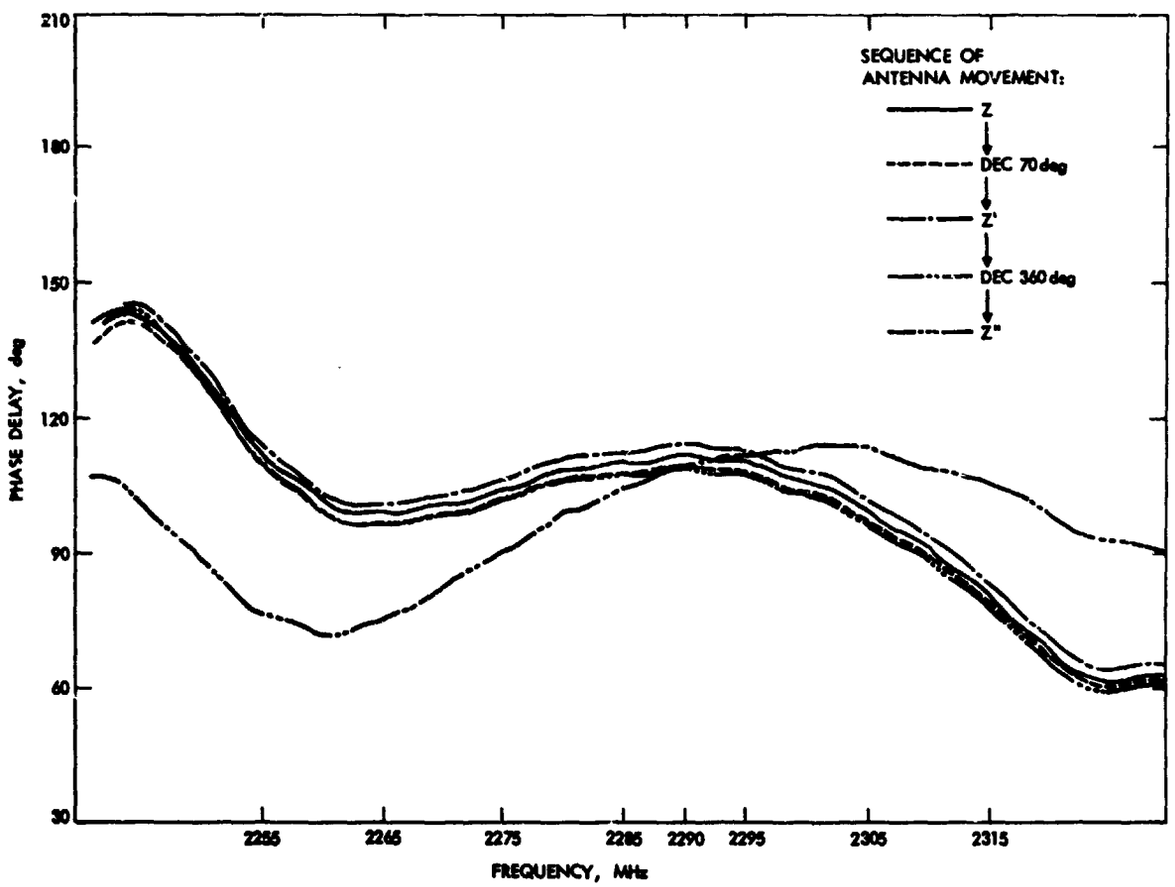

Fig. 9. Phase delay stability vs antenna orientation

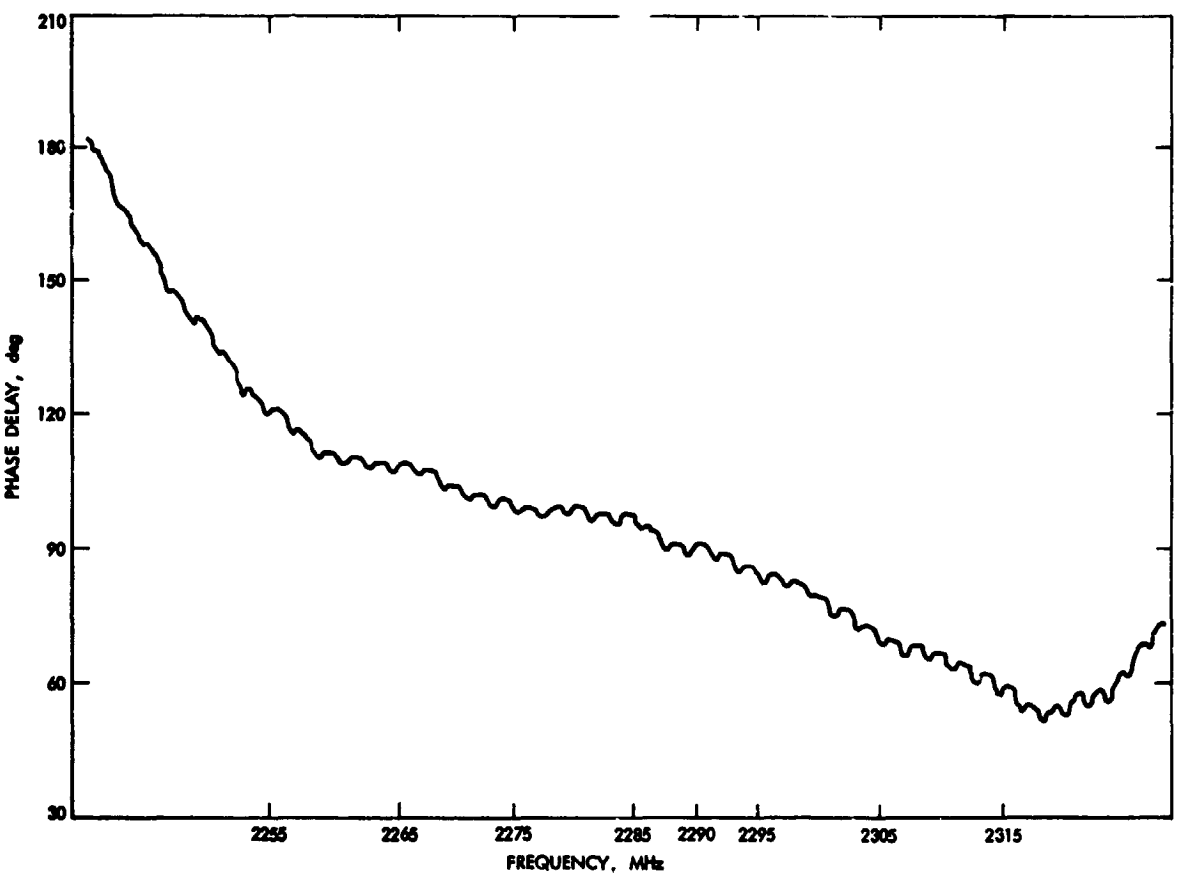

Fig. 10. Cross-head modulation effect on phase delay stability

D18

N79-16018

A Preliminary Model for High-Power Waveguide Arcing and Arc Protection

H. C. Yen
Radio Frequency and Microwave Subsystems Section

This is the first article in a series describing the ongoing effort of the Transmitter Group to upgrade the arc protection subsystems that are, or will be, implemented in the DSN high-power transmitters. This article reviews the status of our present knowledge about waveguide arcs in terms of a simple engineering model and discusses a fairly general arc detection scheme. Areas where further studies are needed are pointed out along with our proposed approaches to the solutions of these problems.

I. Introduction

This is the initial report on one phase of the ongoing effort of the Transmitter Group to upgrade the arc protection subsystems currently used in the DSN high-power transmitters. The ultimate goal of this effort is to develop, with a known margin of safety, an extremely fast and highly reliable arc protection system which can be designed, manufactured and implemented for the eventual automation of these transmitter subsystems.

High-power microwave breakdown invariably results in arcing inside a nitrogen-filled waveguide system (P~1 atm). The breakdown and subsequent arc formation interrupts the normal high-power transmission and causes a very large standing wave to be set up between the microwave source and the arc. Such high-level standing waves can be quite destructive to the components employed in the high-power transmission if their peak power ratings are exceeded. In addition, the accompanying arc once formed was found always moving toward the source at a speed depending on the field level (Refs. 1,2,3). Such high-power arcs can cause new or additional damages through their heating and thermal shocking effects as they propagate through the system. Often the arc damage is of a very severe nature. As an example, if the arc is allowed to travel to reach the output window of a high-power klystron amplifier before the klystron output can be turned off, the arc literally hangs up at the window and destroys it, which usually leads to a costly destruction of the klystron amplifier itself.

Even though precautions can be taken to reduce the chance of microwave breakdown within the designed power rating when assembling the transmission system (Refs. 4, 5), a complete prevention can never be assured. To protect system components against damages in the event of breakdown, protective devices must be employed. Protection is accomplished by removing or reducing the microwave energy that feeds the breakdown within a very short period of time after the breakdown is detected. For a klystron amplifier, this can be the turning off or drastic reduction in the klystron drive. Since the energy level required to sustain an arc is much smaller than that to initiate one, once an arc is initiated, the

klystron output must be well attenuated to completely extinguish the arc.

The arc and the arc plasma cause high reflected power during their formation and propagation (Refs. 1,2,3). A reverse power detector, properly located, is a highly satisfactory device for arc detection. However, the reverse power detector doesn't provide protection against arcs formed between the reverse power detector (directional coupler) and the source – the most damaging kind. For a positive arc protection, other types of devices such as light-sensitive ones have to be used in this region, preferably with one device viewing the klystron output window directly.

In the following, we will concern outselves mainly with the protection of the output window against arc damage, as arcs formed elsewhere can be easily detected by monitoring the reverse power. A simple model showing the energy relationship associated with microwave arcing and a general optical detection scheme is discussed. Due to the complexity of the process and lack of applicable experimental data, only a semiempirical discussion is attempted at the present time. This article will briefly review the status of our present knowledge about microwave arcing inside a high-power waveguide system; at the same time it will also point out the areas where further theoretical and experimental studies are needed as well as our proposed approaches to the solutions of these problems.

II. Arc Model

Radiations emitted by nitrogen arc plasma have been actively studied both experimentally and theoretically (Refs. 6,7). Because of the complexity of the arcing process, a general theoretical treatment is impossible. Often, simplifying assumptions such as local thermodynamical equilibrium, the arc thermal-chemical state, arc parameters (pressure, temperature, current density, radius, symmetry, etc.) and radiation wavelength range have to be made to facilitate the calculations of both line and continuum radiations. Experimentally, the arc plasma has to be stabilized and stationary for data collection. Obviously the applicability of the results from these studies to the case of waveguide arcing during high-power transmission is not without question, because the latter is essentially a time-dependent discharge phenomenon. As shown in these studies, arc plasma radiation depends strongly on the thermal-chemical state of the plasma, which in turn varies considerably with the degree of departure from equilibrium. To make the matter more uncertain, these studies often show some degree of discrepancy among themselves regarding the interpretation of experimental results. Nevertheless, they do provide us an important means to understand arc radiation on a microscopic level. The model given below will be based on macroscopic processes for a first-order characterization of the waveguide arc, however. The reason is that the macroscopic characteristics are only partially understood so far, and a complete knowledge is needed for any meaningful study of the underlying microscopic processes.

According to the law of energy conservation, the energy relationship right before and after the waveguide arcing can be represented by the block diagram in Fig. 1.

Experimentally, the characteristic time for complete arc formation has been found to be of the order of a few microseconds. Conceivably, this time must be a function of the power level. Unfortunately, to our knowledge, this functional dependence has not been systematically examined to date. It turns out that the arc protection also has to be accomplished within approximately the same period of time after initial arcing is detected in order to avoid any real damage (Refs. 1,8). This microsecond response time is one of the important design parameters for an arc detector. The arc shape based on the field profile (TE_{10} mode) would be a cylinder with an approximately elliptical cross section. The actual shape has not been reported previously, probably because of the difficulty of direct visual observation of waveguide arcs. In some experiments where continuous arc tracks were left behind, a spatial periodicity of half guide wavelength along the propagation direction can be seen, with the spatial extent in the cross-sectional plane being modulated. It seems possible to have simultaneous arcings at half guide wavelength apart after the initial arcing if the standing wave field exceeds the breakdown field. This possibility has not, to our knowledge, been explicitly stated or observed in the existing literature.

Once fully formed, the arc plasma becomes a very effective shorting plane despite its limited extension in space, as evidenced by the presence of very little transmitted power and a very large amount of reverse power. Typically, the transmitted power is about 1 percent of the incident power, while the reverse power can range from 50 percent ($P_{inc} \sim 20$ kW) to almost 98 percent ($P_{inc} \sim 1$ MW) of the incident power (Refs. 1,2,8).

The difference between the incident and the reflected plus the transmitted power is the power associated with arcing (energy "absorbed" by the arc). Although not all of this energy is converted into radiation, it is believed that a substantial fraction is. A division of the energy according to the observable macroscopic phenomena is given in Fig. 2. Such division is somewhat simplified and not without ambiguity. It is done here for the purpose of identifying major phenomena which might offer a potential for arc detection. A brief discussion of each category is given as follows:

(1) Sonic wave (pressure wave) is produced along with the

breakdown. At high power level, the sonic wave becomes loud enough to be audible, and often causes the waveguide to shake. It is created in a short burst as breakdown is initiated. Conceivably we can use acoustic transducers to pick up such sonic wave as an indirect indication of arcing. Signals are then processed to activate the protection mechanism. But in view of the requirement on the device sensitivity, stability, response time, power supply and noise immunity, this method seems at best a supplementary one.

(2) Owing to its surface resistance, the waveguide temperature is elevated during power transmission. At equilibrium, the temperature is stabilized and the gas inside will also come to equilibrium at this temperature. Because of the reduction in gas dielectric strength at higher temperature for a given pressure, the maximum power handling capability of the waveguide system is lowered. If a breakdown is suddenly initiated at a certain point, additional heat is imparted to the gas molecules surrounding that point, with the effect of reducing local dielectric strength even further. With the incident power maintained at the same level, it is clear that a catastrophic chain breakdown can be triggered. This is one of the mechanisms that explains the arc movement toward the source. One way to increase the threshold of arcing is to provide sufficient cooling capability to the waveguide system to remove the dissipated heat and to prevent formation of hot spots, thus preserving the maximum power rating. The other would be to increase the gas pressure, which is limited by the strength of the window material and the tolerable leakage rate only.

(3) The waveguide wall heating discussed here is the additional heating due to the presence of arcs. During arcing, part of the energy is deposited in the waveguide wall in the form of heat through the bombardment of energetic electrons and ions. For a prolonged arcing, the local temperature rise in the waveguide can be such that the wall material becomes melted. The turbulent nature of arcing can eject small masses of the molten material into the waveguide. These ejected masses are not directly thermally anchored and get heated up very rapidly, causing more arcings because of the reduced dielectric strength and local field enhancement around these masses. This situation is known as massive breakdown and fortunately is more likely to happen at much higher power levels. In any event, arcs once initiated have to be quenched as soon as possible to avoid any prolonged arcing and its extensive damage.

(4) The remaining part of the energy is distributed among various atomic and molecular processes such as dissociation, ionization, reattachment, recombination or even chemical reaction with wall material. Some of them are radiative, and the others are nonradiative, depending on whether photons are released as a product of the process. The radiation emitted consists of line spectrum and continuum. Because the arc is in a highly complex state with many chemical species, reabsorption of the emission is not negligible, especially for the line spectrum. Therefore, what we are interested in is the total amount of energy of the net emission coming out of the arcing region and how it is spectrally distributed. Such information for waveguide arcs is rather incomplete and is very difficult to obtain due to its time-dependent and random nature. There exist some calculations of equilibrium nitrogen plasma radiation which agree more or less with experimental results (e.g., Ref. 6). As indicated before, the radiation characteristics depend strongly on the thermal-chemical state of the arc plasma. For example, for a difference in plasma temperature by a factor of 2 (say 7,000 and 14,000 K), calculations showed that the net emission per unit source volume per unit solid angle can differ by more than 3 orders of magnitude. Moreover, these calculations covered only a very limited range of radiation spectrum while experimental observations seemed to indicate a much broader spectral distribution, probably ranging from UV to low frequency RF. Thus it shows the need that more data pertinent to the real arcs have to be gathered experimentally.

In order to overcome this inherent difficulty of measuring time-dependent arc properties, we plan to carry out measurements on a sustained arc inside a resonant section of a waveguide system. This scheme will not only provide us a more or less stable source but needs only $1/Q$ of the power to maintain the same level inside the resonant section, where Q is the loaded quality factor of the resonant section. This should solve the dilemma of trying to initiate an arc on one hand and on the other, to protect the klystron amplifier at the same time. Both the total radiation intensity and the spectral distribution from the sustained arc will be measured. The spectral range covered will be determined by the measuring instrument. With known arc geometry, detector sensitivity and the relative orientation of the arc and the detector, a normalized arc emission characteristic can be obtained. Such a controlled experimental arc probably is a good approximation to an arc hanging at the klystron output window and is expected to less resemble a moving arc. The variable parameters in this study would be incident power level, gas pressure, gas temperature, arc geometry and pulse length. With slight modification, the arc formation time, the arc energy absorption and arc traveling speed can also be measured. Detail experimental considerations, arrangements and results will be presented in the future.

III. Arc Detection

With the characteristics of waveguide arcs approximately known, we could then proceed to design a detection system with certain predictable performance. Because the detected arc radiation is eventually converted back to electrical energy for control purposes, a fairly general detection scheme can be outlined as shown in Fig. 3. In addition to the direct arc emissions and those indirectly scattered into the optical entrance aperture, there are also ambient light leakage and output window glow. The ambient light can, in principle, be reduced to an insignificant level by properly arranging and shielding the microwave components. The window glow on the other hand presents potentially a more serious noise source. The glow is a consequence of the dissipation in the output window under normal high power transmission; i.e., it is an integral part of the power transmission process. Its exact nature has not been carefully examined so far, and its effect on the arc detector can only be speculated at this time. Our study will look into this problem to determine its seriousness and will recommend remedies, if needed, such as better cooling of the window or designing a frequency-sensitive detector which will ignore the glow.

Upon entering the aperture, not all the light is transmitted due to the Fresnel reflection if there is a difference in the indices of refraction across the interface (typically 5 percent). Furthermore, if optical fiber is used for transmitting the light signal over some distance, only those beams with incident angle less than a certain acceptance angle will be launched into propagating modes of the optical fiber.

If we define $J_1(\nu,\vec{\gamma})$ as the spectral density at frequency ν of arc emission per unit volume per unit solid angle at arc spatial coordinates $\vec{\gamma}$, then

$$I_1(\nu) \equiv \int_{\substack{volume \\ \Omega(\theta<\theta_a)}} J_1(\nu,\vec{\gamma})\, dV d\Omega \qquad (1)$$

is the spectral density of the direct arc emission entering the entrance aperture that will propagate inside the optical fiber guide, where the solid angle Ω is subtended by the entrance aperture toward the arc. Similarly, we can define $J_2(\nu)$, $J_3(\nu)$ and $J_4(\nu)$ for the indirectly scattered arc emission, the ambient light leakage and the window glow respectively.

Furthermore, we will define the following quantities:

$F(n_1,n_2)$ = fraction of Fresnel reflection loss, where n_1 and n_2 are the indices of refraction for the two adjacent media across which the light is transmitted.

$T(\nu)$ = transmittance of the optical fiber guide

$P(\nu)$ = transfer function of the optical signal processing

$R(\nu)$ = responsitivity of the optical transducer, (A/W)

Then the optical detector partial electric current output due to the arc light input at the entrance aperture is

$$I = \int [J_1(\nu) + J_2(\nu) + J_3(\nu) + J_4(\nu)]\, [1-F(n_1,n_2)]\, T(\nu) P(\nu) R(\nu)\, d\nu \qquad (2)$$

$$\equiv I_1 + I_2 + I_3 + I_4$$

where signal current comes from direct and indirect arc emissions $(I_1 + I_2)$.

The total current of the optical transducer is

$$I_{total} = I + I_N$$

$$\equiv (I_1 + I_2) + (I_3 + I_4 + I_N) \qquad (3)$$

where I_N is the noise current of the optical transducer. A substantial fraction of the noise current comes from the temperature-sensitive dark current of the detector.

The signal to noise ratio (SNR) at this point is

$$\left(\frac{S}{N}\right)^2 = \frac{(I_1 + I_2)^2}{I_3^2 + I_4^2 + I_N^2} \approx \frac{(I_1 + I_2)^2}{I_4^2 + I_N^2} \qquad (4)$$

if ambient light leakage is negligible.

The magnitude of this required input SNR is an important design parameter to be determined. The final SNR at the output of the threshold logic circuit depends, of course, on the electrical components used and should be maximized despite the presence of power supply ripple, EMI, and thermal drift. Its magnitude will be determined based on the required signal level, detection probability and acceptable false alarm rate.

In reality, there are additional losses in the optical path when connections have to be made. A general rule of thumb here is that about 2-3 dB/connector and 0.1 dB/splice loss are

present. For each step of optical path, ambient light leakage is also always present. We have assumed they can be minimized to be negligible. Typical fiber transmittance over the visible and IR spectrum is about 3 dB for a length of 0.5 m. Additional fiber input coupling losses may be necessary in order to isolate the optical transducer from being exposed to intense RF. The dielectric fiber may be advantageous in overcoming ground loop problems in the detection circuit, however.

The eventual total current output is limited by the spectral range over which the transducer has appreciable responsitivity. The commonly used optical transducers are pin photodiode, avalanche diode and photomultiplier tube. The first two are solid-state devices which require a bias of about 20 and 200 volts respectively. The photomultiplier tube is rather bulky and requires more than 1 kV supply. Our experimental study will primarily concern solid-state devices because, in parallel to this study, we will also evaluate a commercial arc detector based on photomultiplier tube. Solid-state devices seem to have adequate sensitivity and response time for arc detection. But their dark currents tend to increase rather rapidly with increasing temperature, thus changing the operation point of the arc detector. Often this thermal drift is large enough to cause false activation of arc protection and to saturate the arc detector. These have been the major problems encountered in the present arc detectors. The increase in the dark current as a function of temperature is inherent to the semiconductor p-n junction inside the diode and, therefore, the solution is either to maintain the diode temperature, or to compensate the thermal drift or to use ac coupling and/or high-pass filtering for the signal and noise.

The output voltage originated from the optical transducer is then compared to a reference voltage to produce a logic output. The threshold is determined by the amount of light output expected from an arc as well as the safety margin for noise and thermal drift. One way to increase the detector sensitivity is to increase the load impedance of the optical transducer as much as possible. However, the most important consideration here is to make sure that the time delay between the arcing and the logic pulse output is less than a few microseconds for a safe arc protection. This may have to be done at slight expense of the detector sensitivity and SNR.

IV. Conclusions

We have briefly discussed the waveguide arc according to a simple model based on an engineering viewpoint and outlined a general scheme for achieving protection against arc damage. Several questions have been raised concerning the waveguide arc characteristics and the arc protection that we plan to answer both experimentally and theoretically as soon as possible so that a reliable arc protection system becomes available not only to presently attended transmitter subsystems but also to unattended ones in the future as well.

References

1. May, R. E., "Characteristics and Effects of CW High Power Breakdown in Waveguide," *IEEE MTT-S Int. Microwave Symp. Digest*, p. 151, 1976.

2. Nakamura, Makoto, Saito, Takaya, and Kuramoto, Minoru, "Characteristics of High Power Breakdown at 28 GHz," *IEEE Trans. MTT-26*, p. 354, 1978.

3. End n, R. P. J., "Microwave Breakdown in Double Ridged Waveguide," *J. Naval Sci.*, Vol. 2, p. 4, 1976.

4. Gilden, M., and Gould, L., "Handbook on High Power Capabilities of Waveguide Systems," Microwave Associated Inc., Burlington, MA., 1964.

5. Ciavolella, J., "Take the Hassle Out of High Power Design," *Microwave J.*, p. 60, June 1972.

6. Barfield, W. D., "Theoretical Study of Equilibrium Nitrogen Plasma Radiation," *J. Quant. Spectrosc. Radiat. Transfer*, Vol. 7, p. 471, 1977.

7. Her nan, W., and Schade, E., "Radiative Energy Balance in Cylindrical Nitrogen Arcs," *J. Quant. Spectrosc. Radiat. Transfer*, Vol. 12, p. 1257, 1972.

8. Acampora, A. S., and Sproul, P. T., "Waveguide Breakdown Effects at High Average Power and Long Pulse Length," *Bell System Tech. J.*, Vol. 51, p. 2065, 1972.

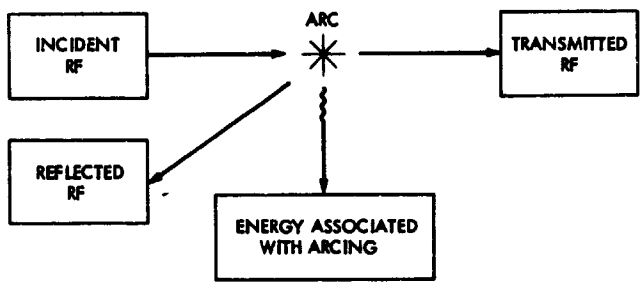

Fig. 1. Waveguide arc energy relationship diagram

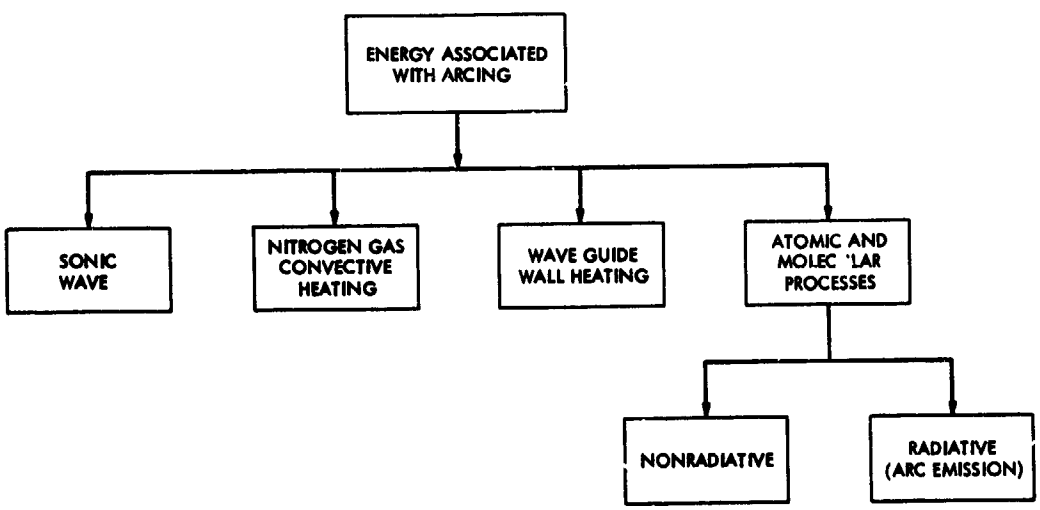

Fig. 2. Waveguide arc macroscopic energy division

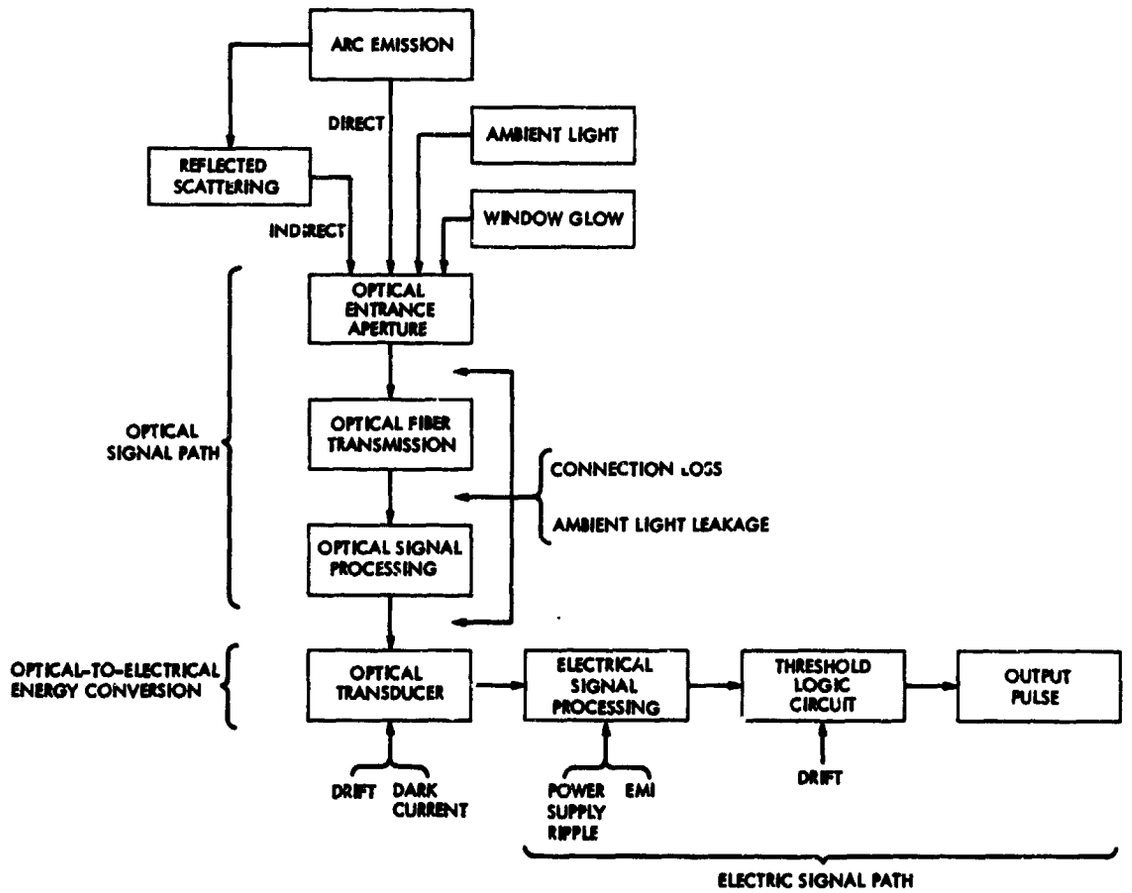

Fig. 3. A general scheme for waveguide arc detection

New X-Band Microwave Equipment at the DSN 64-Meter Stations

R. Hartop
Radio Frequency and Microwave Subsystems Section

In order to improve the performance and capabilities of the DSN 64-m antennas at X-band, extensive modifications to the XRO cone assemblies are in process. The changes include a new feed assembly with a dual hybrid mode horn and orthogonal mode junction, dual traveling wave masers, and a new receiver mode selector.

I. Introduction

The X-band cone assembly (Ref. 1) on the 64-meter antennas originally provided the capability for RCP reception only, with one traveling-wave maser (TWM). The feed was later changed to a Mod II version (Ref. 2) that provided remotely selectable RCP or LCP.

In order to provide increased performance and additional capabilities, especially for the Voyager mission, the XRO cone has undergone a complete redesign. It is planned to reconfigure the three DSN cones in the field; this is the first time such an extensive change to a feed cone has been attempted in place.

After removal of some 90 percent of existing equipment within the cone, the following major changes will be implemented:

(1) A new feed assembly, the Mod III XRO feed.

(2) Dual X-band traveling wave masers.

(3) New monitor receiver.

(4) New TWM support racks.

(5) New output waveguide runs.

(6) New output switching configuration for the monitor receiver.

(7) New receiver mode selector.

To further complicate the changes, the two overseas stations will be implemented with the new Mod III feed assembly on a different schedule from DSS 14. Thus it was necessary to design two new XRO cone configurations: (1) the Mod II version for overseas serves as an interim configuration until items (1) and (7) above are implemented; and (2) the Mod III version for DSS 14 and, later, DSS 43 and DSS 63. Because of the differences in physical size and output configuration of the Mod II and Mod III feeds, this required extensive differences in such details as the maser support stands, maser output waveguides, switch control subsystem, and many support brackets and hardware.

II. The Mod III XRO Feed Assembly

The new feed assembly (Fig. 1) provides the following major changes:

(1) A dual hybrid mode feed horn (Ref. 3) for more efficient subreflector illumination.

(2) An orthogonal mode junction to permit the simultaneous reception of RCP and LCP.

As discussed in Ref. 3, it is expected that the new feed horn will increase the antenna gain approximately 0.29 dB.

III. Dual Traveling Wave Masers

The primary purpose of implementing dual masers is to improve reliability during critical encounter periods by having a second maser cooled down and ready to be switched on line in seconds should the primary maser fail. The presence of two operating masers, however, also leads to increased radio science capability. Thus, with the orthogonal mode junction, it will be possible to receive two orthogonal polarizations simultaneously. Since the polarization selectability of the Mod II feed is retained in this new feed, it is possible to remotely select which polarization (RCP or LCP) is received by TWM 1, with TWM 2 receiving the opposite polarization at all times.

IV. Receiver Mode Selector

Because of this dual-channel feature, it was necessary to design a new receiver mode selector that provided two inputs (rather than a single input as before) and four receiver outputs, so configured that any receiver can independently connect to either maser output. Up to four additional receivers (for a total of eight) can also be connected to the mode selector panel, but with some restrictions on independent maser output selection.

V. Configuration Control Subsystem

Concurrently with the changes to the XRO cone assembly, a new configuration control subsystem is being implemented. This necessitated additional changes in the cone switch control junction box, cable package, and control panel.

VI. Maser Support Equipment and Output Waveguides

With the removal from the cone of the older configuration maser package and monitor receiver, it was necessary to relocate the output waveguide runs and design new brackets for the new maser packages and their support racks. This is the second installation of this equipment after the SXD cone assemblies for the 34-m antennas (Ref. 4), and some of the techniques generated in that project were adapted to the XRO cone redesign. A complicating factor in laying out the waveguide runs involves the requirements for four waveguide couplers. One coupler for each maser output supplies the monitor receiver with its signal through a waveguide switch to select TWM 1 or 2. An additional coupler for each maser output provides an injection point for calibration signals.

VII. Field Implementation

At the time of this reporting, DSS 14 has been implemented with the Mod III configurations, with only a few minor details remaining to complete the task. Test data are not yet available.

During October and November the overseas stations will be implemented with the Mod II XRO cone configurations (dual masers only). It is planned to upgrade these stations to the Mod III configuration during late 1979, in time for Saturn encounter.

References

1. Hartop, R., "X-Band Antenna Feed Cone Assembly," TR 32-1526, Vol. XIX, pp. 173-175, Jet Propulsion Laboratory, Pasadena, Calif., Feb. 15, 1974.

2. Hartop, R., "Selectable Polarization at X-Band," PR 42-39, pp. 177-180, Jet Propulsion Laboratory, Pasadena, Calif., June 15, 1977.

3. Thomas, R., and Bathker, D., "A Dual Hybrid Mode Feedhorn for DSN Antenna Performance Enhancement," PR 42-22, pp. 101-108, Jet Propulsion Laboratory, Pasadena, Calif., Aug. 15, 1974.

4. Hartop, R., "Dual Frequency Feed Cone Assemblies for 34-Meter Antennas," PR 42-47, pp. 85-88, Jet Propulsion Laboratory, Pasadena, Calif., Oct. 15, 1978.

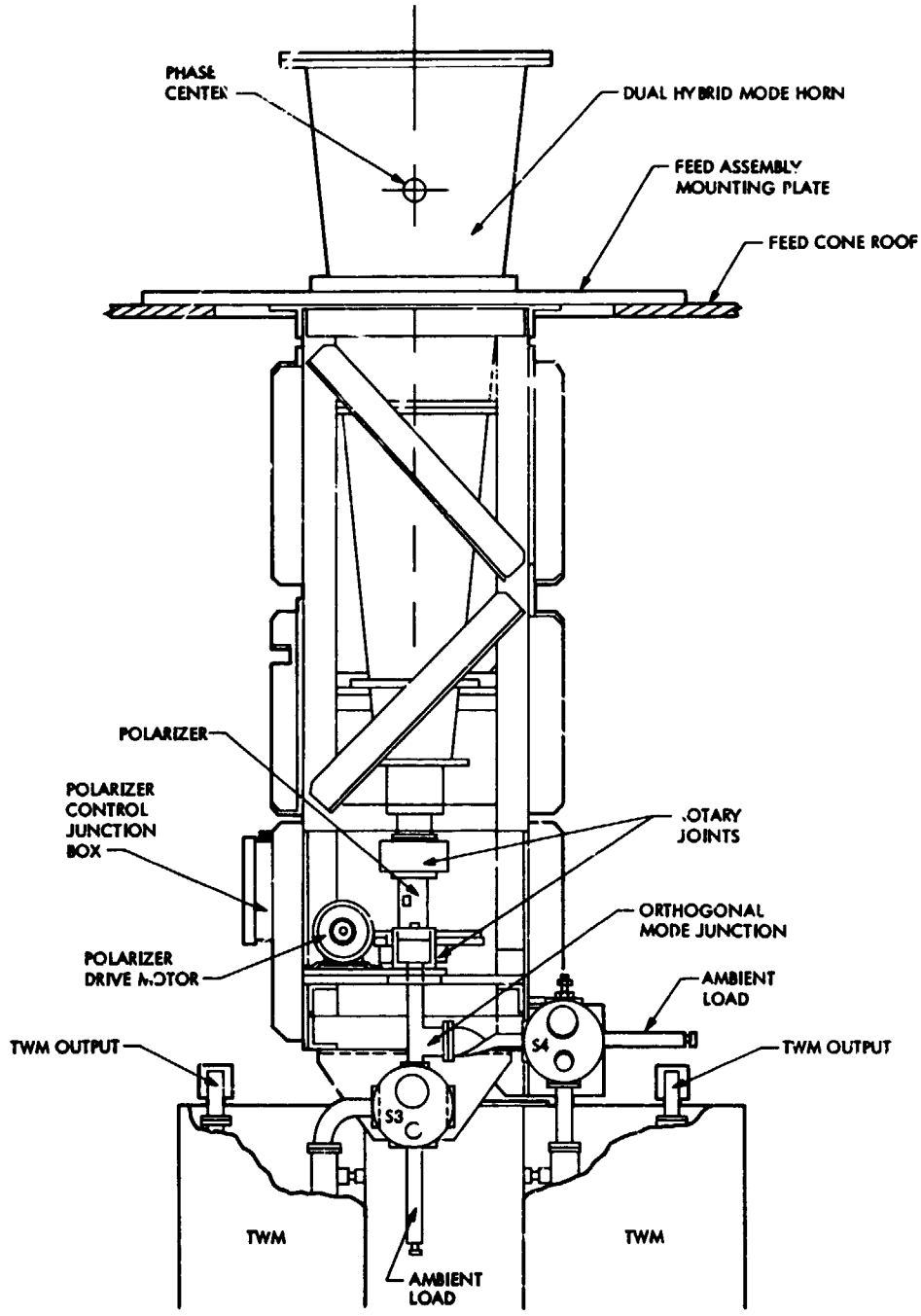

Fig. 1. The Mod III XRO feed assembly

DSN Water Vapor Radiometer Development—Recent Work, 1978

P. D. Batelaan and S. D. Slobin
Radio Frequency and Microwave Subsystems Section

A water vapor radiometer (WVR) has been developed that measures the atmospheric noise temperature at two different frequencies near 22 GHz. These noise temperatures are used in empirical-theoretical equations that yield tropospheric range delay, in centimeters, through the atmosphere along the beam of the WVR. This range correction is then applied, as needed, to measurements concerning spacecraft range and to VLBI baseline determinations. This report discusses the WVR design and calibration techniques.

I. Introduction

Development work has continued on the water vapor radiometer (WVR). This article will discuss progress since the last reports (Refs. 1 and 2). Also mentioned are new frequencies that resulted from analytical support activities and a discussion of the calibration load techniques that have evolved since this work started. The cold calibration load mentioned in Refs. 1 and 2 has been replaced by a hot load. The block diagram of the instrument is unchanged since Ref. 1 except for this change in load design. Figure 1 shows the WVR in its current configuration.

A formal set of technical specifications and recommendations for WVRs has been generated (Ref. 3), with inputs from the outside scientific community.

II. Calibration Loads and Techniques

In the water vapor radiometer, the radiometric noise temperatures of the sky at two frequencies near the water vapor resonance line, 22.235 GHz, are used to infer the phase delay through the atmosphere. To get an accurate measurement of these noise temperatures, the radiometer can be accurately calibrated by using waveguide calibration loads whose absolute radiometric temperature has been determined from insertion loss and physical temperature measurements (Ref. 4).

The method of using absolutely calibrated waveguide loads to calibrate a radiometer depends on several assumptions:

(1) The Rayleigh-Jeans approximation to the Planck blackbody-radiation law must hold at the frequency of interest.

(2) Thermal gradients between the physical temperature sensor and the passive microwave load radiating region are negligible.

(3) Energy radiated by the load is not significantly reflected in reaching the radiometer receiver.

(4) Insertion losses and their physical temperatures between the load and the radiometer receiver are known.

(5) The temperature sensor that measures the physical load temperature must be of sufficient accuracy (Ref. 5).

It is the aggregate effect of all these uncertainties (Ref. 6 identifies ten of them) that leads to the total cal-load temperature error. It should be noted that an ambient temperature cal-load can be designed to have no significant temperature gradients. In this case, the radiometric temperature of the ambient load is equal to its physical temperature (the load looks like a perfect blackbody):

$$T_{AR} = T_{AP} \tag{1}$$

where for future reference,

T is temperature in kelvins

A is ambient

R is radiometric

P is physical

The best radiometer measurements are achieved when the instrument calibration curve extends on either side of the desired measurement region, i.e., data can be interpolated rather than extrapolated. In the case of the WVR, measured sky temperatures are as low as 10 K; it is impractical to try to achieve the true interpolation condition for the calibration curve. However, having one calibration reference load near the coldest expected values would still be desirable to minimize the strong "leverage" effects that often result when using an extrapolated calibration curve.

To achieve these desired colder temperatures, several refrigeration devices were tried. The first was a two-stage Peltier junction, which was quite reliable but achieved only -40°C (233 K), and then only with a two-gallon-per-minute total-loss, water-cooled heat sink. The second device was a reciprocating [illegible]-expansion refrigerator that achieved -90°C (183 K), but required, along with its air source, high maintenance.

The third cooling device was a multistage, closed-cycle fluorocarbon refrigerator that achieved -120°C (153 K) and showed great promise. The fundamental problem with this machine was that it was intended for a laboratory environment, and after several field tests it failed. The manufacturer did major redesign and modification for field use, but before it could be tried again, the decision was made to abandon the cooled cal-load and proceed with the development of a heated reference load. This decision was based on a critical examination of the complexity and potential unreliability of available cryogenic refrigerators when used under field conditions.

If the hot cal-load were to be absolutely calibrated, all of the previously mentioned uncertainties in its noise output would be multiplied by the leverage effect of having both cal-loads far removed from the sky temperature. For example, if the two cal-loads and sky are 400 K, 300 K, and 20 K, respectively, cal-load uncertainties are multiplied by a leverage of 2 to 3 for antenna temperature determinations in the region of 0 to 100 K. Figure 2 illustrates this condition. However, this leverage degradation could be overcome if the cal-load could be calibrated using the cosmic background temperature of 2.7 K as a calibration source via a technique known as "tipping curves." This technique does not require accurate knowledge of insertion losses between the load and receiver.

A tipping curve is done by pointing the radiometer antenna at elevation angles nominally corresponding to one, two, three, and four air masses (elevation angles of 90, 30, 19.47, and 14.47 deg respectively) and noting the radiometer output in "counts." This information is used to extrapolate to the value of counts at zero air masses. Since this condition of zero air masses corresponds to viewing only the cosmic background radiation of 2.7 K, the number of counts at 2.7 K can be derived. The relationship between counts at zero, one, and two air masses is, as an example (to a good approximation), $N_0 = 2N_1 - N_2 = N_c$, the counts corresponding to the cosmic background radiometric noise temperature of 2.7 K (T_c). The radiometer is then switched to the ambient cal-load and the counts N_A are noted. From these measurements, the radiometer gain in counts/kelvin is found to be

$$K_1 = \frac{N_A - N_C}{T_{AP} - T_C} \tag{2}$$

Sky noise temperature can then be determined from

$$T_S = T_{AP} - \frac{1}{K_1}(N_A - N_S) \tag{3}$$

where N_S is the counts when the radiometer views the sky.

It should be noted that these equations ignore several small correction terms to avoid complicating the discussion. In actual practice, various corrections related to noise temperature saturation and instrument parameters are applied. The sky temperature can be determined as shown above since the system has been designed to be linear. A good feature of this tipping curve calibration is that the cosmic background radiation, used as an equivalent cold calibration load, is actually lower than the sky temperatures the instrument normally measures. When used in conjunction with the ambient load,

as is done here, the resulting calibration curve allows sky measurements to be interpolated rather than extrapolated. This means that sky measurement errors, due to cal-load uncertainties, are less than these cal-load uncertainties themselves.

There are some drawbacks to this method. First, the atmosphere is not always well-behaved enough to allow tipping curve calibrations of instrument gain. The possibility of some "lumpiness" in water content will prevent a correct extrapolation of the tipping curve data to zero air masses. To assist in dealing with this problem, a four elevation point tipping curve is used to verify proper atmosphere stratification (atmospheric parameters constant with respect to horizontal movement). The second drawback of this method is that accomplishing a good tipping curve calibration is relatively time-consuming.

Since the radiometer may not hold its gain calibration for the long periods of time between tipping curve tests, a second calibration method is carried out by using the ambient load in conjunction with some nonambient load. In the case of the present WVR, high reliability could not be achieved with coolers for a cold cal-load, and it was decided to use a hot cal-load as the nonambient load.

It is possible to solve for the radiometric noise temperature of the hot load by using the tipping curve derived gain for the radiometer and switching to the hot cal-load as an additional real-time step in the tipping curve sequence. Then the hot load radiometric noise temperature can be calibrated with relationship

$$T_{HR} = \frac{1}{K_1}(N_H - N_A) + T_{AP} \tag{4}$$

In actual practice, the radiometric hot load temperature will be somewhat less than (but strictly related to) its physical temperature. Since the stability of the hot cal-load, a passive device, is many times better than that of the radiometer, an active device with over 100 dB system gain, the calibrated hot load can be used in radiometer measurements between infrequent tipping curve calibrations.

This is done by defining a new gain based on the now-calibrated hot load,

$$K_2 \equiv \frac{N_{H2} - N_{A2}}{T_{HR} - T_{AP2}} \tag{5}$$

where the subscript 2 refers to the latest real-time determination of counts and radiometric temperatures.

Ideally, in a drift-free instrument, $K_1 \equiv K_2$. In operation, the instrument measures counts on sky, hot load, and ambient load, and physical temperatures on hot load and ambient load. Equation (5) is evaluated each time a sky temperature measurement is made. The resulting new K_2 (determined every 5 minutes, or so) is used in real time to determine radiometric sky temperatures:

$$T_S = T_{AP2} - \frac{1}{K_2}(N_{A2} - N_S) \tag{6}$$

The value of K_2 can be continuously compared to K_1 (the tipping curve derived gain) and its previous values as a monitor of radiometer performance.

III. Frequency Selection

The WVR frequency pair of 18.55 and 22.235 GHz were originally chosen only on the basis of sensitivity to separation of the noise temperature effects of water vapor from water droplets (clouds). Frequencies near the resonance line (designated probing frequencies) are more sensitive to vapor than frequencies well off resonance (designated reference frequencies).

Possible pairs were 26.5/22.2, 18.0/22.2, and 31.4/22.2 GHz, for reference and probing frequencies respectively, in the order of increasing accuracy to perform the measurement. Since the 18.0/22.2-GHz frequency pair would achieve almost the same accuracy as the 31.4/22.2-GHz pair, and could be accomplished in a single waveguide-band system, it was chosen for this radiometer.

More recent advanced models have shown that the relationship between noise temperature and phase delay, both induced by atmospheric water vapor, is excessively altitude-profile dependent with the 18.0/22.2-GHz frequency pair. This causes an additional tropospheric delay error source due to modeling error. However, several other frequency pairs exhibit much lower vapor profile dependency (Ref. 7). The two best frequency pairs are 20.0/26.5 GHz and 20.3/31.4 GHz. Analysis predicts that both of these pairs will have an error in measuring water vapor induced phase delay of less than 2 cm rms down to 15 deg elevation (~4 air masses) under nonprecipitating weather conditions. The relative accuracy of the two

pairs favors the 20.3/31.4 pair slightly, about 15 percent (1.5 mm) at zenith, decreasing to equality at 15 deg elevation.

Since the performance figures mentioned are based on an analytical model, it would seem prudent to experimentally verify them. A NEMS (Nimbus E Microwave Spectrometer) has been refurbished and retuned to 21.0/31.4 GHz. (This radiometer would not operate at a frequency less than 21.0 GHz without serious performance degradation.) NEMS will be used to verify the 20.3/31.4-GHz pair. This modification is now complete and tests are awaiting completion of software development for the radiometer microcontroller.

To verify the one-band frequency pair, 20.0/26.5 GHz, it was proposed to modify the DSN Developmental WVR presently at 18.55/22.235 GHz. This modification consists of changing the local oscillators, mixer, isolators, and horn antenna The work has been completed except for the antenna. Since there exists a large amount of operational history with this WVR at the 18.55/22.235-GHz frequency pair, the option of restoring this frequency capability has been included in the modification package. The installation of the modification kit that changes between the 18.55/22.235-GHz pair and the 20.0/26.5-GHz pair requires about one day. In fact, this option has been exercised once already in support of a VLBI experiment scheduled at DSS 13 during August 1978.

One observation regarding the relative desirability of the 20.3/31.4- and 20.0/26.5-GHz pair is offered here. A 20.3/31.4-GHz WVR requires two complete and independent microwave receivers, their associated antennas and calibration loads, while a 20.0/26.5-GHz WVR requires only a single microwave receiver and associated parts. A life-cycle cost analysis (Ref. 8) shows a 25 to 30 percent advantage in favor of the 20.0/26.5-GHz pair when examining the microwave portion of the WVR system only, simply due to fewer components, and only a small decrease in performance (~1.5 mm rms additional delay error). These accuracy figures are modeled and have not yet been experimentally verified.

IV. WVR Calibration and Field Tests

During August and December 1977, a series of WVR antenna temperature measurements were made at Edwards Air Force Base, about 50 miles north of Los Angeles in the Mojave Desert. Radiosondes are launched daily there; and simultaneous WVR microwave measurements were made. Radiosondes measure temperature, pressure, and relative humidity in flight and these can be used to determine the tropospheric range delay effect of the atmosphere along the path of the radiosonde.

Comparison of microwave and atmospheric measurements results in a WVR calibration linking antenna noise temperature and tropospheric delay. Tipping curves were also carried out to determine the radiometric temperature of the hot calibration load.

Data from the Edwards tests are still being examined. Preliminary studies indicate that the experimental measurements encompass primarily clear atmospheres, with water vapor only and no liquid water (clouds) present. This cannot be considered a sufficient data base from which to calibrate the WVR completely; however, certain theoretical considerations may be invoked to generalize the WVR calibration. A complete calibration analysis and description of VLBI support tests will appear in a later volume.

V. Future Work

The DSN Developmental WVR will be used in conjunction with Project ARIES (Astronomical Radio Interferometric Earth Surveying) (Ref. 9). Additional work should be done to experimentally verify the analytical model used in selecting optimum frequencies. This could be done by completing the frequency modifications to both the NEMS radiometer and DSN Developmental WVR, followed by their use in VLBI measurements and direct comparison with a LASER/microwave ranging instrument (Ref. 10). Additional radiosonde/WVR comparisons should be made to calibrate the WVR over a wide range of atmospheric conditions.

References

1. Batelaan, P. D., and Slobin, S. D., "Development of a Water Vapor Radiometer to Correct for Tropospheric Range Delay in DSN Applications," *DSN Progress Report 42-33*, Jet Propulsion Laboratory, Pasadena, California, March 1976, pp. 77-84.

2. Slobin, S. D., and Batelaan, P. D., "DSN Water Vapor Radiometer Development – A Summary of Recent Work, 1976-1977," *DSN Progress Report 42-40*, Jet Propulsion Laboratory, Pasadena, California, May 1977, pp. 71-75.

3. Resch, G. M., et. al., "A Recommendation for the Implementation and Further Development of Water Vapor Radiometers in Support of VLBI Activity," Internal Document No. 900-894, Jet Propulsion Laboratory, Pasadena, California, 1978.

4. Stelzried, C. T., "Microwave Thermal Noise Standards," *IEEE Transactions of Microwave Theory and Techniques*, Vol. MTT-16, No. 9, pp. 646-655, September 1968.

5. Collier, R. D., "Accuracy & Precision," *Industrial Research/Development*, April 1978.

6. Daywitt, W. C., et al., *WR15 Thermal Noise Standard*, NBS Technical Note #615, National Bureau of Standards.

7. Wu, S. C., "Frequency Selection & Calibration of a Water Vapor Radiometer," *DSN Progress Report 42-43*, Jet Propulsion Laboratory, Pasadena, California, January 1978, pp. 67-78.

8. Eisenberger, I., and Lorden, G., "Life-Cycle Costing: Practical Considerations," *DSN Progress Report 42-40*, Jet Propulsion Laboratory, Pasadena, California, May 1977, pp. 102-109.

9. Ong. K. M., et. al., "A Demonstration of a Transportable Radio Interferometric Surveying System with 3 cm Accuracy on a 307-m Base Line," *Journal of Geophysical Research*, Vol. 81, No. 20, pp. 3587-3593, July 10, 1976.

10. Thompson, M. C., Jr., et al., *Use of Radio-Optical Dispersion to Study Radio Range Errors on Moving Paths*, Technical Memorandum ERL TM-ITS 190, ESSA Research Laboratories, Institute for Telecommunication Sciences, Boulder, Colorado, July 1969.

Acknowledgement

We are grateful to Sien Wu, Scott Claflin, and Phil Callahan for their excellent analytical support of this work unit. George Resch, especially, has provided guidance in the development, calibration, and field operation of the WVR.

Appendix

The hot cal-load used in the DSN water vapor radiometer is a JPL-fabricated waveguide unit. The waveguide housing is a 5.08-cm-diameter X 14-cm-long copper bar, into which a WR42 waveguide size hole is machined. The load element is a 10.2-cm-long, compound single-taper piece comprised of 60 percent beryllium oxide homogeneously mixed with 40 percent silicon carbide. This material mixture combines good thermal conductivity (2.2 W/cm °C compared with 3.9 W/cm °C for the copper housing) and excellent microwave qualities (36 dB/cm loss). Reflection coefficient of the completed load over the frequencies of interest is better than 0.008. The heater is wound on the copper housing insulated by a 0.08-mm mica sheet. This is then surrounded by a 4-cm layer of molded ceramic fiber insulation and assembled into a cylindrical aluminum housing to provide mechanical support and mounting capability. Heat leakage from the assembly is 40 W at 0°C ambient and 150°C load temperature, well within the heating capability of 100 W. A photograph of the microwave components of this load is shown in Fig. 3. This load was installed in June 1977, and has been used for all tests since then.

Fig. 1. Water Vapor Radiometer

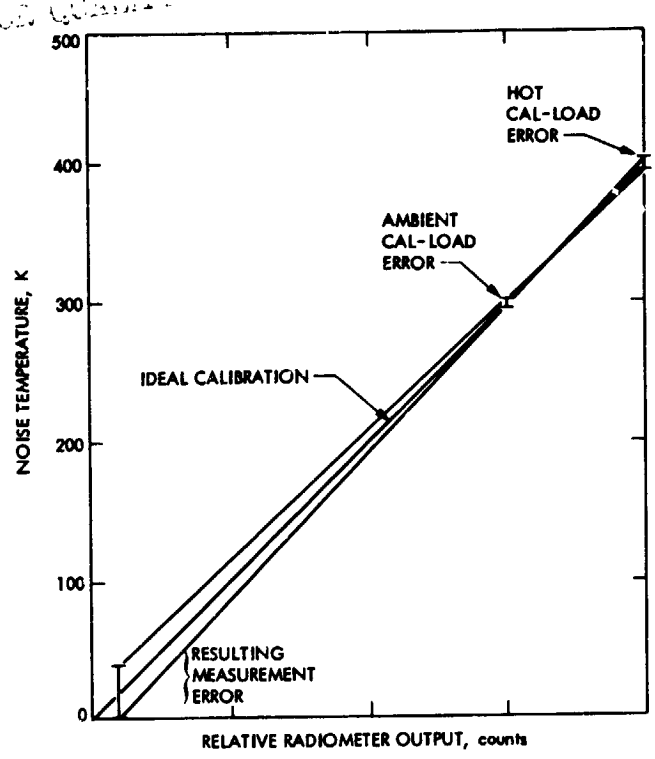

Fig. 2. Effect of calibration load error on antenna temperature determination

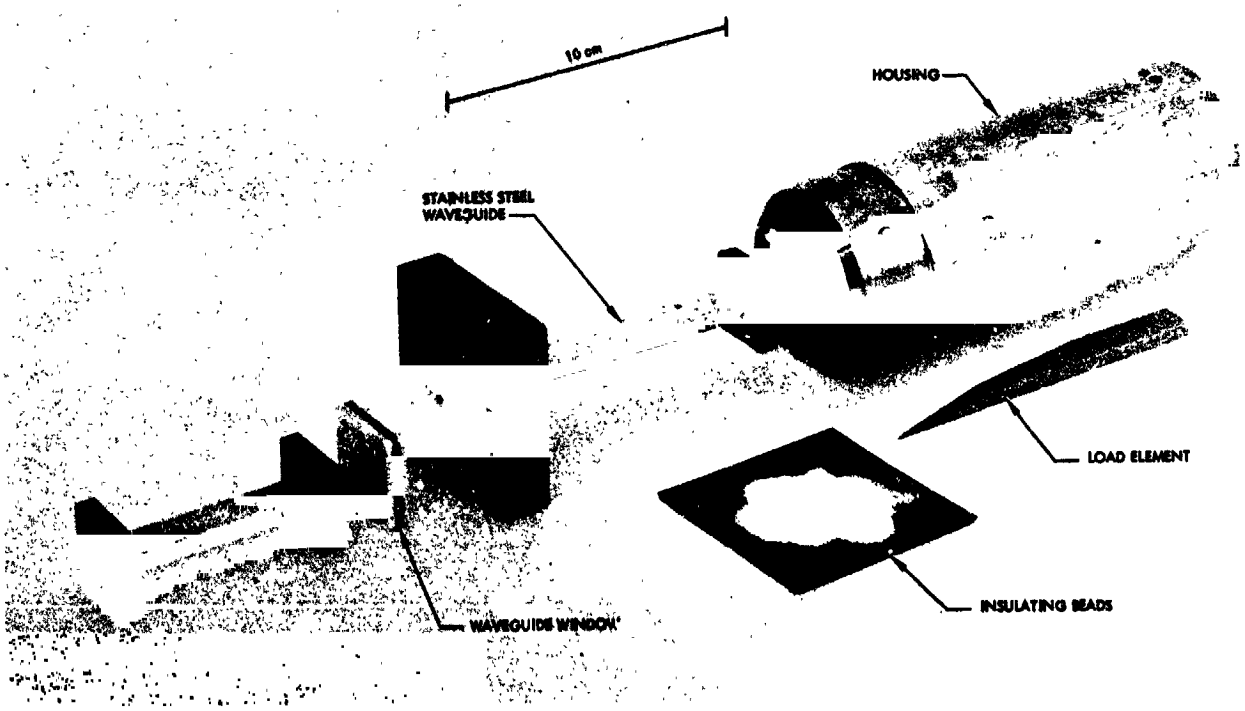

Fig. 3. Exploded view of microwave components of hot calibration load